Ultrafast Terahertz Spectroscopy and Nonlinear Optical Properties of Semiconductor Nanosstructures

Zhen-Yu Zhao

THESE DE DOCTORAT DE

L'UNIVERSITE PIERRE ET MARIE CURIE

Spécialité : Physique

(ED107 : Physique de la Région Parisienne)

Présentée par

Zhenyu ZHAO

Pour obtenir le grade de

DOCTEUR DE L'UNIVERSITE PIERRE ET MARIE CURIE

Sujet de la thèse :

Spectroscopie Térahertz Ultrarapide et Propriétés Optiques Non-Linéaires de Nanostructures Semiconductrices

Soutenu le 17 Juillet 2008

Jury composé de :

Prof. Jérôme TIGNON	Directeur de thèse (France)
Prof. Tianqing JIA	examinateur
Prof. Maria CHAMARRO	
Prof. Fabrice VALLEE	Rapporteur
Prof. Xiaohua YANG	Rapporteur

Abstract

This manuscript presents 2 individual experimental studies in the field of ultrafast carrier dynamics of semiconductor nanostructures:
1. The development of Terahertz time domain spectroscopy (THz-TDS) and its application in gain measurements of GaAs/AlGaAs quantum cascade lasers.
2. The 3rd order nonlinear optical properties of tellurite niobic glasses doped with AgCl nanocrystalss with Z-scan and degenerate four waves mixing (DFWM).
In order to accomplish this goal, we developed a THz-TDS system with different radiation sources: optical rectification in a ZnTe crystal and interdigitated semi-insulating gallium arsenide photoconductive antennas.
First, we studied the competition between Tera-Hertz (THz) generation by optical rectification in <110> ZnTe crystals, two-photon absorption, second harmonic generation and free-carrier absorption. The two-photon absorption coefficient, second harmonic generation efficiency and free-carrier absorption coefficient in the THz range are measured independently. The incident pump field is shown to be depleted by two-photon absorption and the THz radiation is shown to be reduced, upon focusing, by free-carrier absorption. The reduction of the generated THz radiation upon tight focusing is explained, provided that one also takes into account diffraction effects from the sub-wavelength THz source.
Second, we investigated the temporal and spectral properties of the THz emission of a novel semi-insulating GaAs interdigitated photoconductive antenna with different excited carrier densities, in a temperature range from 4.2K to 270K. The THz emission properties are shown to be linear at low bias fields but saturated at large fields due to the intervalley scattering from the Γ band to the L band. The THz performances also saturate for high laser excitation due to the space charge screening. The carrier dynamics at different temperatures was experimentally investigated by recording the temporal and spectral shape of the THz wave. The emitted THz spectrum shifts to the lower frequency with increasing temperature. The impact of electron-hole mobility in this problem is discussed.
Third, we compared the aforementioned two THz generation methods and decided to use photoconductive antennas as the excitation source of our THz-TDS to investigate the gain and losses of a THz quantum cascade laser (QCL) operating at 2.9THz. We investigated the THz gain variation with different injection currents and different temperatures. We measured THz amplitude and phase spectra, allowing the direct determination of the gain. At the emission frequency of the QCL, a value of 6.5cm^{-1} is found. Effects such as gain clamping and spectral narrowing are also observed.
Finally, We investigated the non-resonant ultrafast 3rd order nonlinear optical properties of niobic tellurite glass ($80TeO_2$-$20Nb_2O_5$) doped with silver chloride (AgCl) nanocrystals. Our samples were synthesized by melting-quenching and thermal treatment techniques. We control the grain-size of AgCl nanocrystals by varying the thermal treatment time. Their structures and AgCl nanocrystalss were characterized by spectroscopy and electronic microscopy. The longer thermal treatment time can enlarge the grain-size and increase the AgCl nanocrystalss density, and further results in forming more defect centers and stronger lattice deformation at the interface of AgCl nanocrystals, which gives rise to the bandgap redshift and formation of trapped state excitons. The larger two-photon absorption and local state carrier absorption result in a decrease of the optical limiting threshold, and the third order nonresonant nonlinear susceptibility $\chi^{(3)}$ can be enhanced by the transient polarization of trapped state electrons on the surface of AgCl nanocrytstals.

Keywords : *THz Spectroscopy, Optical Rectification, Photoconductive Antenna, Quantum Cascade Laser, Tellurite Glasses, Nanocrystalss, Nonlinear Optics.*

Résumé

Ce mémoire de thèse présente deux études expérimentales dans le domaine de la dynamique ultra-rapide des porteurs dans les nanostructures semiconductrices:
1. Le développement de la spectroscopie Térahertz dans le domaine temporel (THz-TDS) et son utilisation pour mesurer le gain d'un laser à cascade quantique GaAs/AlGaAs.
2. L'étude des effets de 3^{ième} ordre en optique non linéaire dans des verres de Tellure dopés en nanocristaux AgCl, par "Z-scan" et mélange à quatre ondes (DFWM).
A cette fin, nous avons d'abord construit un montage de spectroscopie Térahertz dans le domaine temporel avec deux sources de rayonnement différentes : la rectification optique dans un cristal non-lineaire <110> ZnTe et par ailleurs des antennes interdigités photoconductrices.
Dans un premier temps, nous avons étudié la compétition entre la rectification optique, la génération de second harmonique, l'absorption à deux photons, et l'absorption par les porteurs libres. Le faisceau pompe subit une absorption à deux photons et le rayonnement THz émis est diminué, dans les conditions de focalisation, par l'absorption des porteurs libres. La réduction de l'émission THz dans les conditions de focalisation est expliquée, à condition de tenir compte des effets de la diffraction de la source THz sub-longueur d'onde.
Dans un deuxième temps, nous avons étudié les propriétés de l'émission THz dans le domaine temporel et spectral d'un nouveau type d'antenne photoconductive interdigitée basée sur du GaAs semi-isolant, en fonction de la densité de porteurs et dans une gamme de température allant de 4.2K à 270K. Les propriétés de l'émission THz sont linéaires pour de faibles tensions appliquées mais révèlent des effets de saturation pour des tensions importantes en raison de la diffusion inter-vallées de la bande à la bande *L*. Les performances THz saturent aussi pour de fortes excitations laser à raison de l'écrantage des charges. La dynamique des porteurs à été étudiée expérimentalement pour différentes températures. Le spectre THz de l'émission se déplace vers les basses fréquences lorsque la température augmente. L'influence de la mobilité électronique est discutée.
Dans une troisième partie, après avoir comparé les deux méthodes de génération THz ci-dessus et décidé d'utiliser les antennes photoconductives comme source d'excitation pour notre montage THz-TDS, nous avons étudié le gain et les pertes d'un laser à cascade quantique (LCQ) fonctionnant à 2.9 THz. Nous avons étudié les variations du gain en fonction du courant injecté, à différentes températures. Nous avons mesuré les spectres d'amplitude et de phase THz, permettant une détermination directe du gain. A la fréquence de fonctionnement du LCQ, nous mesurons un gain de 6.5cm^{-1}. Des effets comme le « clampage » du gain et l'affinement spectral du gain sont observés et discutés.
Pour finir, nous avons étudié le coefficient de polarisabilité d'ordre 3 des verres de Tellure ($80TeO_2$-$20Nb_2O_5$) dopés en nanocristaux AgCl. Nous avons produit des échantillons par les techniques fonte-trempe et traitement thermique. Les résultats de la caractérisation révèlent qu'un traitement plus long augmente la tailles des nanocristaux qui donne lieu à l'apparition de plus de défauts et une plus grande déformation du réseau cristallin des nanocristaux aux interfaces avec le verre. Des états électroniques piégés apparaissent sous l'effet de la déformation de la structure cristalline. Une forte absorption à deux photons et une absorption des états électroniques piégés réduit le seuil de la limitation optique. Le coefficient polarisabilité non linéaire $\chi^{(3)}$ augmente à cause de la formation des défauts et des états électronique localisés.

Mots Clés : *Spectroscopie THz, rectification optique, antenne photoconductive, Laser à cascade quantique, Verres Tellure, nanocristaux, optique non-linéaire.*

FIGURE CAPTION

Contents

General Introduction

With the development of compact femtosecond lasers, ultrafast spectroscopy [1-3] has become a powerful tool for investigating the carrier dynamics in semiconductor nanostructure. Recently, the special attention was dedicated to the long-wavelength edge of far-infrared spectrum between 300 gigahertz ($3x10^{11}$ Hz) and 3 terahertz ($3x10^{12}$ Hz), corresponding to the sub-millimeter wavelength range between 1mm and 100 μm. This spectral range is called terahertz (THz) or the THz gap (due to the major lack of emitters or detectors in this spectral range)[4,5]. It is useful to have the following numbers in mind:

1THz↔330μm↔1picosecond↔4.1meV↔10K

THz waves have a unique character. There are non-ionizing and share with microwaves the capability to penetrate a wide variety of non-conducting materials such as clothes, plastic, wood, sand and soil. Some chemical materials such as gas and liquid have unique spectral fingerprints in the THz band. These properties and the recent development of new techniques triggered special interest both for applications (in imaging, gas sensing etc) as well as for new fundamental physics experiments. With respect to the present work, we underline the development of terahertz time-domain spectroscopy (THz-TDS) [6-10] to investigate the semiconductor nanostructures.

The generation and detection of "T-Rays" had been unknown for a long time, which hampered the development of this technique, until the 1970s. *Yang Richard* and *Shen* at Berkeley, *Yajima* and *Takeuchi* in Japan presented respectively the demonstration of far-infrared (FIR) generation due to the optical rectification with use of second order nonlinear crystal and picosecond pulses. Nonlinear optical rectification was proposed as the first mean to generate far-infrared radiation. Meanwhile, *Auston* and *Lee* at AT&T bell laboratory used ultrashort laser pulses to excite Cr-doped semi-insulating GaAs (SI-GaAs) in "photoconductive switches" to generate far-infrared radiation. Until today, the aforementioned two THz generation methods (optical rectification and photoconductive methods) are successfully used in THz-TDS. The basics about THz-TDS, THz generation and THz detection are given in the Chapter 1.

Compared with other nonlinear crystals, <110> ZnTe crystal have the merit of large second-order nonlinear susceptibilities, have well-suited phase-matching properties [11,12] and so are

good optical rectification devices, widely used for THz generation [13-16]. Current challenges in this field concern the competition between optical rectification and other nonlinear processes such as second harmonic generation (SHG), two-photon absorption (TPA) and free-carriers absorption (FCA) [17-21]. Moreover, when the exciting laser spot size becomes smaller than the typical THz wavelength, it induces a decrease of the THz generation due to diffraction [20,22]. Nevertheless, to date, existing analysis of these phenomena are not comprehensive and the explanations are sometimes even contradictory [20,21]. In particular, the effect of free carrier absorption [23] on the THz radiation was neglected in previous studies. While developing a first THz-TDS setup in LPA at ENS, we contributed to this field (Chapter 2) and determined the best conditions for generating THz in our experiment.

On the other side, the technique and the physics of photoconductive antennas are still progressing. Of particular interest for the present work, *Dreyhaupt et.al*. [24,25] and *Hattori et.al.* [26] discovered the practical advantages of generating THz using interdigitated photoconductive antennas (at room temperature). The temperature effects are known since *Markel et.al*.[27] in conventional photoconductive antennas. *Rodriguez et al.* [28] found that space charge screening (SCS) results in a "bipolar" THz temporal waveform and a THz spectral blue-shift but they ignore temperature dependence of SCS. Nathan Jukam, in LPA at ENS, recently fabricated an interdigitated photoconductive antenna for our THz-TDS setup. We characterized it as a function of temperature and excitation power.

In 1994 [29], a new infrared semiconductor emitter appeared: the quantum cascade laser (QCL), first demonstrated by *Faist et al*. at Bell Laboratories. A QCL comprises a periodic series of thin layers of varying material composition forming a superlattice. The superlattice introduces a varying electric potential across the length of the device, inducing a varying probability for the electrons to occupy different positions over the length of the device. This is referred to as one-dimensional multiple quantum well confinement and leads to the splitting of the bands of permitted energies into a number of discrete electronic subbands. By suitable design of the layer thicknesses it is possible to engineer a population inversion between two subbands in the system which is required in order to achieve laser emission. Since the position of the energy levels in the system is primarily determined by the layer thicknesses and not the material, it is possible to tune the emission wavelength of QCLs over a wide range in the same material system. The revolutionary progress occurred in 1998, when *Sirtori et al*. [30] designed the first THz QCL by bandgap engineering, making QCL a THz source. From then on, THz QCL stimulates strong competition for new designs and fabrication techniques [30-32].

Terahertz quantum cascade lasers have shown considerable development over the last few years, with operation extended to low frequencies [33], sub-wavelength dimensions [34,35] above liquid nitrogen temperature operation [36,37].

Current challenges, however, include further performance improvements and an understanding of the fundamental gain and loss mechanisms within the QCL. To achieve these goals, novel characterization methods are required to determine key parameters such as the spectral gain and losses, as well as the dynamics that governs the QCL[38,40]. *Karl Unterrainer* et al.[41,42] first succeeded in measuring the gain in THz QCL with THz-TDS. Considering the performances of THz-TDS, one can use it to measure the gain of THz QCL. After developing our own THz-TDS setup, we used it to study the gain in THz-QCL. Chapter 3 reports on the first results we obtained.

For practical reasons, part of this PhD work was done in France and part of it in China on a slightly different topic. The final chapter 4 concerns the ultrafast dynamics of AgCl nanocrystalss doped tellurite niobic glass. Tellurite glass possesses broad optical transparency, low melting temperature [43,44], and so they have become prospective nonlinear optical materials for photonic devices such as Raman amplifier [45-47], saturable absorber [48], photoluminescence and up conversion fiber [49-51], etc. Many researches indicate that tellurite glass exhibits large nonlinear refractive index (n_2) with femtosecond response time, 40 times larger than that of the silicate glass, and it is a potential candidate in ultrafast optical switching [49]. Recently, many efforts have been made for enlarging n_2 and increasing its transparency by varying the composition of tellurite glass. Moreover, tellurite glass has good nonlinear absorption β, and it can be used as a potential candidate of optical power limiter.

Since 1980s [53-56], semiconductor nanocrystalss doped glass (SDGs) rise important attention due to exciton enhancement induced colossal nonlinear refractive index n_2. However, their temporal response is generally in the picosecond range, accompanied with large absorption coefficients [53], which diminishes the figure of merits for optical switching. In order to enlarge n_2 at transparency region of glass, a new effort is made to implant nanocrystals inside glass matrix. *Cotter et al*. [57] first studied large n_2 at non-resonant region of SDGs, and then most efforts [53,54,58~60] concentrated on the n_2 enhancement of silicate glass doped with II-VI compound nanocrystals such as CdS, CdSe, CdSSe, CdTe, etc. and much larger n_2 than silicate glass can be obtained by implanting semiconductor nanocrystalss inside tellurite host matrix. Compared with silicate glass, tellurite glass has much higher n_2, and so good tellurite

glass with rather larger n_2 can be obtained by implanting semiconductor nanocrystalss inside tellurite host matrix. Taking account of the glass transition temperature (450°C) of the tellurite host matrix, the I-VII compound AgCl with lower growth temperature than that of II-VI compounds is doped inside tellurite niobic glass matrix. To our knowledge, there is no report on the AgCl nanocrsytal doped tellurite glass, and furthermore, its nonlinear absorption coefficient and optical limiting have not been investigated.

In this last chapter 4, AgCl nanocrystalss doped niobic tellurite glass ($80TeO_2$-$20Nb_2O_5$) are prepared with melting-quenching and thermal treatment method. The AgCl nanocrystals structural properties are investigated with high-resolved transmitted electron microscopy (HRTEM) and scan field-emission scanning electron microscopy (FESEM). The UV-visible absorption spectrum was measured by absorption spectrometry, and the non-resonant third-order nonlinear susceptibility $\chi^{(3)}$ was measured by degenerate four wave mixing (DFWM). The optical limiting and nonlinear absorption were investigated by Z-scan technique.

Chapter 1

Principle of THz-Time Domain Spectroscopy

1.1 Introduction

In the chapter 1, we first describe the essential parts of a standard THz-Time Domain Spectroscopy (THz-TDS) set-up. Fig. 1.1 is a schematic diagram of a THz-TDS spectrometer, which is based on the pump-probe like geometry. It consists in a femtosecond laser source, a beam-splitter, a variable delay line, a THz emitter, THz collimating components and a THz detection system. A computer controls the acquisition as well as the displacement of the delay-line.

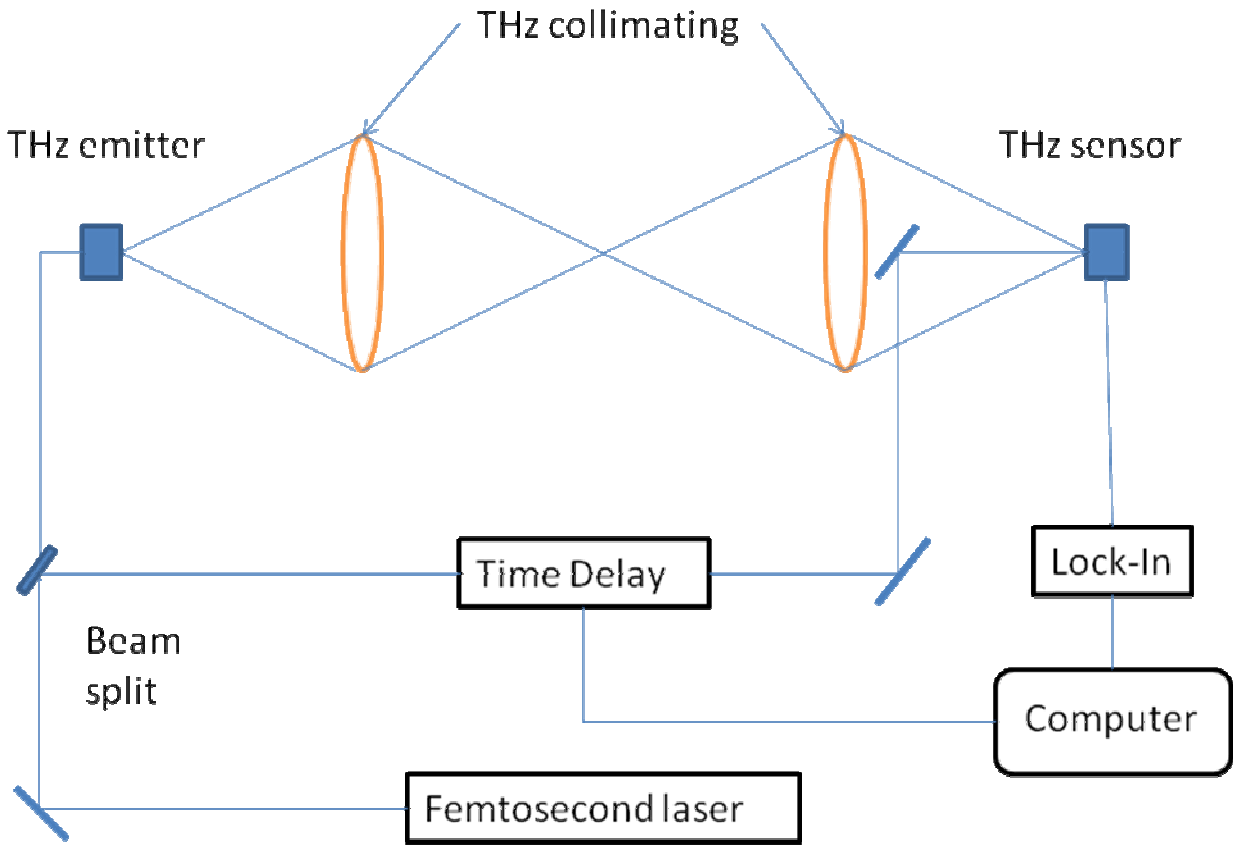

Fig. 1.1 Schematic diagram of a THz-TDS spectrometer

In the following, we describe (i) the typical THz generation methods that rely either on optical rectification of an ultrafast near-IR laser pulse in a nonlinear crystal, or on photoconductive antennas; (ii) after briefly reminding the principle and limits of the bolometric detection in the

context of our work, we describe the principle of THz detection using Free-Space Electro-Optic Sampling (FSEOS); (iii) the main characteristics of THz collimation components and (iv) the principle of the spectrum analysis.

1.2 THz generation

1.2.1 Optical Rectification

The optical rectification is a unique 2nd order nonlinear optical effect which appears in anti-centrosymmetric crystals [61-72]. Typical crystals are <110> zinc telluride (ZnTe) or gallium phosphide (GaP). A near-IR ultrashort laser pulse is used to excite a transparent nonlinear crystal that emits a THz radiation. The THz emission from optical rectification is described diagrammatically in Fig. 1.2.

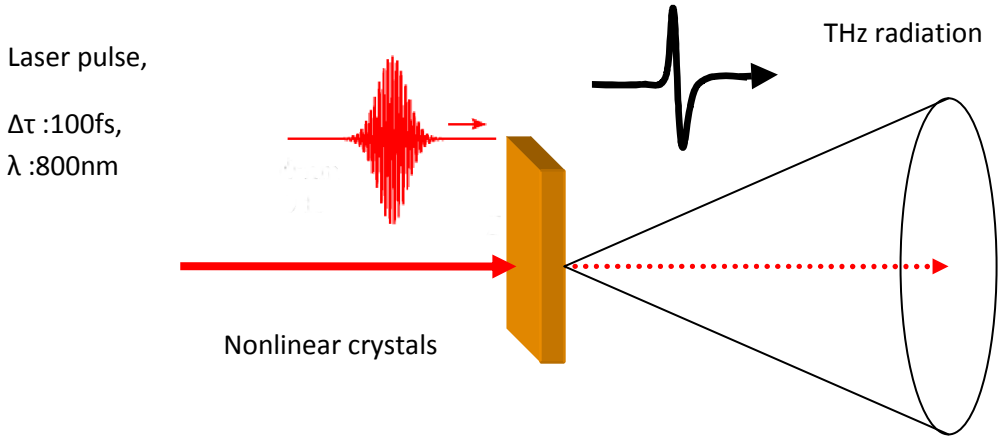

Fig. 1.2 Diagram of optical rectification and THz emission

Optical rectification can be seen as a difference frequency mixing between the frequency components given by the broadband near-IR laser pulse and occurs in media with a large second order susceptibility $\chi^{(2)}$. The nonlinear polarization induced in the material can be written as:

$$P^{(2)}(\omega=\omega_1+\omega_2)=\chi^{(2)}_{ijk}E_1(t)E_2(t)\cos(\omega_1 t)\cos(\omega_2 t)= \\ =\frac{1}{2}\chi^{(2)}_{ijk}(\omega)E_1(t)E_2(t)\left[\cos(\omega_1-\omega_2)+\cos(\omega_1+\omega_2)\right]=P^{(2)}_{OR}+P^{(2)}_{SHG}, \quad (1.1)$$

where P is the polarization, χ is the nonlinear susceptibility, E is the electric amplitude of incident beam. The subscript OR and SHG correspond to the optical rectification and second harmonic generation term. The above equation shows that optical rectification is directly

proportional to the incident wave intensity, and is in general time-dependent. Because of the dispersion in the nonlinear crystal, the phase matching condition is wavelength limited. Second harmonic generation is inevitable, but since the beams probe different refractive indexes, the phase-matching condition is different. Besides phase matching, the generated THz spectrum is affected by the laser pulse duration, the crystal absorption and thickness. As shown in Chapter 2, a typical THz-TDS system based on commercial 100-fs Ti:sapphire laser generates frequencies up to 3-4 THz (frequencies up to 50 THz can be reached with shorter pulses and adapted crystals). Last, we note that since optical rectification relies on high intensity laser pulses and since the nonlinear crystal is excited in its transparency region, this technique is very well suited to excitation with amplified Ti:sapphire lasers (using an regenerative amplifier). Photoconductive antennas tend to provide better results when working with an non-amplified system. More details about optical rectification can be found in Appendix A.

1.2.2 Photoconductive Antenna

Photoconductive antennas are very popular for generating and detecting THz pulses [73-74]. Here, a semiconductor (typically GaAs) is excited across the bandgap by a near-IR laser pulse to generate carriers (electron-hole pairs) that will be accelerated by an applied bias voltage [74-93]. The bias accelerates the newly formed carriers, yielding a transient current (the insulating system becomes conductor). The THz bandwidth is here firstly limited by how fast the carriers can be accelerated or by the carrier lifetime, rather than by the laser pulse duration. Short carrier lifetime can be achieved using low-temperature (LT) or semi-insulating (SI) GaAs. This type of source is typically used with oscillator-only, i.e., non-amplified systems. A generic setup is shown in Fig. 1.3.

For applying the bias, transmission lines are deposited lithographically onto an undoped GaAs wafer. The parallel metal strips of the transmission lines are separated by a certain distance that can range from few μm to centimetres (depending on the required field and input laser power). A dc bias voltage (typically tens of Volts) is applied across the gap via wires bonded to pads at the end of each strip with indium metal. When a near-IR pulse from the Ti:sapphire illuminates the semiconductor surface between the metal strips, the acceleration of the photocreated electrons in the dc field radiates a sub-picosecond THz pulse, which is usually

collimated by a crystalline quartz or silicon hyperhemispherical lens and off-axis paraboloidal mirrors.

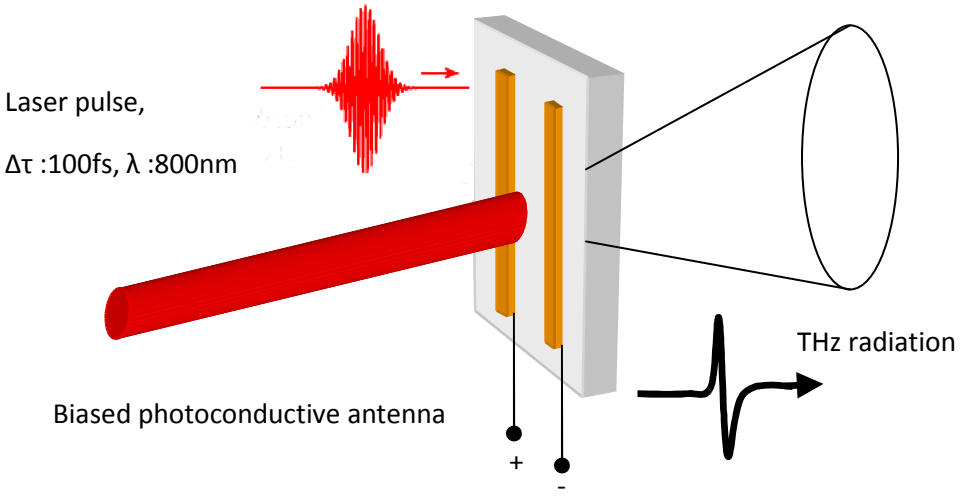

Fig. 1.3 Diagram of THz emission from photoconductive antenna

The acceleration of carriers in the bias field is the most critical aspect of the problem for THz emission. This is the process that determines the temporal evolution of the initial transient photocurrent. It can be regarded as involving an initial ballistic acceleration of the carriers on a time scale shorter than the carrier scattering time, followed by an approach to the drift velocity. At low carrier densities and room temperature, phonon-scattering dominates the scattering process and the scattering time typically does not exceed a few tenths of a picosecond. The carrier-carrier scattering time may also be important when considering transport phenomena, since these collisions can change the momentum in the electron or hole subsystem. Electron-electron scattering, although it does not contribute to the current relaxation due to momentum conservation, plays an important role in establishing thermal equilibrium among the electrons. The carrier scattering rate is the key parameter in the description of transport. Carrier acceleration subsequent to photo-generation of an ensemble of carriers will persist for a time on the order of scattering time as the steady-state carrier drift velocity is reached. This behavior is captured in the time-dependent mobility function of carriers (see appendix B).

1.3 THz Detection

1.3.1 Bolometric detection

Traditional bolometric detection allows measuring the total energy of a THz pulse and not the amplitude of the THz electric field over time, as in FSEOS. As a consequence, bolometric detection is not suited for THz-TDS. Nevertheless, we used a bolometer to realize part of the work accomplished during this PhD and this paragraph is dedicated to briefly describe the principle this detection technique. A bolometer measures the variation in the radiation absorption and converts this into a measurable quantity such as a voltage or current [94-98]. It can be used to measure the radiation for most wavelengths. However, for sub-millimeter wavelengths (from around 200 μm to 1 mm wavelength), the bolometer is the most sensitive type of detector for any measurement (though records with free-space electro-optic sampling have shown that this technique can be comparable). Typically, a bolometer consists of an absorber and a thermometer of heat capacity C, connected by a small thermal conductance G, to a heat sink held at a fixed temperature T_0 (Fig. 1.4 : left). The energy E of the incident radiation is converted into heat in the absorber, leading to a temperature rise $T = T_i - T_0 = E/C$, until the radiation power flowing into the absorber is equal to the power flowing into the heat sink through the weak thermal link. The temperature rise is subsequently measured and is directly proportional to the deposited energy. Suppose an incident electromagnetic radiation with frequency ω is absorbed by the bolometer, the temperature will be modulated by $T_{bolo} = T_0 - T_1 e^{i\omega t}$ where T_0 is equal to $T_0 = T_s + T_0/G_0$ and $T_1 = Q_1/G(\omega)$. In the bolometer, it composes of two processes: energy dispersion and storage.

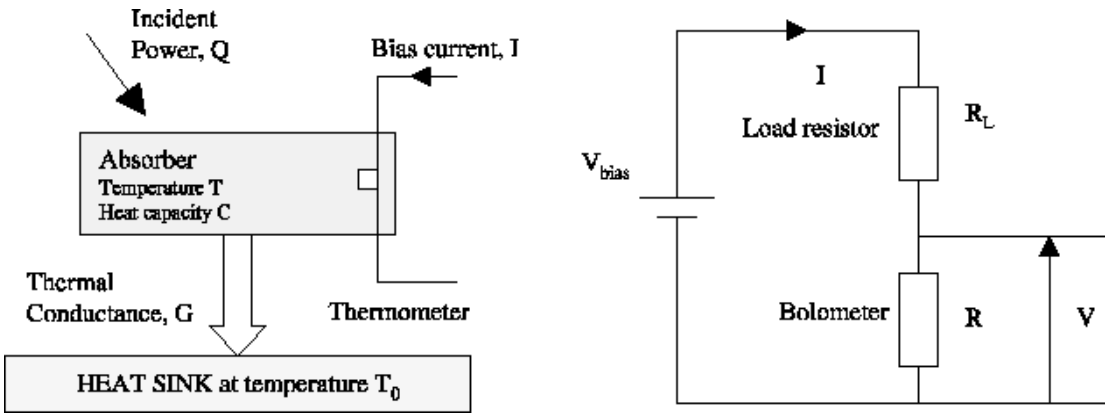

Fig. 1.4 Diagram of bolometric detection

The first process can be written as:

$$Q_{dis} = G_0(T_0 - T_s) + G(\omega)T_1 e^{i\omega T}, \tag{1.2}$$

and the storage process by:

$$Q_{stock} = \frac{d}{dt}\left[C \cdot (T_{bolo} - T_s)\right] = i\omega C T_1 e^{i\omega T}, \tag{1.3}$$

The balance equation of bolometer is:

$$Q_0 + Q_1 e^{i\omega T} + I^2 R_0 + I^2 \frac{dR}{dT} T_1 e^{i\omega T} = G_0(T_0 - T_s) + G(\omega)T_1 e^{i\omega T} + i\omega C T_1 e^{i\omega T}, \tag{1.4}$$

The sensitivity expression is then:

$$S = \frac{V}{Q_1} = \frac{dR}{dT} \cdot T_1 \cdot \frac{1}{P_1} = \frac{I\frac{dR}{dT}}{\left[G - I^2 \frac{dR}{dT} + i\omega C\right]}, \tag{1.5}$$

From this expression, one can conclude that the sensibility is related to the load resistance R_L and $R_L >> R$.

1.2.2 Free-space electro-optic sampling

Two common detection techniques are used in THz-TDS: electro-optic or photoconductive sampling. In both techniques, a reference near-IR pulse (from the same laser source as the one that generates the THz pulses) illuminates the detection system at the same time and position as the THz pulse to be detected. The detection system will then react differently depending on the value of the *amplitude* of the THz electric field. These techniques are coherent and as a consequence the noise is low (the time window of the measurement is very small). With respect to the bolometric detection, the advantages are (i) the system does not need to be cooled to cryogenic temperatures (ii) the detection is insensitive to incoherent radiation (thermal noise) (iii) the detection provides the complex THz electric field and not only the intensity. Photoconductive sampling relies on similar principles as photoconductive emission (but in a reversed process) and will not be discussed here. We will concentrate on FSEOS which was used in the present work.

The schematic diagram of FSEOS[99-105] is shown in Fig. 1.5 and briefly described in the following. The crystal used for the generation by optical rectification can be used for the detection relying here on the Pockels effect. A reference near-IR pulse is incident on an optical bridge: the linear polarization of the laser beam is transformed into a circular polarization by a λ/4 waveplate. A Wollaston prism separates the parallel and horizontal polarization components. The two resulting beams are sent onto a photodiode balance. In the absence of THz radiation and when the system is correctly aligned, the difference in intensity onto the two photodiodes is zero. In the presence of a THz electric field (arriving at the same time and position as the near-IR pulse), the polarization of the reference beam is modified by Pockels effect, resulting in an intensity difference between the photodiodes. The difference in intensity is proportional to the *amplitude* of the THz electric field. By changing the position of the delay line, one can then reconstruct the temporal evolution of the THz field. More details can be found in Appendix C.

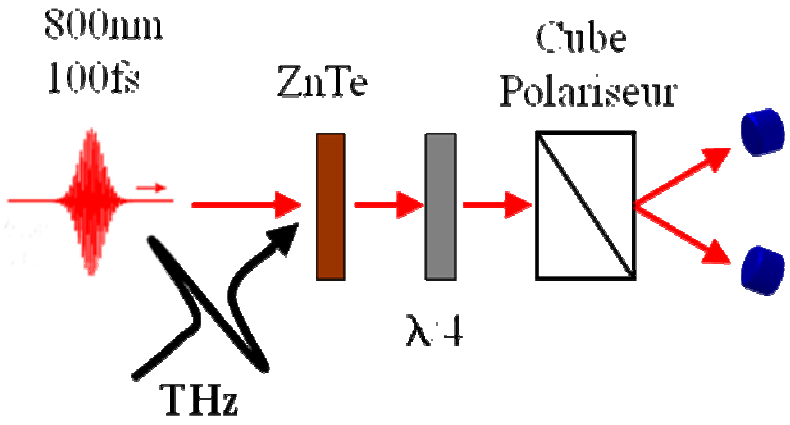

Fig. 1.5 Diagram of Free Space Electro-Optic Sampling (FSEOS)

The incident THz pulse induces a birefringence in the ZnTe crystal, which gives rise to a phase retardation of the linearly polarized probe laser beam, described as follows:

$$\begin{aligned} n_x &= n_0 + \frac{1}{2} n_0^3 r_{41} E_{THz} \\ n_y &= n_0 - \frac{1}{2} n_0^3 r_{41} E_{THz} \\ n_z &= n_0 \end{aligned} \quad , \qquad (1.6)$$

$$\Gamma_{THz} = \frac{2\pi l}{\lambda}\left(n_x - n_y\right) = \frac{2\pi l}{\lambda} n_0^3 r_{41} E_{THz}, \qquad (1.7)$$
$$\Delta I = I\Gamma_{THz}$$

By recording the phase retardation, the THz field amplitude can be detected. Both the polarization of THz pulse and probe laser beam are aligned parallel to [110] direction of ZnTe sensor crystal. The Wollaston prism behind the λ/4 wave-plate converts the THz-induced phase retardation of the probe beam into an intensity modulation between the 2 perpendicularly polarized probe beam components. The difference signal is feed back to the lock-in amplifier referenced at a frequency chopping the pumping optical beam to generate the THz radiation.

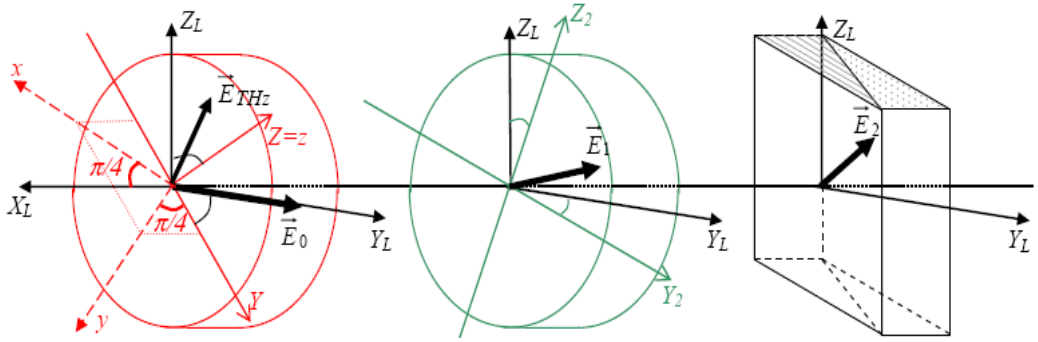

Fig. 1.6 Diagram of THz detection in FSEOS

In FSEOS, there is a clear trade-off between the sensitivity and frequency response that is determined by the thickness of ZnTe sensor crystal. A thicker crystal produces a greater interaction length, but on the other hand it reduces the detection bandwidth due to group-velocity mismatch. The most distinct advantages of FSEOS are broad-bandwidth detection range and ease of implementation. The shortcoming of FSEOS is that it is very sensitive to laser noise and low-frequency mechanical and acoustical disturbances.

1.4 THz Collimation

1.4.1 Lens collimation

This method is in principle equivalent to the using lenses in geometric optics. However, the lens materials need to be transparent in the THz range. The refractive index n_{THz} and absorption coefficient α_{THz} within the THz frequency range become the key parameters (see Table 1).

Table 1.1 Refractive index and absorption coefficient of THz transparent materials [2]

Materials	n_{THz}	$\alpha_{THz\ (cm^{-1})}$
TPX	1.48	<0.01
Picarin	1.56	<0.01
Sapphire	3.04	<4
High-resistivity Silicon	3.42	<0.1
GaAs	3.59	0.1~3

High-resistivity silicon is silicon with high intrinsic resistivity ρ=10kΩ.cm. Polymer materials display lower absorption at THz frequencies than inorganic solid. Picarin has the advantage of having the same refractive index in the THz range as in the visible, which allows easier alignment of the system (but the material is soft, fragile and polishing into lens shapes remains difficult and expensive).

1.4.2 Parabolic collimation

The most common technique to collimate the THz diverging radiation is to use off-axis parabolic mirrors. Four off-axis parabolic mirrors are typically needed in a THz-TDS set-up. Alternatively, two ellipsoidal mirrors can be used since they offer two focal points at finite distance. Nevertheless, parabolic mirrors are easier to manipulate.

1.5 Analysis of the THz spectrum

The paragraph briefly describes a method to extract physical parameters from a THz-TDS spectrum. THz time domain spectroscopy allows measuring the transmission through a material, giving access to physical parameters by measuring the complex function T(ω) [106-109]. It is obtained by measuring the THz beam going through the sample and a reference beam bypassing it:

$$T(\omega) = \frac{E_{Sam}^{THz}(\omega)}{E_{ref}^{THz}(\omega)}, \tag{1.8}$$

where $E_{ref}(\omega)$ is the transmitted THz radiation in free space and $E_{sam}(\omega)$ is the sampling THz radiation. The transmitted complex function is composed of different frequency components so that one can extract the phase and amplitude of sampling signal by Fourier transformation. This function contains the physical material parameters through the complex refractive index: $\tilde{n} = n - i\kappa$. The real and imaginary parts can be deduced by calculation from the transform function T(ω):

$$T(\omega) = \frac{A_2(\omega)}{A_1(\omega)} \exp[-i(\phi_2(\omega) - \phi_1(\omega))], \tag{1.9}$$

where A(ω) and ϕ(ω) correspond respectively to the magnitude and phase of the THz beams. With d the thickness of sample, n the refractive index and α the absorption coefficient, one can deduce:

$$n(\omega) = 1 + \frac{c}{2\pi f d}(\phi_2(\omega) - \phi_1(\omega)), \tag{1.10}$$

$$\alpha(\omega) = \frac{-1}{d} \ln\left(\frac{A_2(\omega)}{A_1(\omega)}\right), \tag{1.11}$$

Chapter 2

Development of THz-Time Domain Spectroscopy

2.1 Introduction

In Chapter 1, we reminded briefly the basic concepts of THz-Time Domain Spectroscopy. In this Chapter 2, we present the THz-TDS system that we developed in the laboratory. We describe the laser source, the alignment and the signal optimization procedures. As reported above, THz generation can be achieved either by optical rectification of by using photoconductive antennas. Here, the two methods are tested. Concerning the first method, we investigate in particular the competition between optical rectification (in <110> ZnTe) and other non-linear processes. Upon focusing, for excitation sizes smaller than the THz wavelength, Second Harmonic Generation (SHG), Two Photon Absorption (TPA) as well as Free Carrier Absorption (FCA) are observed while THz emission is strongly reduced. While TPA is responsible for the optical pump depletion, we find that FCA cannot be neglected as often assumed in the past. Both contributions are found to be of the same order of magnitude. The conditions for the most efficient THz generation are described. Then, we study THz generation in an *interdigitated* SI-GaAs photoconductive antenna. As compared to traditional photoconductive antennas, this new scheme allows generating THz on a large surface (thus minimizing diffraction effects), under the application of a moderate bias voltage. The structure is characterized versus temperature and exciting carrier density.

2.2 Ultrafast Laser Source

Optical rectification, photoconductive antennas and free-space electro-optic sampling are driven by femtosecond pulse laser excitation. Our Laser system is composed of a Coherent Verdi-V8 solid-state pump laser (wavelength: 532nm, output power: 8W) and a Coherent MIRA900F Ti:sapphire oscillator (center wavelength: 800nm, medium pulse duration: 100fs, repetition rate: 76MHz).

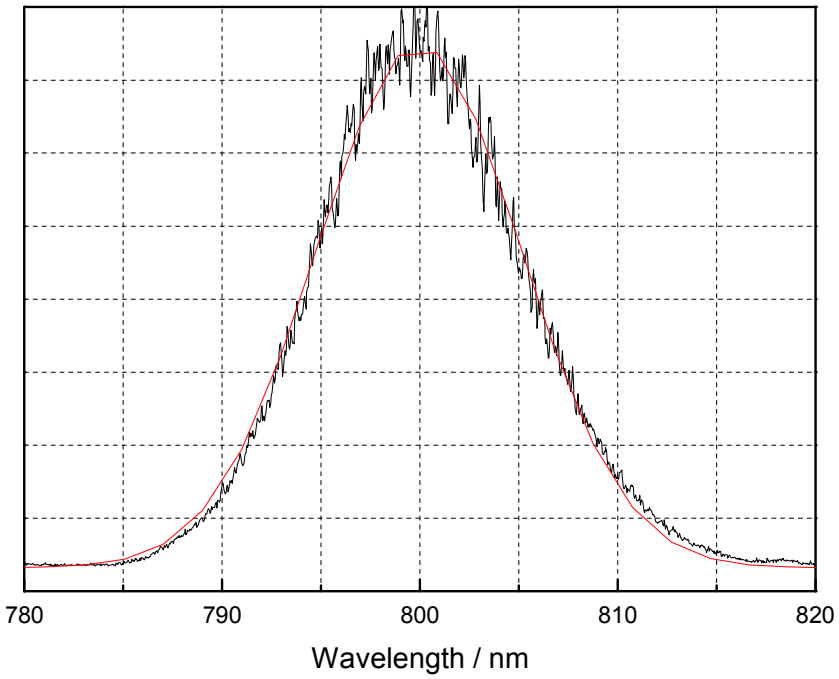

Fig. 2.1 Laser pulse spectrum

The full width at maximum height (FWMH) of the laser pulse spectrum is about 15nm. Assuming the pulse is Fourier-Transformed limited, one can deduce the pulse duration. The typical pulse duration is 100fs. The particular optics and birefringent filter (for wavelength selection) chosen in this laser system allow to reduce the pulse duration to below 80 fs when necessary. The output power is usually maintained at 1.5W (mode-locked).

2.3 THz-TDS with ZnTe emitter

2.3.1 Alignment of THz-TDS

The scheme of our THz-TDS system is shown as follows in Fig 2.2. In the case of optical rectification with a <110> ZnTe crystal emitter, the pump beam is modulated by a mechanical chopper. In the case of photoconductive antennas, an Agilent functional generator drives the antenna (at a frequency which triggers the Lock-In simultaneously). The laser beam is focused onto the surface of THz emitter with a 4cm focus lens. As discussed in details in the next section, for optical rectification, optimum THz generation is achieved when the ZnTe crystal is slightly out of focus. Off-axis parabolic mirrors (PM) collimate the parallel beam.

The PMs used in the present work (Janos) have a 100mm diameter, 15.2cm focal length and 90° angle. The four PMs are positioned on xy-stages in order to adjust the distance between emitter and PMs. The focus of first PM has to overlap with the light spot on the THz emitter. In practice, this adjustment can be achieved by replacing the THz emitter by tracing paper, which diffuses the incoming laser beam and makes the alignment easier. In order to recombine the THz beam and the probe beam collinearly into the ZnTe sensor, one can use a pellicle beam splitter (between mirror M5 and the sensor A) which reflects the near-IR beam while transmitting the THz radiation. Nevertheless, a pellicle beam splitter is generally sensitive to mechanical vibrations which easily induce additional noise. An alternative solution consists in using a small (2x2mm) metallic mirror which is more stable and which shadows only a little part of the THz beam.

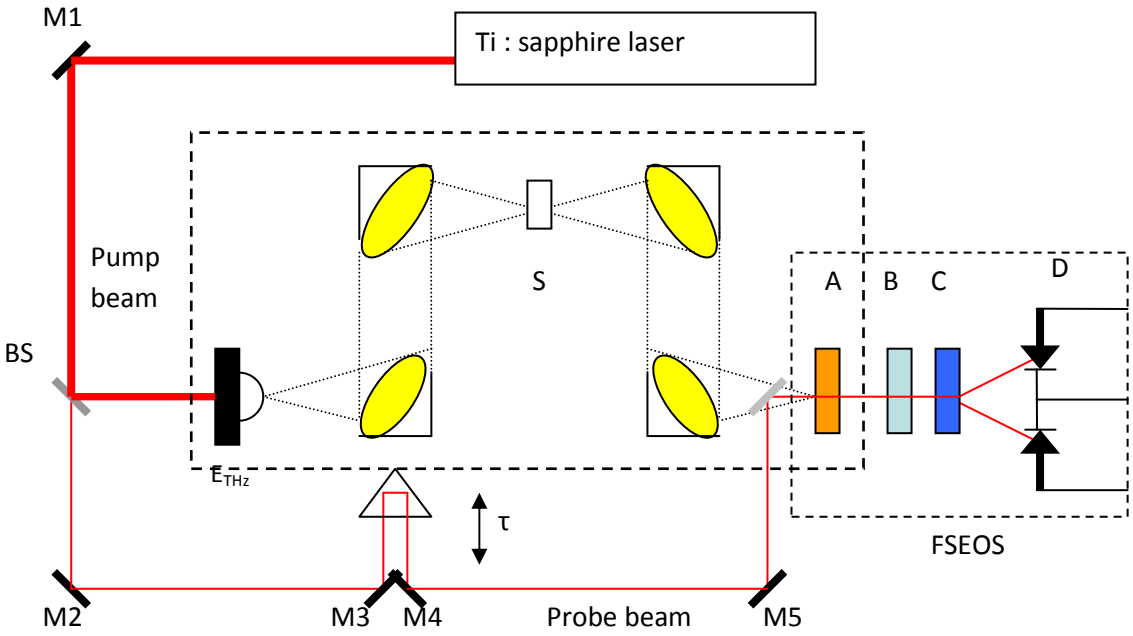

Fig. 2.2 Schematic diagram of THz-TDS; S: sample, M: mirror, BS: beam-splitter, τ: time delay, E_{THz}: THz emitter (ZnTe crystal or photoconductive antenna), A: ZnTe sensor, B: λ/4 waveplate, C: Wollaston prism, D: balanced detector.

The water present in the atmosphere strongly absorbs the THz radiation. An air-tight box, filled in with nitrogen gas or dry air, was fabricated. It comprises all the optical components from the emitter to the ZnTe sensor.

The final step is to determine zero time delay and spatial overlap between the probe beam and the THz beam onto the ZnTe sensor. At this stage, the alignment procedure is very difficult: (i) the pre-alignment of the PMs may not be good enough, (ii) the focalization of the THz spot on the ZnTe sensor may not be optimum, (iii) for a first use of the ZnTe sensor, its neutral axis may not be known, (iv) the spatial and temporal is not determined yet, (v) the expected THz signal is weak. In a preliminary alignment, the spatial-temporal overlap is approached by performing an autocorrelation measurement. This is done by removing the THz emitter and replacing the ZnTe sensor by a type-I BBO crystal (0.5 mm). The autocorrelation measurement is then performed between the near-IR pump and the probe beams. The autocorrelation intensity is given by:

$$A(\tau) = \int_{-\infty}^{+\infty} I(t) I(t-\tau) dt \,, \tag{2.1}$$

The signal generated in the second-harmonic-generation crystal is proportional to $(E(t)+E(t-\tau))^2$. Only the beam propagating on the optical axis, proportional to the cross-product $E(t)E(t-\tau)$ are detected (see Fig. 2.3). This signal is then recorded by a slow detector, which measures

$$I_M(\tau) = \int_{-\infty}^{+\infty} \left| E(t) E(t-\tau) \right|^2 dt = \int_{-\infty}^{+\infty} I(t) I(t-\tau) dt \,, \tag{2.2}$$

$I_M(\tau)$ is the intensity autocorrelation $A(\tau)$.

For a Gaussian time profile, the autocorrelation width is $\sqrt{2}$ longer than the width of the pulse (and 1.54 longer in the case of an hyperbolic secant squared (sech2) pulse).

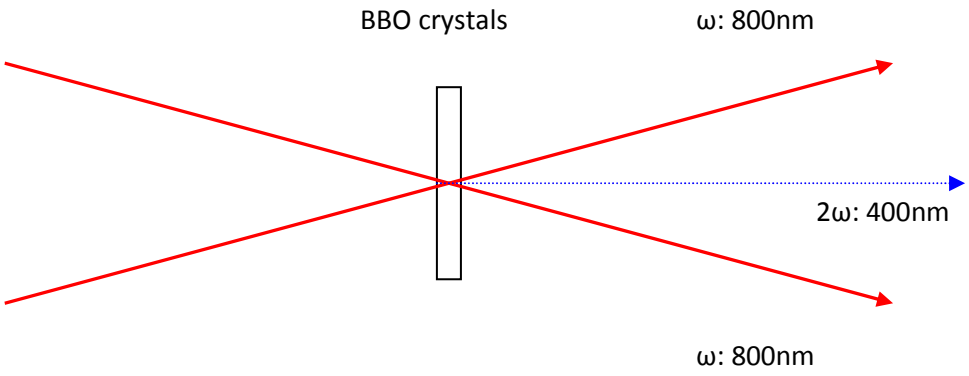

Fig. 2.3 Diagram of the auto-correlation geometry

The SHG signal was detected with a photon multiplier (PMT) driven at a voltage of 1KV. The autocorrelation second harmonic generation signal (SHG) is shown in Fig. 2.4. The pulse duration is typically 100 fs in the experiments presented in this work.

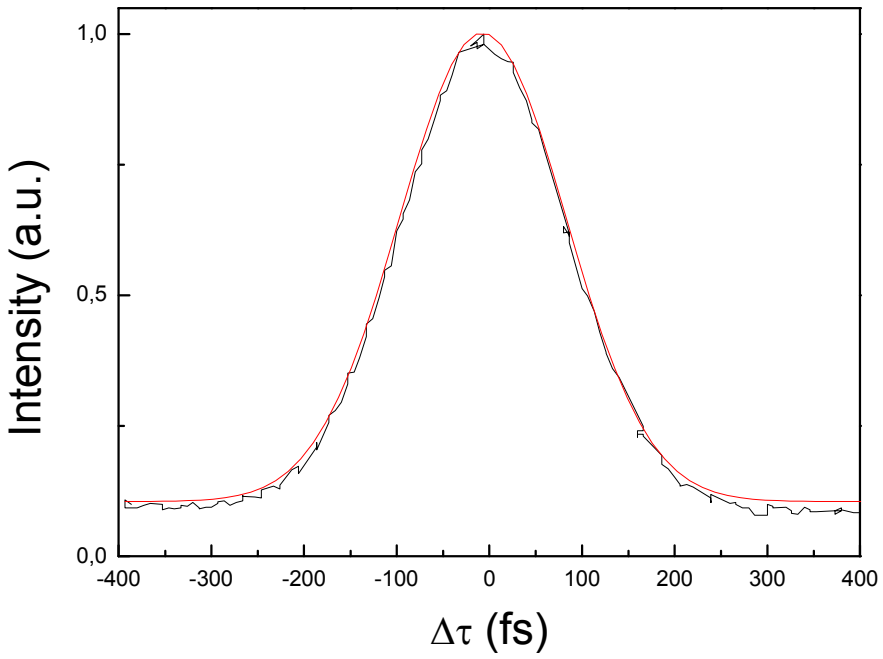

Fig. 2.4 The SHG intensity autocorrelation at zero time delay

2.3.2 Signal-to-Noise Ratio optimization

The optimization of the signal-to-noise (SNR) ratio is critical in THz-TDS experiments. Obtaining record SNR ratio (that can reach values as high as 10^6 to 10^7) is not the goal of the present work. Common values of the S/N typically reach 10^4 to 10^5 after a careful optimization. We underline here the several problems that we met while searching for the first THz signal and optimizing the SNR:

- The THz beam and the probe beam can be recombined collinearly into the ZnTe sensor with a pellicle beam splitter (which reflects the near-IR beam while transmitting the THz radiation: see Fig. 2.2) or a small mirror. Nevertheless, a pellicle beam splitter was found to be very sensitive to mechanical vibrations. We chose to use a small (2x2mm) metallic mirror which is more stable and which shadows only a little part of the THz beam. The SNR was improved from 15μV/Hz to 0.4μV/Hz.

- The laser noise and stability was carefully checked with a spectrum analyzer. In optimum conditions, the laser noise is limited to the standard quantum limit (shot noise) at high frequency. High frequency modulation of the laser beam can be reached with an acousto-optic modulator. At the low frequency (kHz range) of a mechanical chopper, the situation is more critical. In our experiment, mechanical noise sources (induced by pumps or by the chopper itself) were identified using the spectrum analyzer, and reduced to a minimum.

- Important gas (nitrogen or dry air) fluctuations in the dry box induce additional noise. The gas pressure was controlled in order to minimize the noise.

2.3.3 Measurement of the THz focal area

The THz spot size was measured with a "knife-edge" technique as illustrated in Fig.2.5.

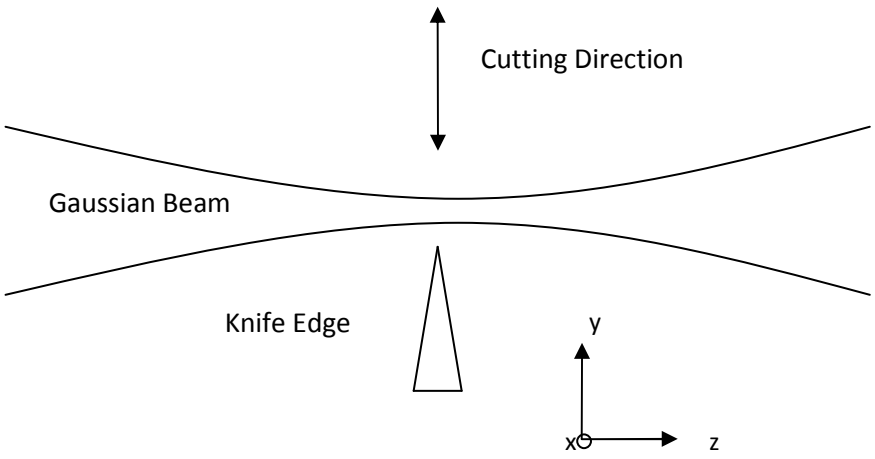

Fig. 2.5 Diagram of knife edge measurement technique

It consists of a micrometer motor-driven translation stage, to which is attached a single-edge razor blade. The razor passes through the focal plane of THz beam. The transmitted THz field is then measured by the FSEOS detection system. The details of the analysis are given in Appendix D. The beam diameter is exacted by derivation the transmission function. In order to extract the position of the THz focal plane, the measurement is performed for several position along the z-axis. The typical THz spot size is 400 to 500μm.

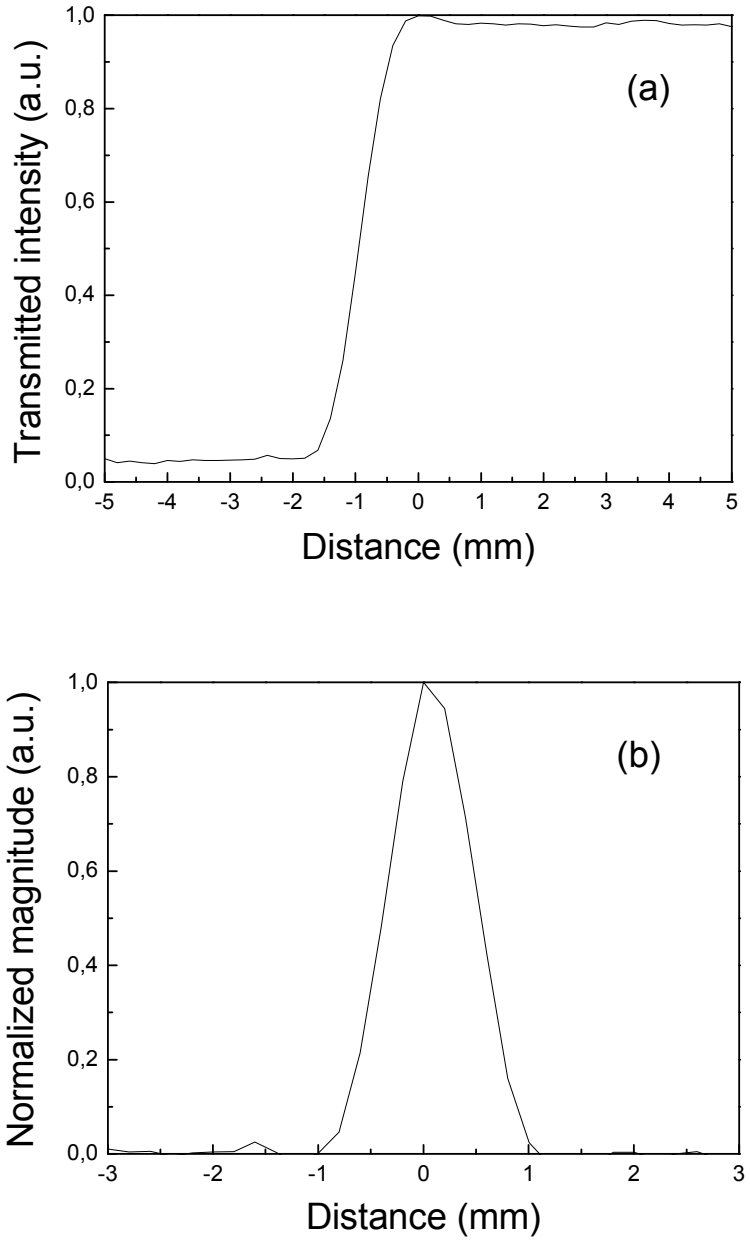

Fig. 2.6 Transmission function: (a) Transmission of THz at focal plane (b) Derivative of the transmission function at the THz focal plane.

2.3.4 Thickness influence of ZnTe emitter and sensor

ZnTe crystals have a large electro-optic coefficient, but a more compelling attribute is the velocity matching between the femtosecond optical beam in the wavelength vicinity of 800nm and the THz radiation [110-111]. The refractive indices of the near infrared beam (~800nm)

match very well with the dielectric constant in the THz range from sub-THz to several THz. This feature means that the thickness of ZnTe crystals has a limited influence on the walk-off effect and results in large conversion efficiency. However, the THz spectral bandwidth depends on the pulse duration and also on the phase matching. A laser pulse can generate a THz pulse with bandwidth twice as broad as the laser pulse itself. Therefore shorter laser pulses are expected to extend the bandwidth of the radiation. However, it is impossible to select an electro-optic crystal that fulfills the group velocity matching condition for all frequency components. In order to minimize walk-off between the THz and optical pulses, thinner crystals must be used. Suppose Ω is the THz frequency, and ω is the optical frequency. Then, the frequency response function for the phase-matched process [111] is

$$G(\Omega) = \frac{\exp(i2\pi\Omega\delta) - 1}{i2\pi\Omega\delta}, \tag{2.4}$$

where δ is the phase difference between the pump light and the THz light fo frequency Ω, given by

$$\delta = \frac{d}{c}\left(\sqrt{\varepsilon(\Omega)} - n_g\right) = \frac{d}{c}\Delta n, \tag{2.5}$$

Here, d is the thickness of ZnTe crystal, c is the light speed in vacuum, n_g is the group refractive index for the laser pulse, and ε(Ω) is the dielectric constant of the electro-optic crystal at the THz frequency Ω. The phase-matching equations are the same for electro-optic detection.

Besides the phase-matching condition, another important limitation factor is the "etalon" [112] (Fabry-Pérot like) effect of ZnTe crystals. An incident probe pulse passing through the ZnTe sensor is partially reflected by the internal facets of the crystal. During the sampling process, the THz signal is reconstructed temporally by a series of near-IR probe pulses. The sampling diagram is show in Fig. 2.7.

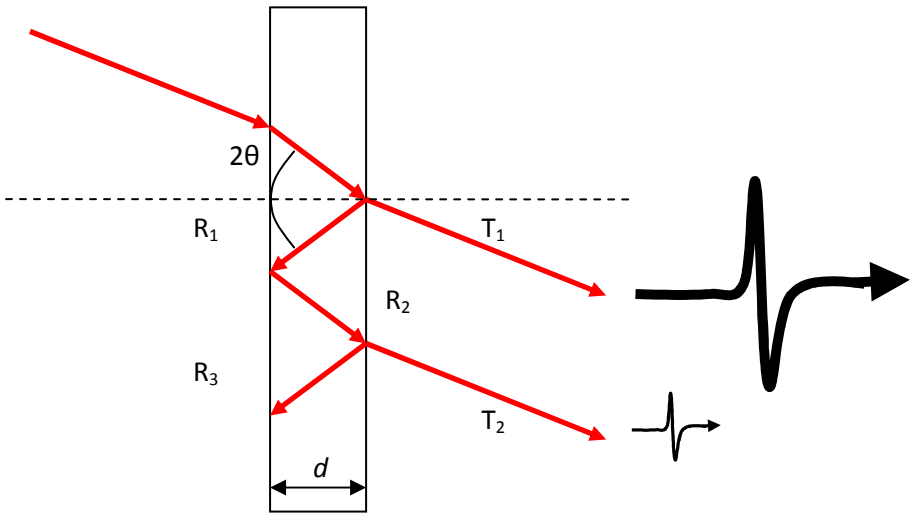

Fig. 2.7 Etalon effect in the ZnTe sensor crystal

In the THz-TDS spectra, this induces THz echoes following the major oscillation. In the example displayed in Fig. 2.8, we used a 1mm ZnTe crystal sensor and a 2mm ZnTe crystal as the emitter.

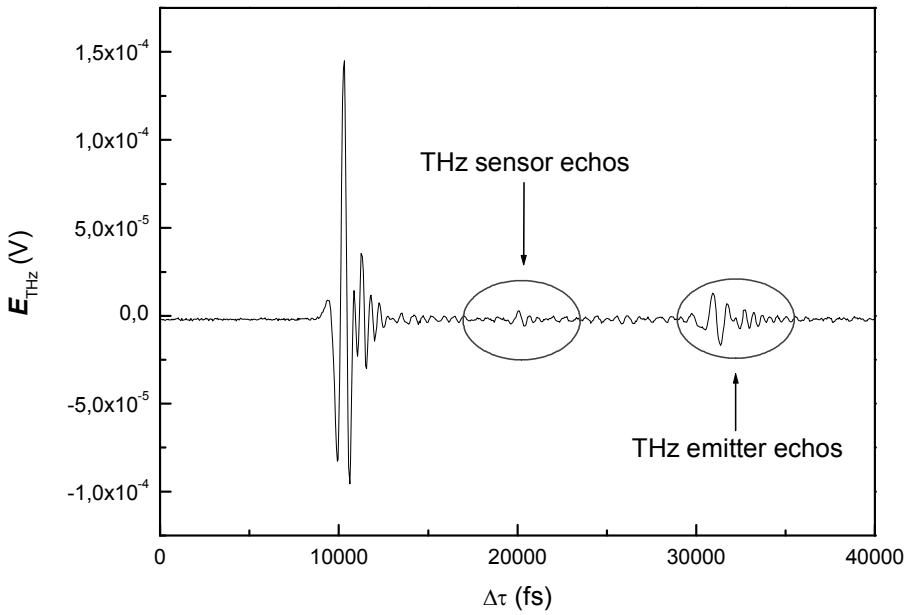

Fig. 2.8 Etalon effect induced THz echos in spectra

2.3.5 Water absorption and typical spectrum in dry atmosphere

THz radiations are easily absorbed by the water present in the air so that the terahertz time-domain spectroscopy has to be performed in a purged system (nitrogen or dry-air). To illustrate this, Fig. 2.9 shows a THz-TDS spectrum obtained in normal atmosphere (60% humidity). The spectrum contains about thirty strong lines in the given frequency range. The NASA catalog[113,114] allows identifying a majority of the lines.

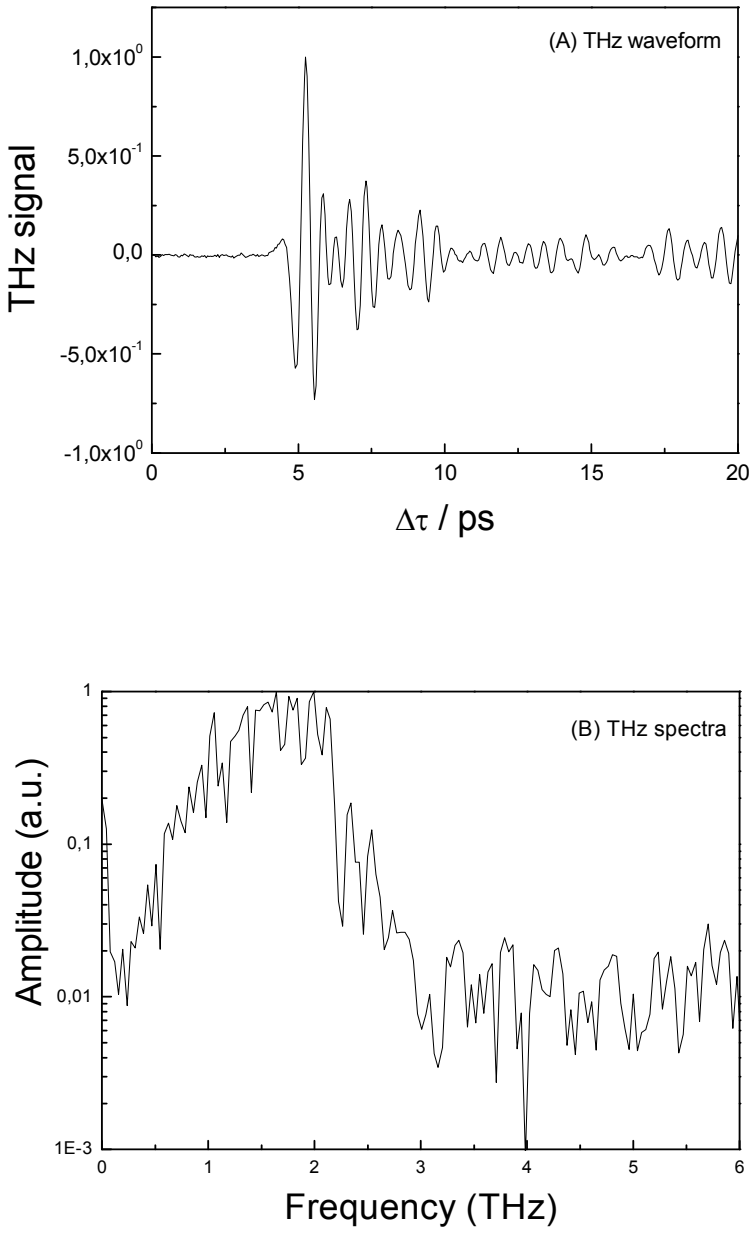

Fig. 2.9 (A) THz waveform and (B) THz spectrum in air

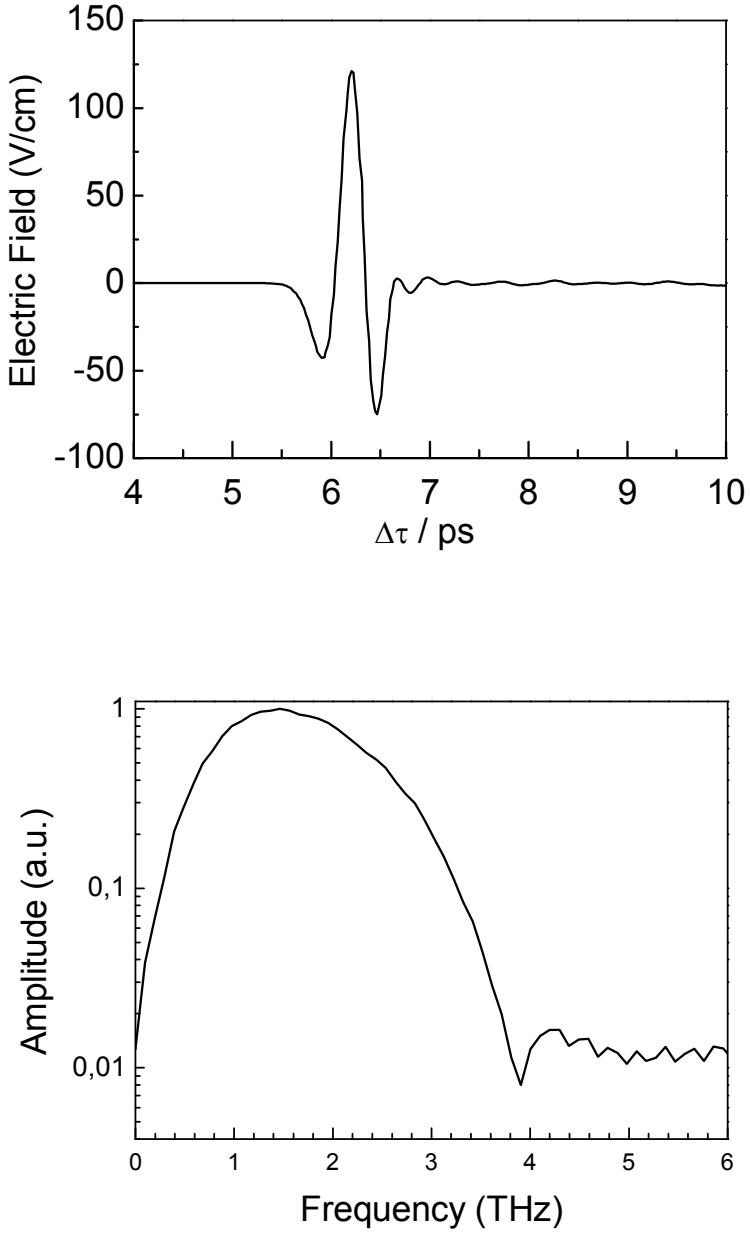

Fig. 2.10 (A) THz waveform and (B) THz spectra in dry-atmosphere

2.3.6 The competition of THz generation and nonlinear optical effect

(A) Experiment

The excitation of the <110> 2-mm-thick crystal was provided by a 800nm Ti:sapphire laser (100 fs pulses) at 300mW, using a 4cm focusing lens. The ZnTe crystal is virtually

transparent in the frequency domain of interest[19]. The detection of the THz radiation was performed by a liquid helium cooled bolometer.

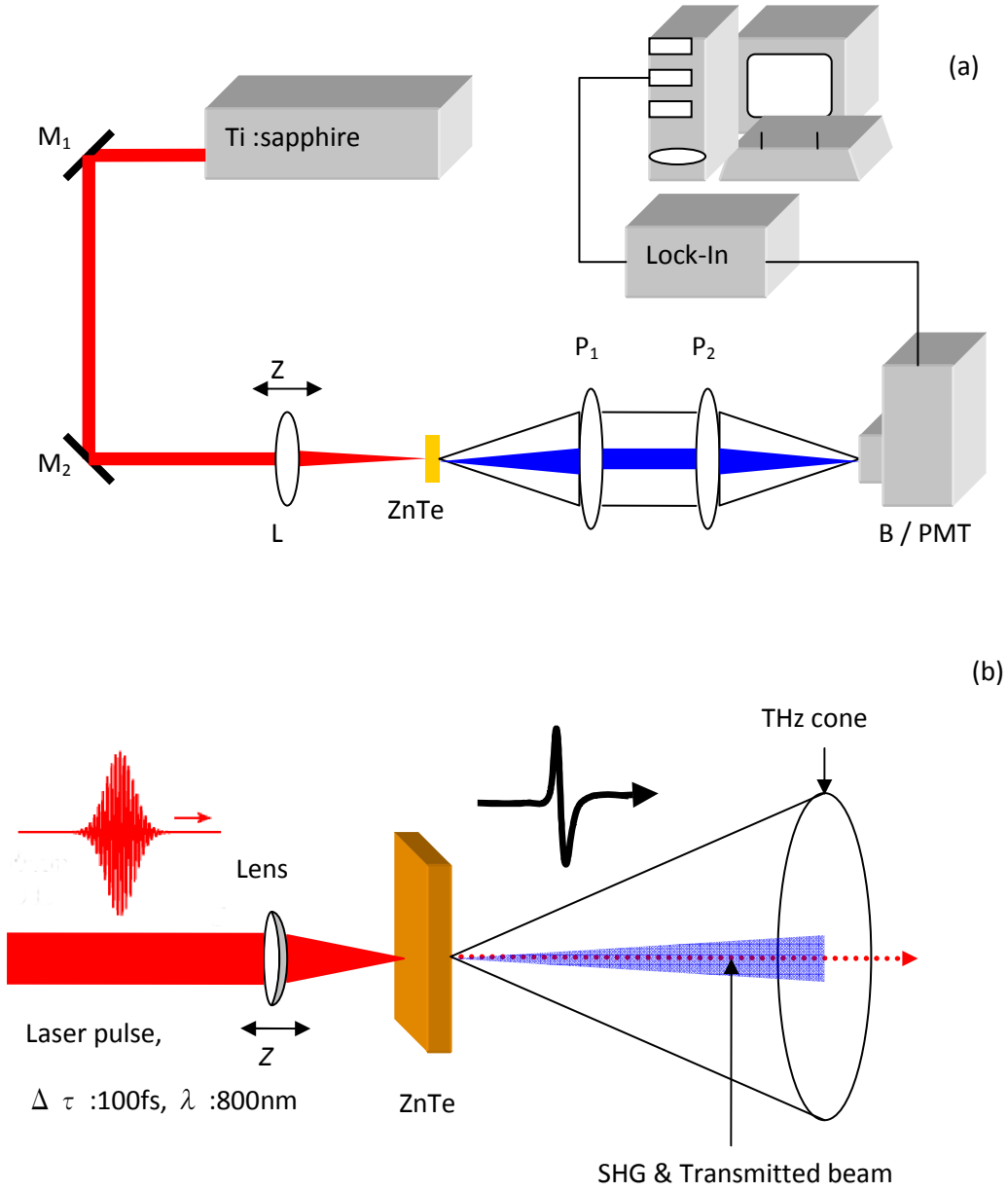

Fig. 2.11 (a) Schematic setup of nonlinear THz experiments; blue cone and line is the SHG signal; L: lens, C: ZnTe crystal, P: picarin lens, B: bolometer, PMT: photon multiplier tube; (b) Diagram of the THz Z-hole measurement.

For reasons that we'll discuss below, we performed as well a "two-color" experiment described in Fig. 2.12: a BBO crystal is placed at the focus of the near-IR beam and the ZnTe crystal is placed further on the z-axis.

The transmitted laser beam is measured with a silicon photodiode (OPA 5T), the SHG a photon-multiplier tube (PMT) associated with a blue pass filter.

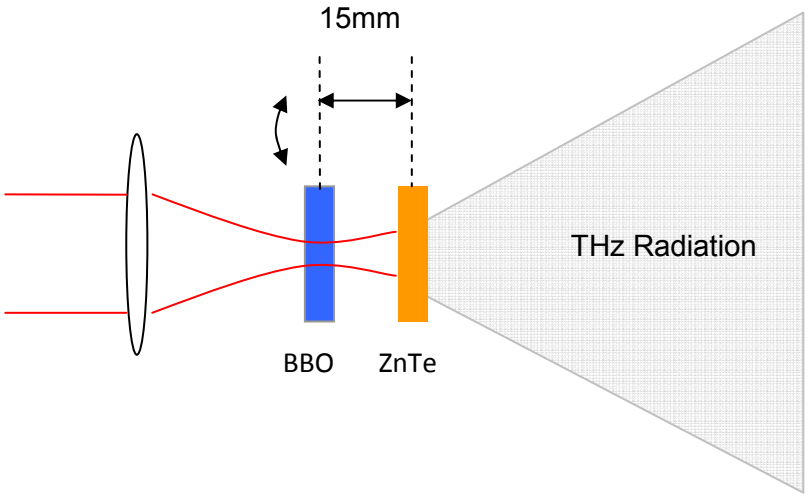

Fig. 2.12 Schematic setup the "two-colour" experiment.

(B) Result and Analysis

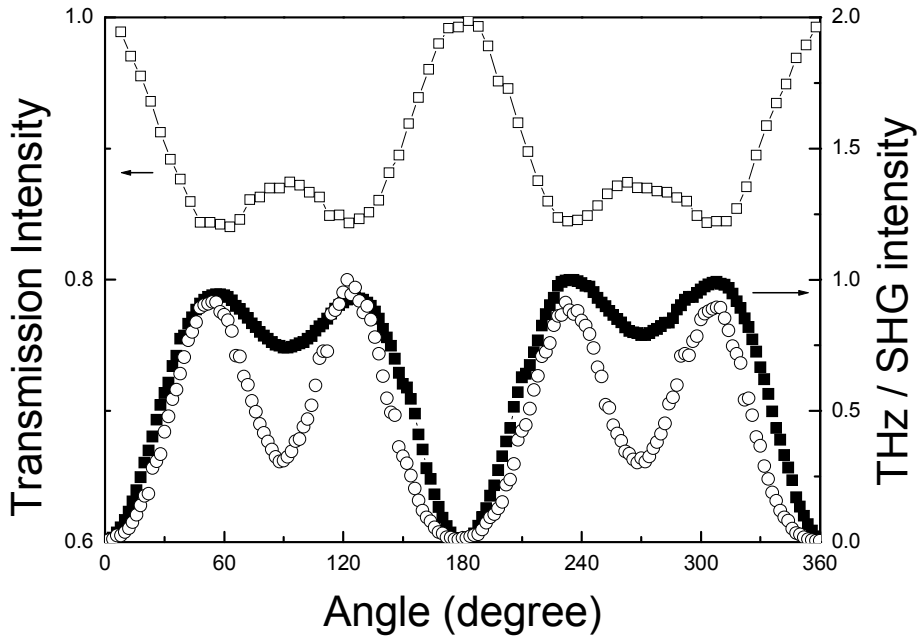

Fig. 2.13 Closed symbols: THz intensity as a function of the ZnTe azimuthal angle. Open circles: SHG intensity upon focusing. Open squares: transmission at 800 nm.

Fig. 2.13 shows the THz emission, SHG and the transmission laser beam as a function of the azimuthal angle of the ZnTe crystal. The THz emission and SHG have the same profile: extreme are obtained for the same angles and both intensities vary in the range from 0 to 100%. The transmission at 800 nm presents variations opposite of two previous ones: maxima of the transmission correspond to the minima of the THz radiation and SHG respectively. The attenuation of transmitted beam varies from less than 20%.

The THz and SHG intensities are proportional to the square of the nonlinear polarization which angle dependence is determined by the 2nd order nonlinear susceptibility tensor $\lfloor d_{ijk} \rfloor$ [116]. The linearly polarized optical pump beam is normally incident upon the <110> crystal and the angle between its electric field E(ω) and the <001> axis is noted θ. E(ω) is given by:

$$\mathbf{E}(\omega) = E_0 \cos\omega t \left(\frac{\sin\theta}{\sqrt{2}}; -\frac{\sin\theta}{\sqrt{2}}; \cos\theta \right), \tag{2.6}$$

The polarization associated to OR and SHG in crystallographic axis are described by:

$$\begin{aligned} P_i^{OR}(\omega_2 - \omega_1) &= \sum_{j,k} d_{ijk} E_j E_k \cos(\omega_2 - \omega_1)t \\ P_i^{SHG}(\omega_1 + \omega_2) &= \sum_{j,k} d_{ijk} E_j E_k \cos(\omega_1 + \omega_2)t \end{aligned}, \tag{2.7}$$

where the indices refer to the set $\{x, y, z\}$.

For a crystal with zinc-blende structure, such as ZnTe, the nonlinear susceptibility tensor is:

$$d_{il} = \begin{bmatrix} 0 & 0 & 0 & d_{14} & 0 & 0 \\ 0 & 0 & 0 & 0 & d_{14} & 0 \\ 0 & 0 & 0 & 0 & 0 & d_{14} \end{bmatrix}, \tag{2.8}$$

where the index l refer the Voigt notations.

The angle θ dependence of the THz and SHG intensities is then determined by the following expression:

$$I_{THz} \propto I_{SHG} \propto |\mathbf{P}|^2 \propto d_{14}^2 E_0^4 f(\theta) \text{ with } f(\theta) = \sin^2\theta\left(1 + 3\cos^2\theta\right), \tag{2.9}$$

In principle, optical rectification, SHG as well as TPA can be responsible for the optical pump depletion. Nevertheless, the optical rectification efficiency is only on the order of 10^{-7} and, as

already pointed out in previous studies [123], SHG generation is also inefficient in depleting the pump and the variations observed in transmission can only be attributed to TPA. Therefore, the variation of transmission originates from the angle dependence of TPA (through a coefficient β given below). *Hutchings* and *Wherrett*[118-121] theory of TPA show that β strongly depends on the relative orientation of the light polarization with the crystal axes. In the case of a linear polarization contained in the <110> plan, the orientation dependence of TPA is given by:

$$\beta(\theta) \propto \left[1 - \frac{\sigma}{2} f(\theta)\right], \tag{2.10}$$

where β is the anisotropy parameter of TPA.

Finally, the azimuthal dependence of the THz emission, SHG and the transmission intensity is determined by the same function $f(\theta)$. This function reproduces exactly the experimental variations.

We note that easy crystal axis determination is highly desirable when developing ultra-fast THz spectroscopy experiments based on optical rectification and free-space electro-optical sampling. In this case, as already pointed out, several parameters need to be properly adjusted simultaneously: crystals orientation, pump focusing, time delay, spot overlap. The measured intensity depends on the angle φ between the THz electric field and the z axis:

$$I_{signal} \propto E_{THz}\sqrt{1+3\sin^2\varphi}\,, \tag{2.11}$$

So, the maximum sensitivity is reached when the [-110] axis is parallel to THz field. In this context, Fig. 2.13 also shows that measuring the angle-dependence of the transmission is the simplest method for determining the best crystal orientation for optimum THz generation.

For a THz-TDS system, a convex lens is generally used to collimate laser beam on the crystal to increase the energy density for higher THz emission power below the damaged threshold. However, we have previously shown that SHG and TPA play a significant role when the crystal is placed at the laser beam waist. When the crystal is placed out of focus (e.g. z = 8mm), the intensity have a quadratic behaviour with the exiting power, which corresponds to the expected variation. Nevertheless, when the beam is focused on the crystal (z = 0), the THz emission tends to saturate what clearly shows that the other nonlinear processes affect the optical rectification.

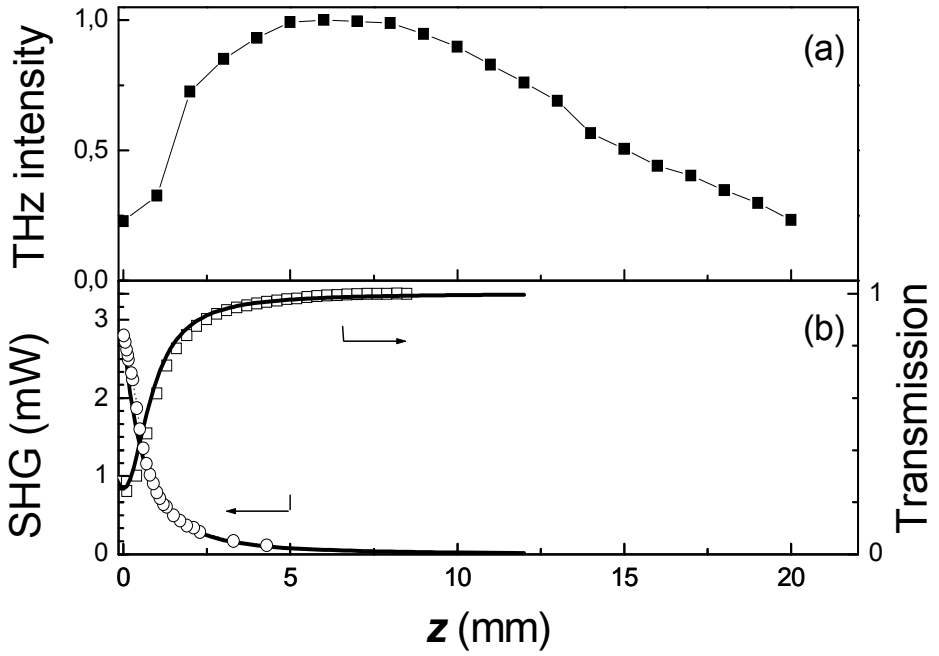

Fig. 2.14 (a) THz intensity as a function of the distance to focus point (open aperture z-scan). Pump power 300 mW. (b) Circles: SHG power. Squares: transmission at 800 nm. Solid line, right axis: fit of the TPA equation (nonlinear absorption coefficient β = 4.6 cm/GW). Solid line, left axis: fit of the SHG.

Competition between the nonlinearities was investigated using an open-aperture z-scan method [120~123]. The THz emission, SHG and transmission at 800 nm where measured as a function of the distance z between the beam waist and the crystal, along the optical axis with an azimuthal angle corresponding to a maximum of THz emission (see Fig. 2.13).

As shown in Fig. 2.14 (b), the SHG power is a decreasing function of z: the maximum is obtained at the focus point. The electric field associated with the SHG is given by $dE_{SHG}/dz \propto E_0^2$ with E_0. The integration or this equation leads to the z-dependence of the 400nm emission power:

$$P_{SHG} = I_{SHG} \times S(z) \propto \ell^2 P_0^2 S(z)^{-1}, \tag{2.12}$$

where l is the crystal thickness, P_0 the pump power and $S(z)$ the spot surface (Gaussian beam). The SHG power is thus inversely proportional to z^2 (see fit in Fig. 2.13 (b)).

The Fig. 2.14 (b) also shows the transmission at 800nm as a function of the distance to focus. TPA is responsible for the depletion of the optical pump intensity following $dI/dz = -\beta I^2$, where β is the nonlinear absorption coefficient (the linear absorption is neglected). The integration of this equation leads to the z-dependence of the transmitted power:

$$P_t = I \times S(z) = \frac{P_0}{1 + \beta P_0 S(z)^{-1} \ell}, \tag{2.13}$$

Fig. 2.14 (b) shows a fit (solid line) of the transmission data giving a nonlinear absorption coefficient β = 4.6 cm/GW due to TPA, in good agreement with previous studies [120~123]. As shown in Fig. 2.14 (a), upon focusing, the THz emission first increases. For z < 10 mm, the THz emission tends to saturate. For even smaller distances, the THz emission drops significantly, forming a 'z-hole', as already reported. As a consequence, it is now well accepted that the optimum THz generation is obtained when the crystal is placed slightly out of focus. We note that, as shown by *Dakovski et al*. [122], this z-hole does not depend on the THz wavelength (so the fact that the emission is here spectrally integrated does not play a significant role in the present analysis).

As observed experimentally and depicted in Fig. 2.14 (a) and (b), we can assume that the OR is not in competition with the other nonlinear process for z > 5mm. In this context, lets discuss the THz emission z-dependence induced by diffraction effects. When z is large compared to the pump beam Rayleigh length, the spot surface S is proportional to z^2. As already pointed out, since optical rectification is a second-order nonlinear process, the nonlinear polarization is proportional to the optical intensity $I_0 = P_0 / S(z)$ [118,122]. When diffraction effects can be neglected (spot size larger than the typical THz wavelength, 300 μm, the THz power is :

$$P_{THz} \propto S(z)(P_0 / S(z))^2 \propto z^{-2}, \tag{2.14}$$

as observed experimentally (in Fig. 2.14, and depicted schematically in Fig. 2.15). On the contrary, when the pump size is smaller than the THz wavelength, the THz emissions from the whole emitter section interfere constructively and the THz emitted power reads:

$$P_{THz} \propto (S(P_0 / S))^2 \propto z^0, \tag{2.15}$$

and the THz power becomes independent of the spot size close to focus. This is sketched by the solid horizontal line in Fig. 2.15

Now, let us discuss the z-hole observed in the THz emission when the beam is focused. First, as shown above, TPA is responsible for the depletion of the pump beam and, in the diffraction limit, this leads to a THz power:

$$P_{THz} \propto \frac{P_0^2}{(1+\beta P_0 S(z)^{-1} l)^2}, \tag{2.16}$$

which is partly responsible for the formation of a z-hole close at the focus. This is shown by the thick solid line in Fig. 2.14. Secondly, it is now that the THz radiation is partly absorbed by the free carriers [117]. They can be generated either by SHG or TPA in the ZnTe crystal. The free carrier generation rate by TPA is given by $\beta I_{800nm}^2 / 2\hbar\omega$, whereas the free carrier generation rate by SHG is $\alpha I_{400nm} / \hbar\omega$, where β is the absorption coefficient at 400 nm (33 cm^{-1})[123]. As a result, the TPA over SHG free carrier generation rate ratio is 0.35. In this context, the equation describing the THz generation has the form:

$$dE_{THz} / dz = aE_0^2 - \alpha_{THz} E_{THz}, \tag{2.17}$$

where the first term is due to optical rectification and the second to the free-carrier absorption. The THz electric field then varies as $E_{THz} = \eta \times aE_0^2 l$, where $\eta = (1 - e^{-\alpha_{THz} l}) / \alpha_{THz} l$ is a factor that reduces the THz field induced by optical rectification.

In order to estimate the free-carrier absorption of the THz radiation, we performed a two color experiment as depicted in Fig. 2.12: The ZnTe crystal is placed at z = 15 mm away from the focus, where optical rectification is not in competition with other nonlinearities. A BBO crystal is placed between the focusing lens and the ZnTe crystal. The THz radiation intensity generated by the 800 nm pump beam is measured when the blue-beam (400 nm) power is varied from 0 mW (I_{THz}^1) to 1 mW (I_{THz}^2) by adjusting the BBO azimuthal angle. This allows extracting a free-carrier absorption coefficient $\alpha_{THz}(z = 15\text{mm}) = l^{-1} \ln(I_{THz}^1 / I_{THz}^2) = 6\ cm^{-1}$. This two-color experiment allows estimating the effect of the free-carrier absorption on the THz radiation within experimental conditions as close as possible to what occurs when focusing the pump beam (i.e. when free carriers can be generated). In this case, hot free-carriers (electron and holes) are generated simultaneously with generation of the THz

radiation (i.e. zero time-delay), resulting in absorption of the THz radiation [117,124]. We assume that the absorption coefficient $\alpha_{THz}(z)$ is proportional to the free-carrier density and thus inversely proportional to the pump spot surface:

$$\alpha_{THz}(z) = \alpha_{THz}(z = 15\text{mm}) \frac{S(z = 15\text{mm})}{S(z)}, \tag{2.18}$$

One can estimate the z-dependence of the THz radiation power in the presence of FCA (bold line in Fig. 2.14). Nevertheless, when focusing, the pump surface becomes considerably smaller than the THz spot size. Thus, our calculation tends to overestimate the effect of FCA.

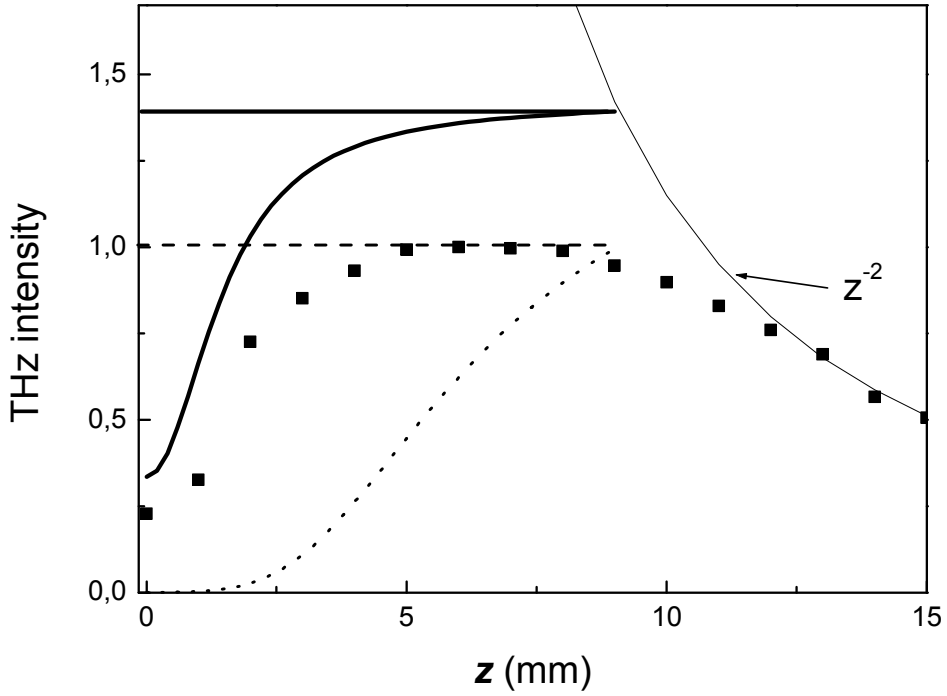

Fig. 2.15 Symbols: measured THz intensity. Thin solid line: expected THz emission z-dependence for large z, when the THz source is larger than the typical THz wavelength. Dashed: expected THz emission z-dependence in the diffraction limit (small excitation spot size). Thick solid line: THz emission z-dependence including TPA only. Dotted line: THz emission including only FCA generated by SHG. Dash-dotted line: THz emission including only FCA generated by TPA.

Finally, the Fig. 2.14 and 2.15 shown that both TPA and FCA strongly contribute to the reduction of the THz generation upon tight focusing. Even though pump depletion by TPA is

the main effect, we find that free-carrier absorption cannot be neglected and also gives rise to a THz 'z-hole' of the same order of magnitude.

2.4 THz - TDS with a Microstructured - Photoconductive Emitter

In Chapter 1, we reminded the principle, advantages and limitations of conventional photoconductive emitters. In particular, conventional photoconductive emitters need to be photo-excited on a small surface area as compared to the THz wavelength and, as a result, strong diffraction effects occur. Since the collection has a limited numerical aperture, small wavelength are lost (this can in principle be compensated by attaching an additional silicon lens on the antenna). Moreover, large bias voltages are needed (tens of Volts). Here, we present and characterize a new generation of *interdigitated* photoconductive emitters that allow solving these problems. The structure we study was fabricated in UCSB by Nathan Jukam, following the scheme recently proposed by *A. Dreyhaupt* and co-workers[33].

2.4.1 Structure of the emitter

The macroscopic image of our antenna chip is show in Fig. 2.16. The antenna array is based on a semi-insulating gallium arsenide (SI-GaAs) wafer (surface 5mm × 5mm and thickness 500μm). Each "chip" contains 7 individual interdigitated photoconductive antennas. The principle is the following: instead of a single antenna made of two electrodes, the interdigitated antennas are made of two structured interdigitated electrodes (see Fig. 2.6). The overall illuminated area is then large (500μm) even though the gap between the electrodes is small (allowing to apply small bias voltages). Since the structure is periodic, the voltage is alternatively positive and negative on successive electrodes. As a result, the emitted THz field is alternatively polarized (linearly) in opposite directions. As a consequence of the destructive interference in the far field, the total THz field is negligible. To overcome this problem, every other gap (between 2 electrodes) is masked during the fabrication. The fabrication requires two masks.

Each electrode is a layered structure with 20nm Titanium, 100nm gold, 10nm Platinum and 10nm Titanum. The width of each metal electrode is 1.5μm with its thickness 140nm. The gap-width between the electrodes is 1.5 μm, making the electrodes relatively easy to be driven using a relatively low bias field. Silicon dioxide SiO_2 was filled in the gap and also covered the electrodes as insulator. SiO_2 as good transparency and this thin film is only 0.75 μm.

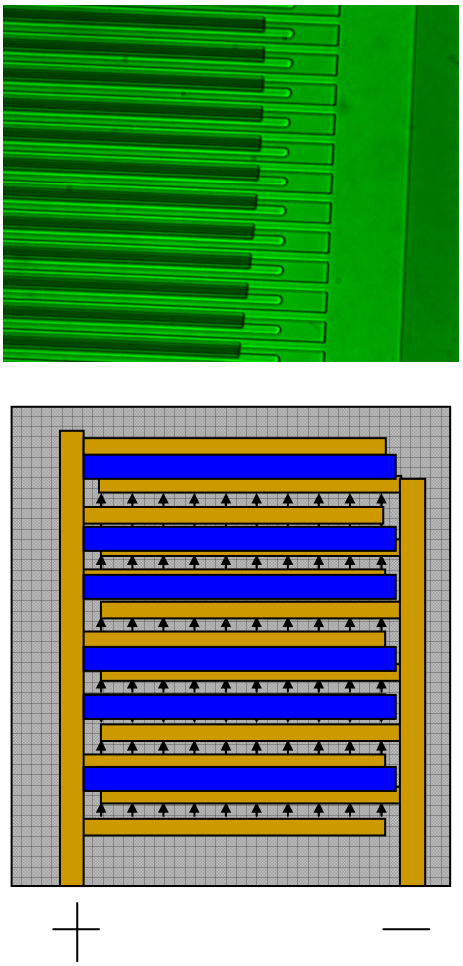

Fig. 2.16 (a) Image; (b) Diagram of interdigitated electrodes on SI-GaAs substrate

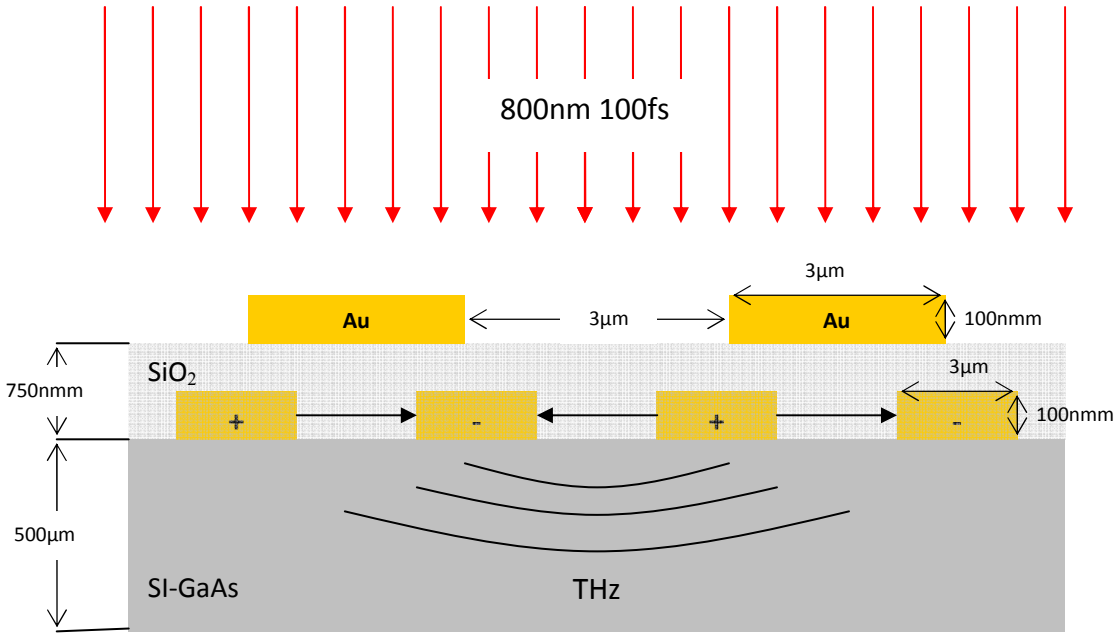

Fig. 2.17 Diagram of interdigitated SI-GaAs photoconductive antenna.

Au/Ti metal stripes were deposited on the SiO_2 layer. Fig.2.17 shows the cross-section of the antenna samples.

2.4.2 Characterization Experiment

We investigated the THz emission of these interdigitated emitters using a simplified THz-TDS geometry. The THz emitter is fixed inside a helium-cooled cryostat. The THz radiation was collimated with only 2 off-axis parabolic mirrors. In order to understand the carrier dynamics of the emitter, we used FSEOS to record the THz waveforms under various excitation conditions. The experimental setup is shown as follows:

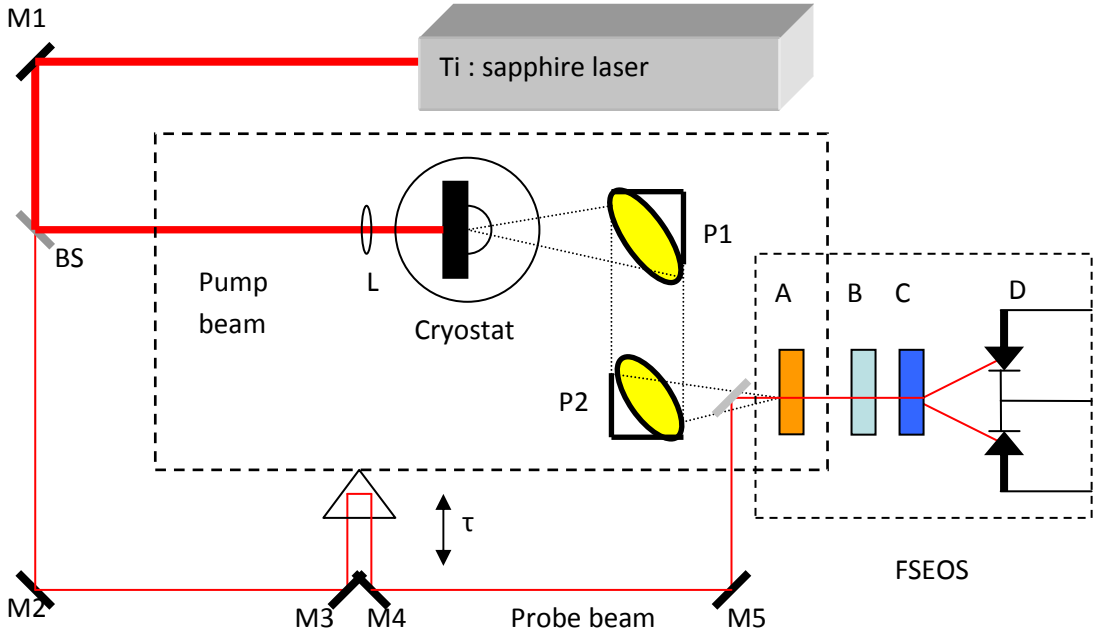

Fig. 2.18 Schematic diagram of THz-TDS; L: lens, M: mirror, BS: beamsplitter, P: off-axis parabolic mirror, τ: time delay, A: ZnTe sensor, B: λ/4 waveplate, C: Wollaston prism, D: balanced detector.

In this measurement, the incident power is 1.2W/ 800nm/ 100fs. The modulated duty cycle of the driving voltage is 5% in order to avoid heat-sink effects.

2.4.3 Results

Laser excitation when its energy larger than the GaAs bandgap creates free electrons and holes so that the electrical conductivity of the GaAs is transiently changed. Simultaneously, the semiconductor is driven with a bias field and the photo-generated carriers are accelerated resulting in a transient photo-current.

(a) Bias dependence of THz emission

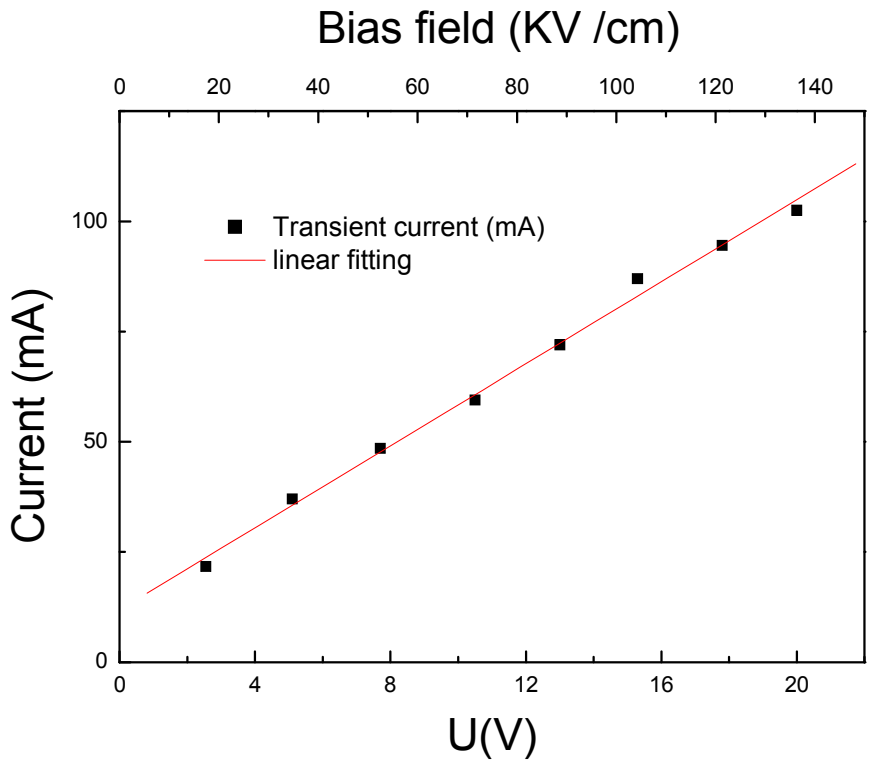

Fig. 2.19 I-V curve of photoconductive antenna

First, we report the I-V characterization of the structure in the Fig. 2.19. The current-voltage curve exhibits a linear dependence.

The THz emission performance also depends on the applied voltage. Fig. 2.20 shows the THz waveform for different bias field.

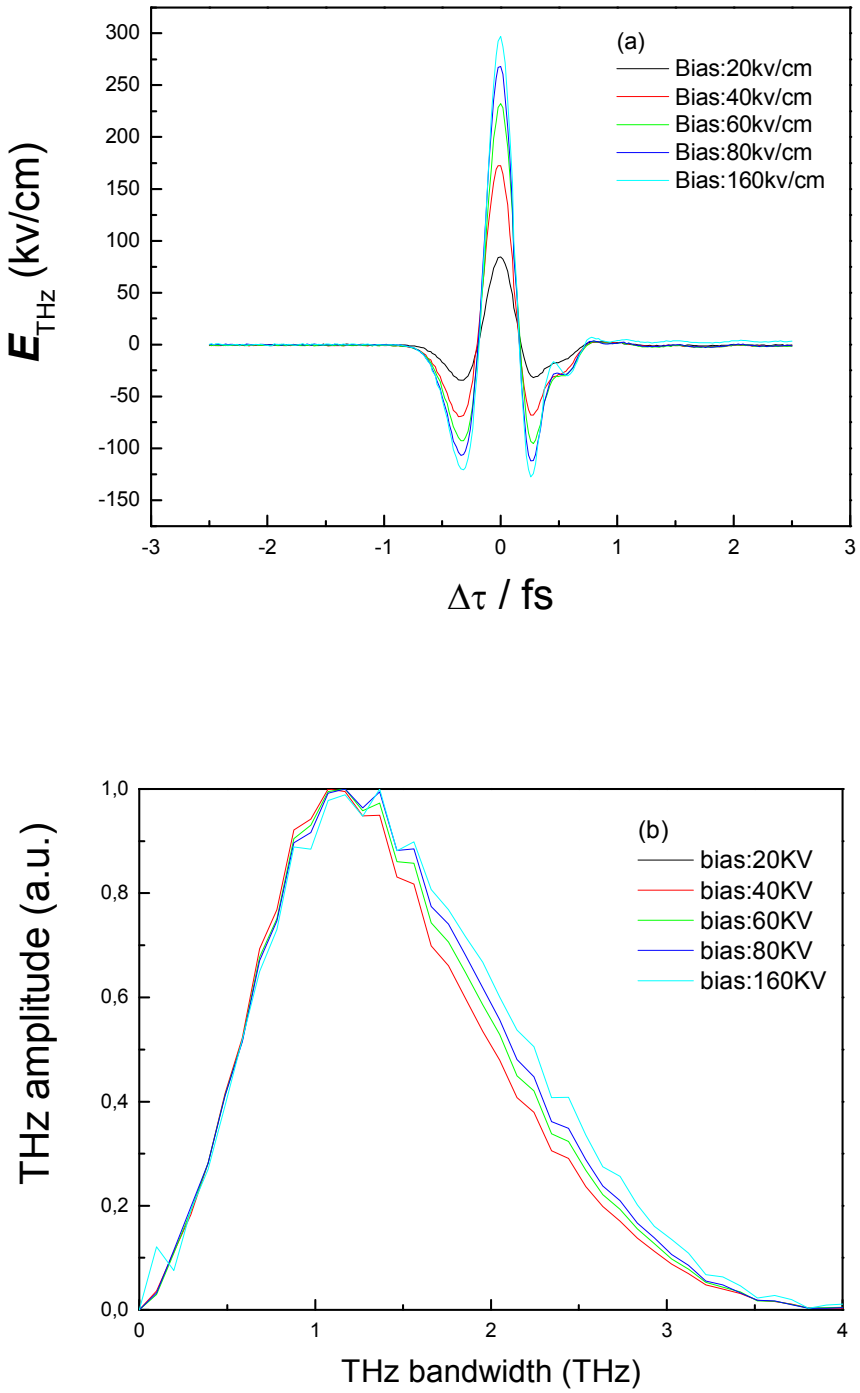

Fig 2.20 (a) THz waveform (b) THz Spectra of antenna at different bias field

The THz amplitude (peak to peak) increases with the bias field. The THz spectra obtained by FFT of the waveforms are shown in Fig. 2.20. The THz bandwidth is slightly expanded to higher frequencies. The analysis of these results goes beyond the scope of our work which was mostly limited to characterization. Nevertheless, one may attribute the observed

properties to *Γ-L* intervalley scattering which leads to the THz emission saturation[125]. In order to verify this hypothesis, the THz amplitude (peak to peak) versus bias field was measured and is shown in the Fig. 2.21. Fig.2.21 shows that the THz amplitude tends to saturates when the bias is beyond 80 kV/cm.

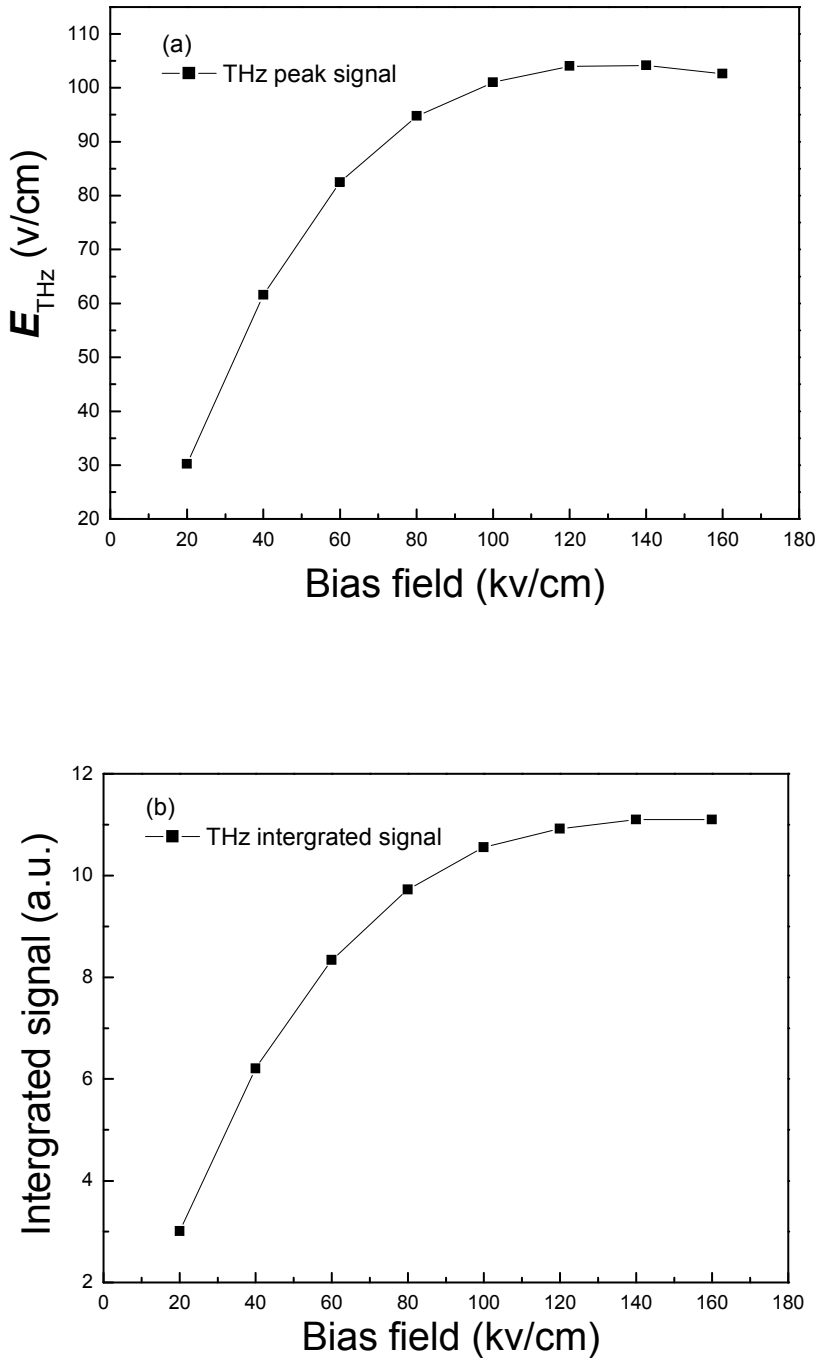

Fig. 2.21 Bias dependence of THz emission (a) Peak signal (b) integrated signal.

(b) Space Charge Screening

The transient current of the photoconductive antenna depends on the bias field and also on the carrier density that can be controlled with the excitation photon intensity. In the next experiment, the bias field was maintained at 10KV/cm and the incident pump power was adjusted with a neutral filter in the range 10mW, 50mW, 200mW and 600mW. Fig. 2.22 shows the THz waveform of the antenna for different pump powers.

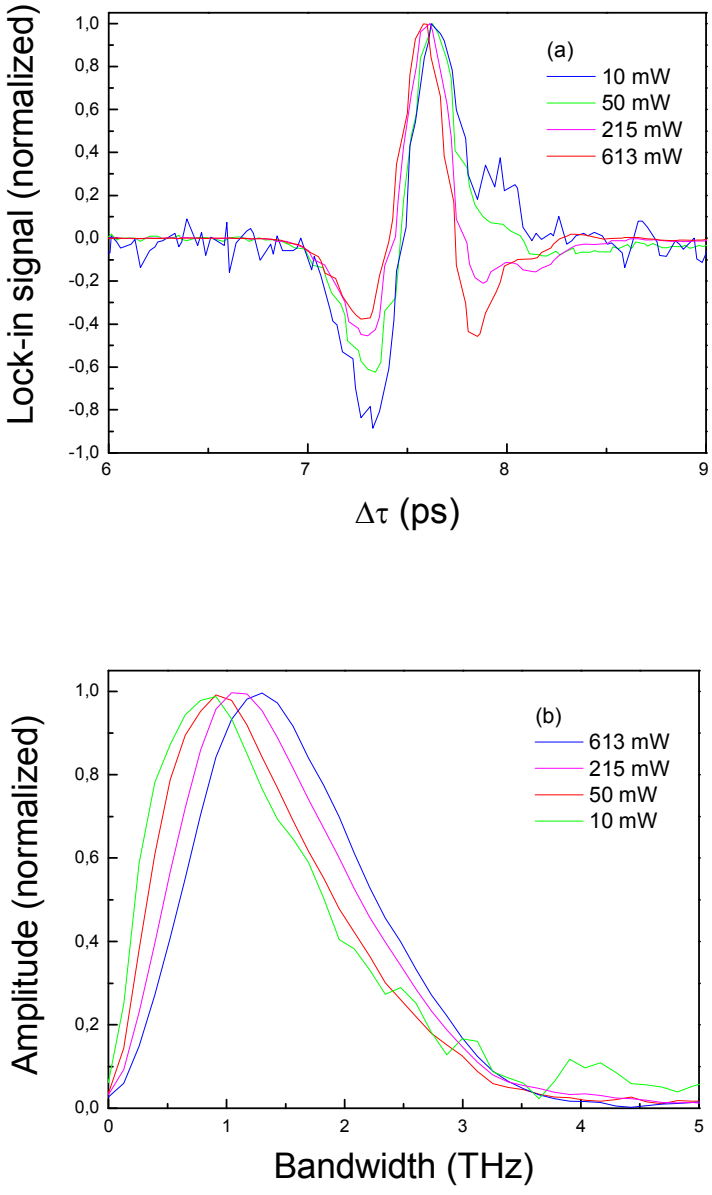

Fig. 2.22 The (A) THz waveform (B) THz spectra of antenna at different pump power

All the experimental data were normalized to the first main peak. When the optical flux increases, the tail valley appears and becomes deeper. The THz spectra show that the

bandwidth remains unchanged but the maximum frequency component of THz radiation is blue-shifted[127-129].

The high frequency components correspond to the appearance of a second lobe in the THz waveform. This corresponds to an oscillation of the charges in this ultrafast dynamic process. In the case of high flux excitation, the dense photo-generated carriers are accelerated by the bias field so that the electrons and holes form plasma. Meanwhile, the internal field causes the inverse acceleration of the carriers which screens the bias field as long as the carrier density is high enough. These two inversed field cause plasmon oscillation[126]. The oscillation frequency is:

$$\omega_p^2 = \frac{ne^2}{m^* \varepsilon}, \tag{2.19}$$

where the n carrier density, e unit charge, m* the effective mass, ε the dielectric constant. The plasmon oscillation frequency depends on the carriers density so that a high optical flux will lead to a THz blue-shift.

(c) Optimization of incident spot-size in emitter

In order to optimize the THz emission (the amplitude and bandwidth) for future experiments, we measured the emission as a function of the laser beam spot-size. First, we measured the (pump) laser beam spot-size with a knife-edge method (Fig. 2.23).

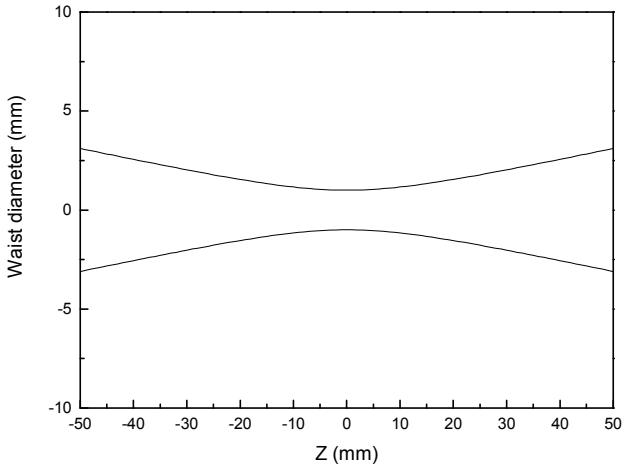

Fig. 2.23 Laser waist

The THz intensity and temporal shape are shown in the Fig. 2.24. Since the total pump power is constant, the optical flux increases when diminishing the excitation spot-size. This results in a blue-shift of the THz spectra, in accordance with the previous analysis.

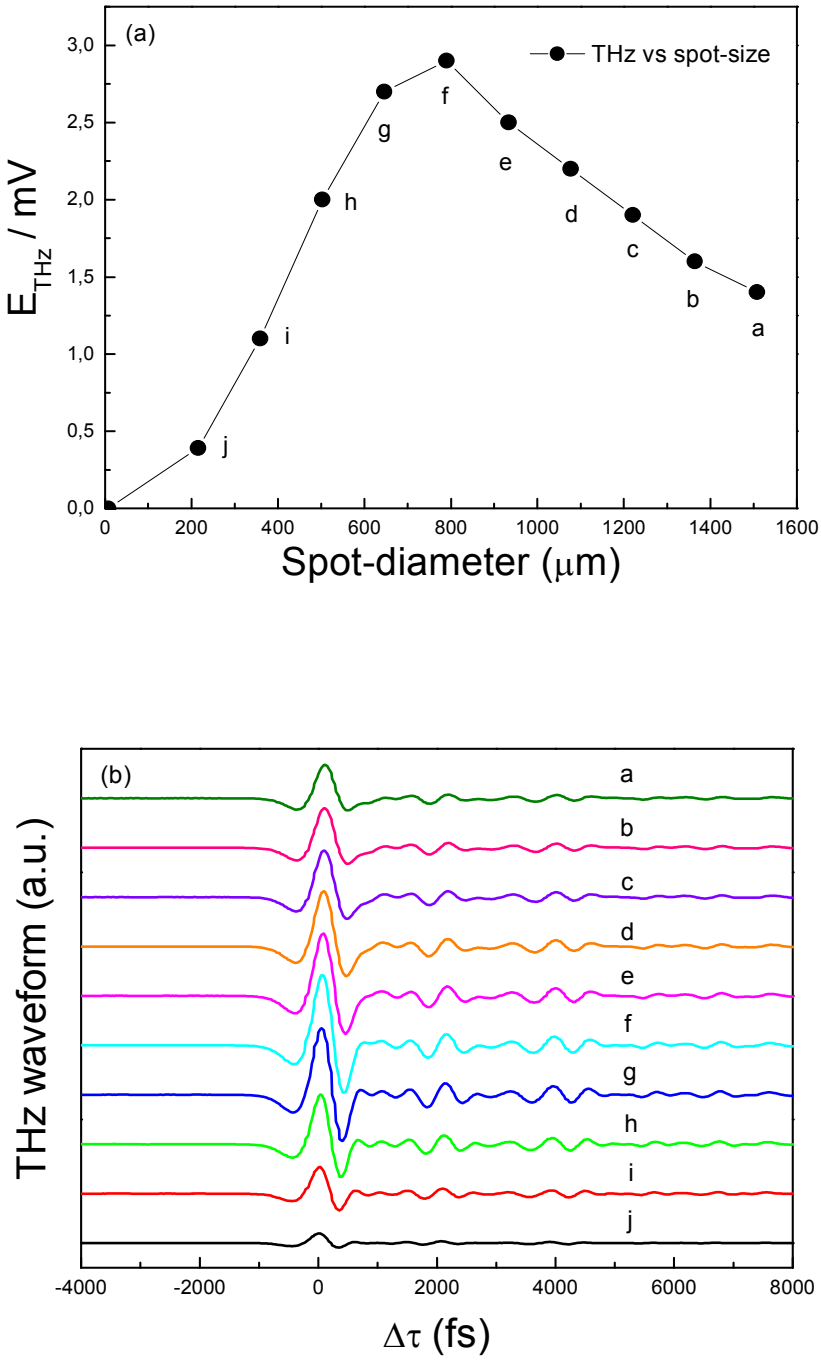

Fig. 2.24 (a) THz intensity vs spot-size; (b) THz waveform vs spot-size.

When the lens is far from the antenna, the spot-size becomes larger than the antenna active area, reducing the effective excitation power. The maximum emission efficiency is reached when the spot-size overlaps the whole antenna active region.

(d) Temperature dependence of emitter

Fig. 2.25 shows the temperature dependence THz emitter. Both the THz peak amplitude and THz integrated intensity were recorded.

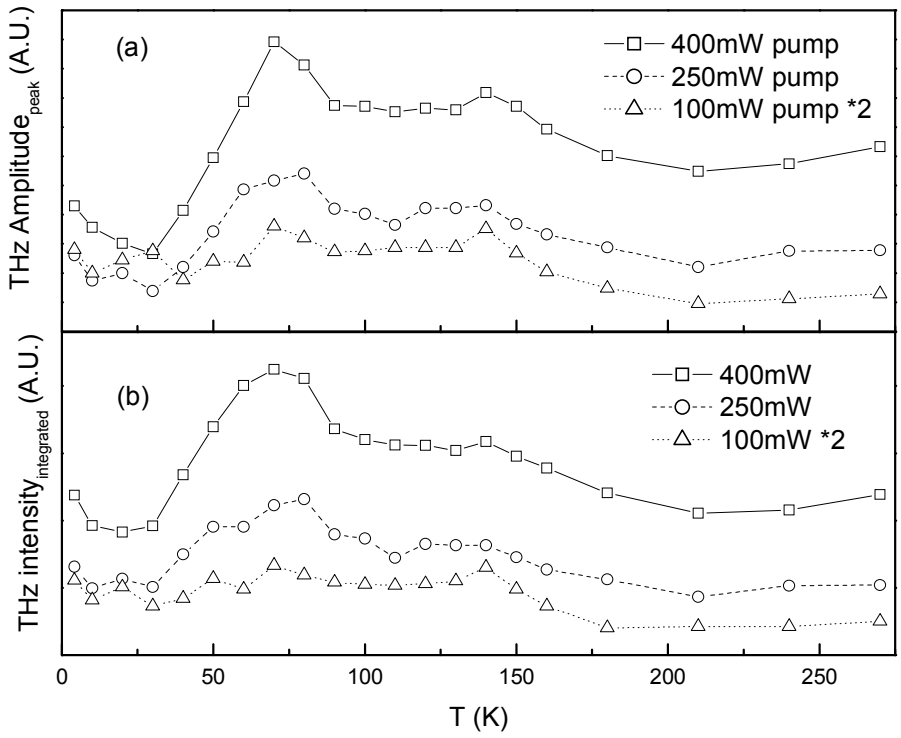

Fig. 2.25 Temperature dependence

In each measurement, the laser power was fixed to a constant value. The THz peak-to-peak amplitude decrease from 4.2k to about 25k then increase dramatically until it reaches the maximum at 70k. Then, the THz peak-to-peak amplitude decreases gradually until a secondary maximum at about 140k. Afterwards, the THz peak-to-peak amplitude decreases constantly. In order to confirm this observations, we also integrated the THz emission in the full the bandwidth 0-4THz. The temperature dependence of the integrated signals matches well with that of the THz peak-to-peak amplitude (in the measurements presented here the

pulse was incident normal to the antenna substrate so that the THz emission was independent of surface depletion effects and difference frequency mixing due to the surface $\chi^{(2)}$ of GaAs). The terahertz emission depends on the photoconductivity through:

$$E_{THz} \propto e\mu E_B \frac{d}{dt} n(t), \tag{2.20}$$

The Drude-Lorentz model describes the electron transport in a photoconductive process. The mobility μ depends on the temperature following a power law. *Stillman et.al*. [130] show that acoustic mode scattering is the dominating scattering mechanism below 70K, while impurity scattering dominates above 70K in N-type GaAs. Nevertheless, in Fig. 2.25, the intensity dependence from 4K to 30K does not fit with the Stillman's theory. In SI-GaAs substrate, the ion impurity density of SI-GaAs substrate is negligible but neutral impurity cannot be neglected. And there is also a similar temperature dependence of the mobility due to neutral impurity scattering. Hence, we may conclude that the neutral impurity scattering dominates the mobility and THz emission properties below 70K.

The effective deformation potential of GaAs increases from 6.3eV/Å at 0K to 7.8eV/Å at 300K[131] and the deformation potential scattering dominates the temperature dependence of the THz emission over 70K.

Next, we report on the influence of the temperature and pump power on the THz temporal and spectral shapes. In Fig. 2.26, the THz emission waveform and spectra are reported versus temperature and pump power.

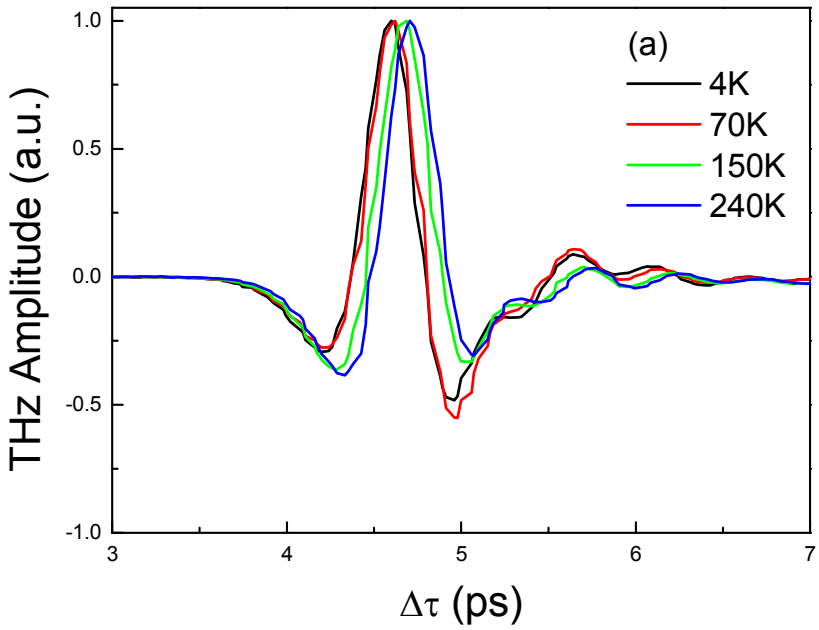
(a)
4K
70K
150K
240K
THz Amplitude (a.u.)
Δτ (ps)
1.0
0.5
0.0
-0.5
-1.0
3
4
5
6
7

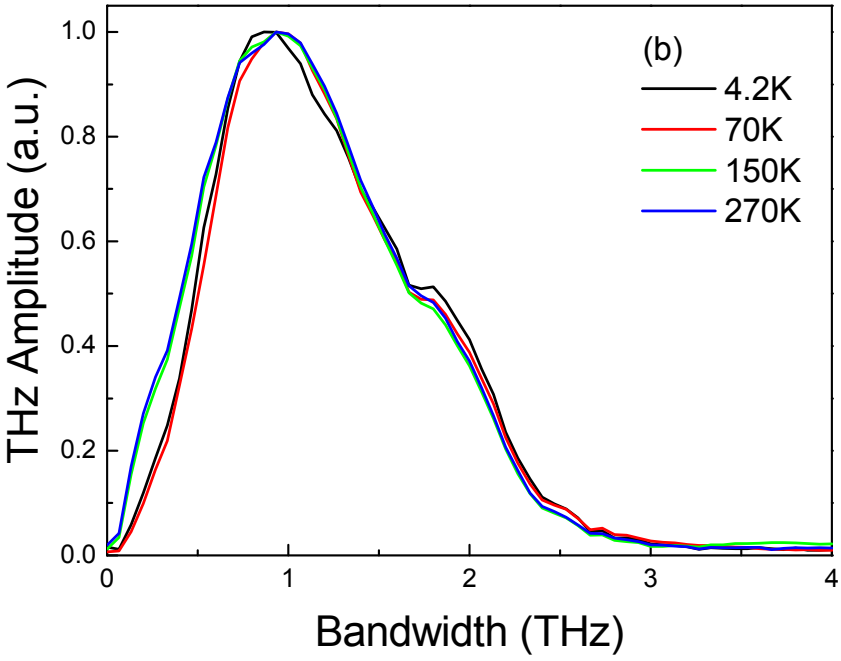
(b)
4.2K
70K
150K
270K
THz Amplitude (a.u.)
Bandwidth (THz)
1.0
0.8
0.6
0.4
0.2
0.0
0
1
2
3
4

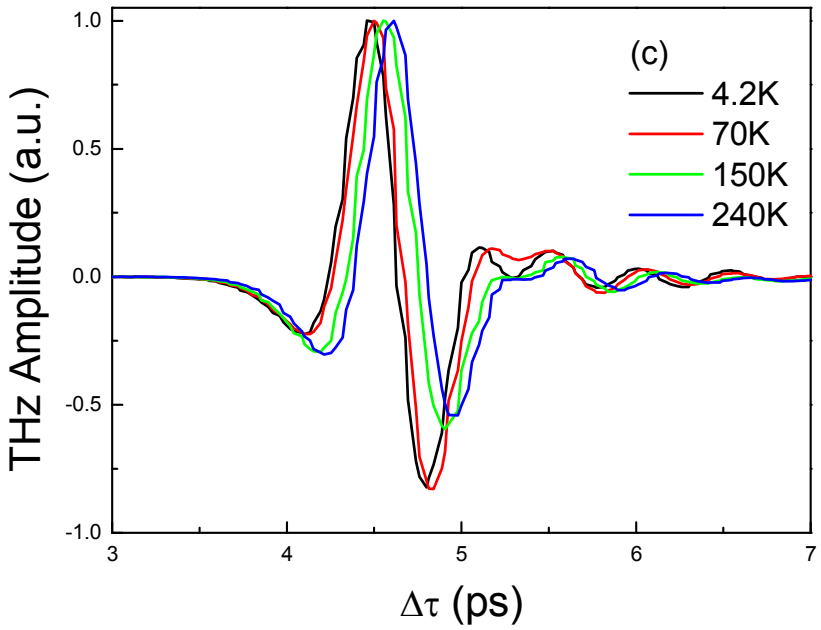
(c)
4.2K
70K
150K
240K
THz Amplitude (a.u.)
Δτ (ps)
1.0
0.5
0.0
-0.5
-1.0
3
4
5
6
7

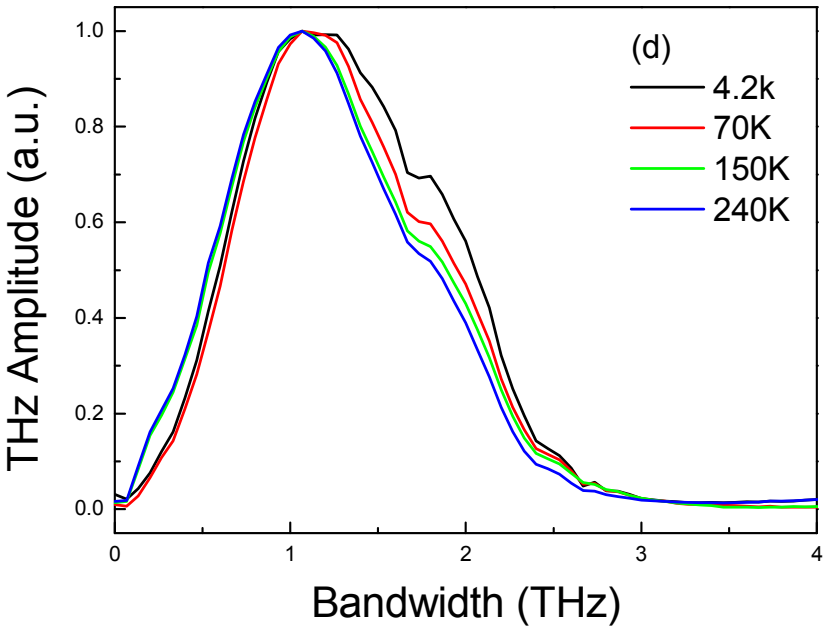
(d)
4.2k
70K
150K
240K
THz Amplitude (a.u.)
Bandwidth (THz)
1.0
0.8
0.6
0.4
0.2
0.0
0
1
2
3
4

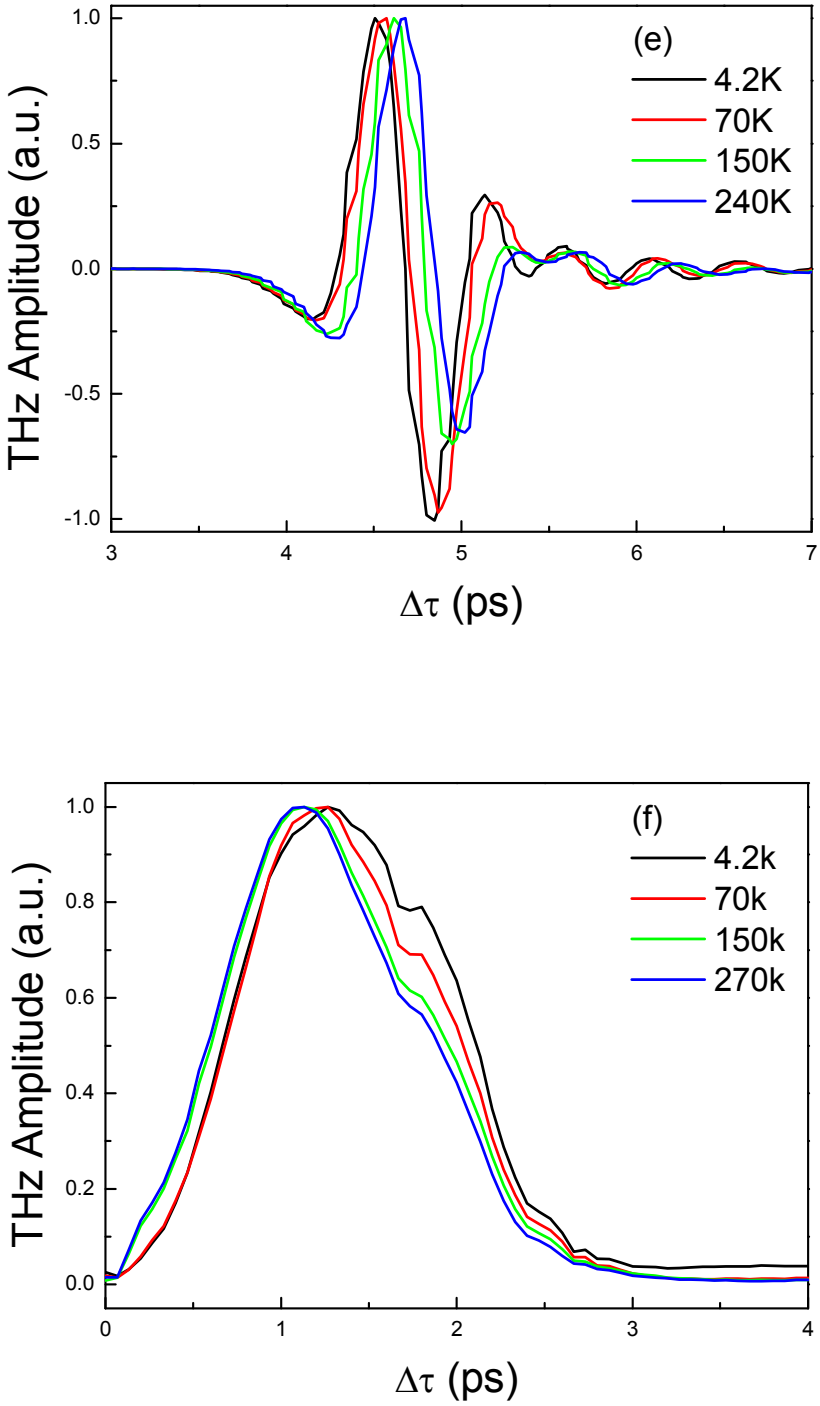

Fig. 2.26 THz waveform of antenna at different exciting power and different temperature: (a), (c), and (e) refers to the THz waveform at 100mW, 250mW and 400mW pump power; (b), (d), and (f) refers to the THz bandwidth at 100mW, 250mW and 400mW pump power; rectangular: 4.2K, circle: 70K, up-triangle: 150K, down-triangle: 240K.

As compared to the 100mW excitation power, the 200mW excitation power induces a larger negative lobe in the THz waveform (a a blue-shift of the spectrum), which indicates a larger effect of space charge screening in the latter case. In the case of 400mW exciting power, the negative lobe amplitudes of THz waveform are equal to the THz peak amplitude. Space charge screening induces an inversed movement of charges in the active region which causes the lobe of in the THz waveform.

2.5 Summary

Two different THz emitters were studied using THz-TDS: ZnTe crystal (optical rectification) and interdigitated photoconductive antennas.

The competition between optical rectification and other nonlinear optical process has been investigated. We find that both the two photon absorption and free carrier absorption reduce the THz emission.

For the interdigitated photoconductive antenna, the temperature and pump power dependence have been characterized.

Chapter 3

Application of THz-TDS: Gain Measurement in a 2.9 THz Quantum Cascade Laser

3.1 Introduction

Gain measurement is a major tool to investigate the interminiband transition dynamics of QCL [41]. Current challenges include further performance improvements and an understanding of the fundamental mechanisms. Therefore, it provides useful information such as the gain and losses of a QCL and allows feedback into new designs.

In this chapter, we expose gain measurements in a 2.9THz-QCL using THz-TDS. This provides useful information about gain and losses in QCLs, for operation below as well as above the lasing threshold. These measurements allow to provide a feedback into new QCL design.

3.2 Basic concepts of THz-QCL

Quantum cascade lasers (QCL) schematically consist of: active region, injection region and waveguide. The lasing behavior is based on the intersubband transition between quantized states in multiple semiconductor quantum well (QWs) structure based on GaAs/AlGaAs. The active region of a QCL consists in a superlattice. Electrons are injected electrically from an injector region into the second 'upper' miniband ('2'). From there, electrons can make a radiative transition to the top of the lower miniband ('1'). For a given set of materials, miniband and minigap widths can be engineered by suitable choice of the layer thicknesses. In order to obtain the long-wavelength lasing (hundreds of μm), the superlattice active region can be improved by gradually decreasing the well thickness in the direction of electrons motion, leading to the "bound-to continuum" structure [133,134].

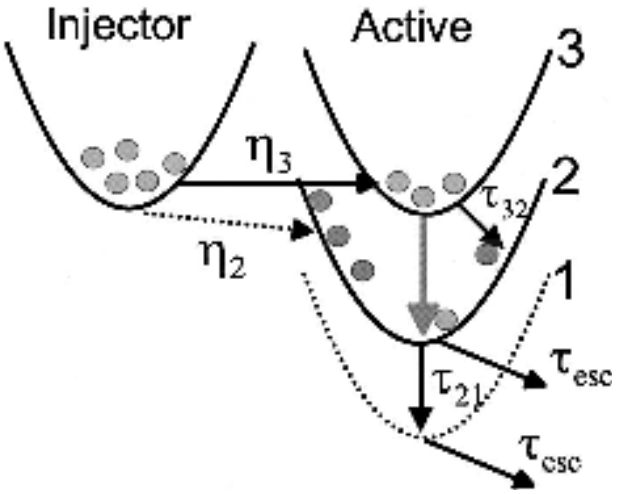

Fig. 3.1 Diagram of intersubband transition in an active region of QCL[133]

In this design, electrons are injected in an isolated state created inside a minigap by a thin well adjacent to the injection barrier, while electron extraction occurs through a lower miniband. Due to the diagonal nature of the laser transition, both injection efficiency and lifetime ratio (upper to lower state) are maximized, while miniband transport is employed as an efficient extraction mechanism to minimize the lower-state population. At zero bias, the states of QWs are localized because the variation in the adjacent layers is such that the corresponding energy levels of the isolated wells are out of resonant. As an electric field of appropriate value and polarity is applied, these states are brought into resonance so that they anti-cross forming manifolds of closely spaced extended states.

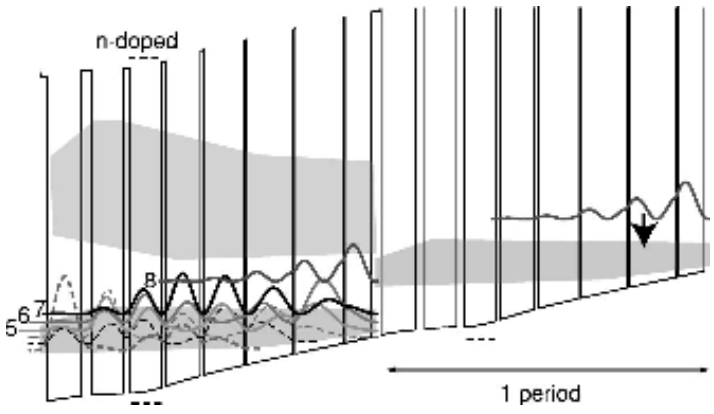

Fig. 3.2 Diagram of Bound-to-Continuum Interminiband Transition[134]

This situation is analogous to that of a compositionally graded semiconductor in which the corresponding conduction-band quasi-electric field associated with the bandgap grading is compensated by an applied electric field. Such a design is suitable for long-wavelength laser operation. The gain of THz QCL is dominated by the interminiband transition, which is

governed by the LO-photon scattering, and oscillator strength. The former governes the miniband lifetime and the latter reflects the optical transition matrix. Therefore, one can exact the gain coefficient by the following equation [135,136]:

$$g = \tau_2\left(1-\frac{\tau_1}{\tau_{21}}\right)\frac{4\pi e z_{21}^2}{\lambda_{\grave{a}}\varepsilon_0 n_{eff} L_p 2\gamma_{21}}, \tag{3.1}$$

where, g is the gain coefficient, τ is the lifetime, subscript number corresponds to the miniband, z is the optical transition matrix, λ is the center emission wavelength, γ is the full width at half maximum value of THz luminescence spectrum, ε_0 is the vaccum dielectric constant, e is the charge unit, n_{eff} is the effective refractive index, L_p is the one period of active and injector region.

However, there are three major loss mechanisms have influence on the lasing behavior of THz QCL:

The laser oscillator is formed by semi-transparent mirrors, typically un-coated, as-cleaved, and parallel semiconductor facets. They provide a reflectivity of $R=((n_{eff}-1)/(n_{eff}+1))^2$ each. This results in a mirror or outcoupling loss $\alpha_m = (1/L)\sqrt{\ln(R)}$, with L being the length of the resonator. The potential absorption loss is at resonant interminiband transitions. The extrinsic electrons in the injector region can cause significant absorption if there are optical transitions resonant with laser wavelength. The free carrier absorption in the semiconductor region and metallic contact layers induces the waveguide losses. The metallic layer influence can be suppressed by careful design of the waveguide.

The design of optical confinement structure is a key parameter for THz QCLs [137-141].

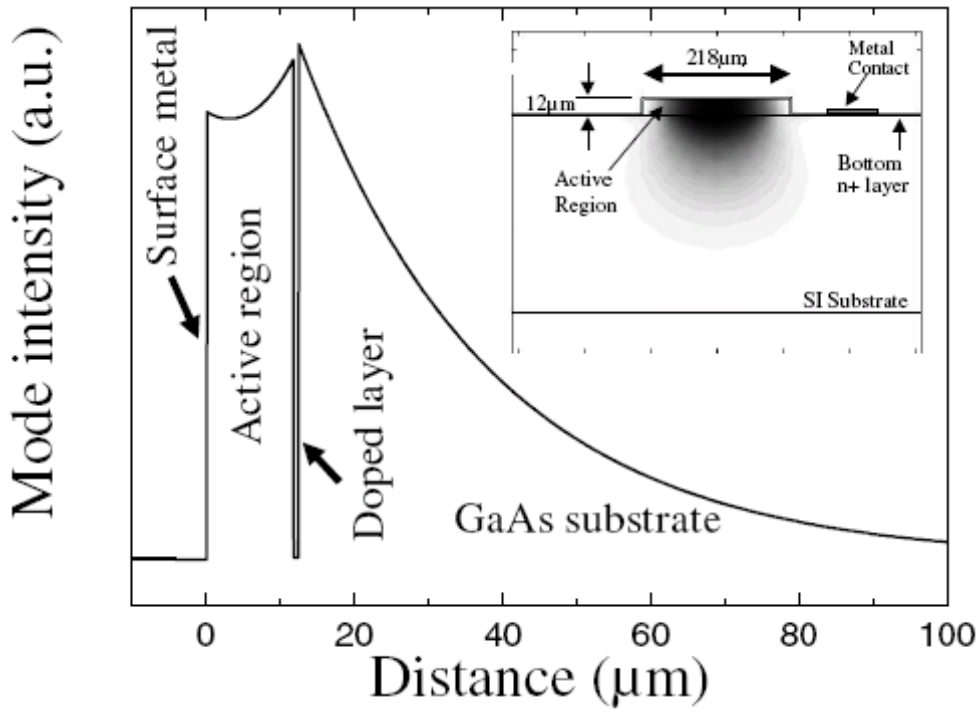

Fig. 3.3 Diagram of THz mode Confined by Surface Plasmon Waveguide

The free carriers absorption coefficient increases up with the radiation wavelength in conventional dielectric waveguide such as Fabry-Pérot structure and Distributed Bragger Feedback structure.

The laser threshold gain is given by:

$$g_{th} = \frac{\alpha_w + \alpha_m}{\Gamma} = \frac{\alpha_w}{\Gamma} + \frac{\ln(R)}{\Gamma L}, \tag{3.2}$$

Here, Γ is the confinement factor. The waveguide losses have an influence on the THz lasing emission. The surface plasmon confinement mechanism was successfully applied in the far-infrared wavelength range, in which the modes are not supported by a layered transparent medium but are electromagnetic surface waves (surface plasmons) at a metal-semiconductor interface. Surface plasmon guides tranverse-magnetic (TM) mode existing at the interface between two media which have dielectric constants of opposite signs, as it is the case with a metal and a semiconductor. For the THz radiation, the penetrating depth at corresponding wavelength is reduced dramatically.

3.3 Structure of 2.9THz quantum cascade laser

Our THz QCL consists of 90 repeated periods of a GaAs/$Al_{0.15}Ga_{0.85}As$ heterostructure. The band diagram of one period of the active region is shown in Fig. 3.2, together with the moduli squared of the most relevant wave functions, under an applied electric field of 2.1KV/cm. The energy difference between the upper state of the laser transition, labelled 2, and the lower superlattice miniband is 11meV. The corresponding oscillator strength between the interminiband transition is f_{21}=11 and $f_{21'}$=4, where 1 and 1' are the two upper states of the lower miniband, respectively. In agreement with superlattice sum rules, the oscillator strength to the remaining states is negligible. It follows that the main radiative transition is between states 2 and states 1. Compared with the chirped superlattice design, the center of the upper and lower state wave functions are more spatially separated, with the lower state (1) wave function occupying mostly the fourth and fifth quantum wells away from the injection barriers [134]. The superlattice miniband is designed to be only 18meV wide and to extend over 125nm, slightly longer than other reported superlattice design [134,142,143]. With a given transition energy and miniband width, having a longer period leads to a lower required electric field for miniband alignment, which reduces Joule heating. Meanwhile, it allows for a reduction in the total number of periods, and therefore the operating voltage, without decreasing the confinement factor. However, one should remember that these advantages are at the expense of a lower gain coefficient since this is proportional to the inverse period length. A great deal of care was taken in the design to avoid reabsorption of the emitted radiation within the injector miniband as well as from state 2. To this end, it was ensured that all computed dipole matrix elements between states separated by the laser transition energy were negligible. The laser transiton energy (11meV) was also made substantially smaller than the energy difference (17.5meV) between the upper miniband, starting with subband 3, and state 2 [143]. In our 2.9 THz QCL sample, the active region is embedded between upper (80nm thick) and lower (700nm thick) GaAs layers which are doped at levels of $n = 5\times10^{18} cm^{-3}$ and $n = 2\times10^{18} cm^{-3}$, respectively. These layers, together with the 11.57μm thick active region, the semi-insulating substrate, and the top contact metallization, form a plasmon confinement waveguide [142]. At longer wavelength, the overlap with the surface plasmon mode decreases rapidly with increasing doping of the active region. For the reason, in the present case, the two 12.0 and 11.4nm thick quantum wells were doped at a level of $1.6\times10^{16} cm^{-3}$, yielding a computed overlap factor of 27% and waveguide losses of $10cm^{-1}$. Combined with the doped layer just below the active region a transversed magnetic (TM) mode as shown in Fig. 3.4 is generated.

The mode typical of our 2.9 THz QCL sample overlaps with active region by 20% and has a significant part of decay into the substrate. Our sample was grown by molecular-beam epitaxy (MBE) and wet-etched into ridge cavities 200μm wide and 12μm deep with standard lateral AuGeNi contacts made. A Pd/Ge (25nm/75nm) contact, coated with a Ti/Au layer (20/100nm), was made to the top layer and centered on the laser ridge. The substrate was then thinned to approximately 200μm to aid cleaving. The device was indium bonded to copper holders and mounted on the cold finger of a cryostat.

3.4 Characterization of the THz QCL

Increasing the applied bias will detune the alignment of miniband in the injector region, hence, the THz output will be diminished. One can interpret specific features in the voltage-current (V-I) curve as an indication of resonant tunnelling through the injection barrier, arising from the alignment of upper miniband and adjacent lower miniband. The I-V characteristic reflects the global transport properties.

3.4.1 Experiment

The THz QCL sample is mounted with a specially designed cold-finger in a helium-cooled cryostat. The laser sample was driven by a rectangular bias with 25% duty cycle at 25KHz frequency, which is modulated by a low frequency (25Hz) in order to comply with the pyroelectric detector response time. The current and voltage were record with an Agilent oscilloscope and THz light output was recorded with a pyroelectric detector connected into a Lock-in trigged at the modulation frequency. The voltage, current, and light output were simultaneously acquired in a computer. The experimental setup is shown in Fig. 3.4:

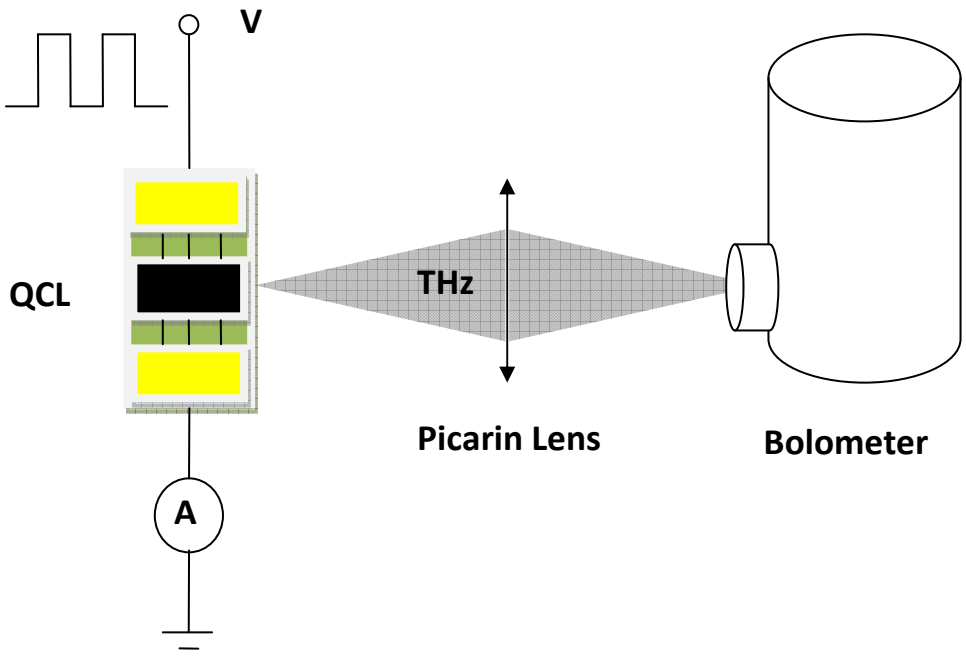

Fig. 3.4 Schematic setup of L-I curve and V-I curve measurement

Two parabolic mirrors were used to collimate the THz into the pyroelectric sensor. In our measurement procedure, the I-V curve and L-I curve were recorded with an oscilloscope simultaneously.

3.4.2 Result and analysis

Fig. 3.5 shows the I-V curve of 2.9THz QCL measured at the different temperature from 10K to 70K. In order to maintain the same current density, the applied voltage decreases with temperature. The electrical characteristics of the QCL can be reflected on the differential resistivity (ρ_d) deal by derivating the I-V curve.

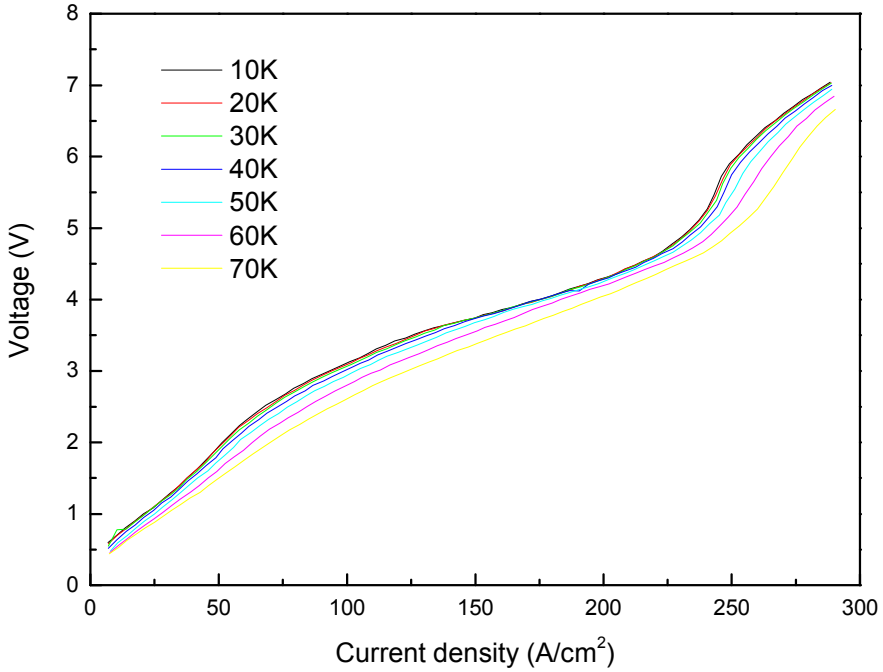

Fig. 3.5 I-V curve of 2.9THz QCL under different temperature

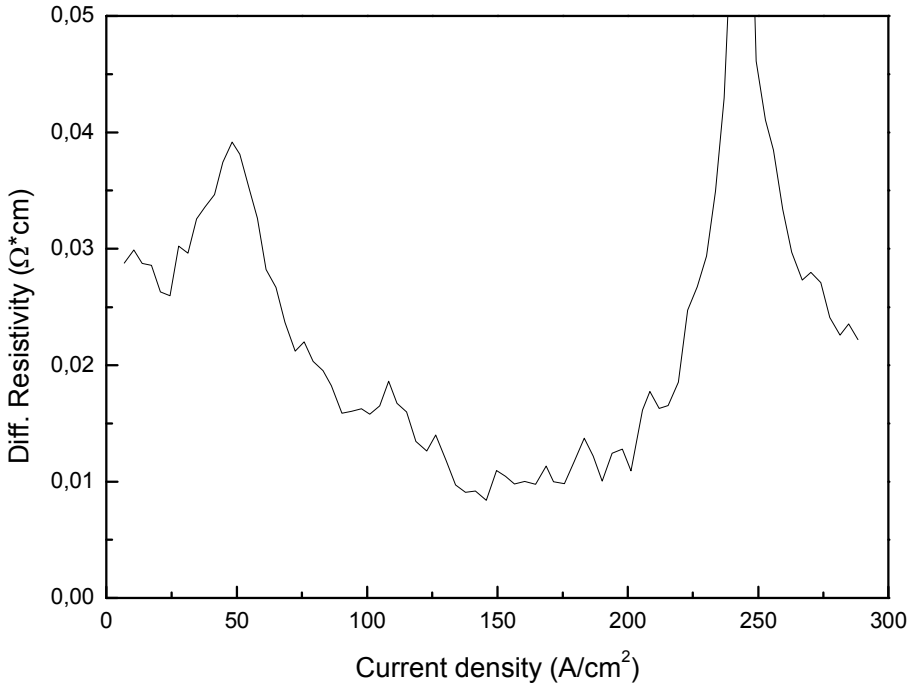

Fig. 3.6 The resistance of QCL at different injection current

In Fig. 3.6 the differential resistivity initially increase up to J~50A/cm^{-2}, corresponding a bias voltage of 1.8V. Below this voltage, transport is principally from electrons being scattered from the miniband of one period directly into the miniband of next period. Above this voltage value, electrons start to be injected into upper state, yielding a fast decrease in differential resistance. Population of the upper state of the THz laser transition began at 50A/cm^2. Although of rather low magnitude, this initial interminiband leakage current limits the minimum achievable threshold current density and should be further reduced. The THz output curves versus current at different temperature are show in Fig. 3.7

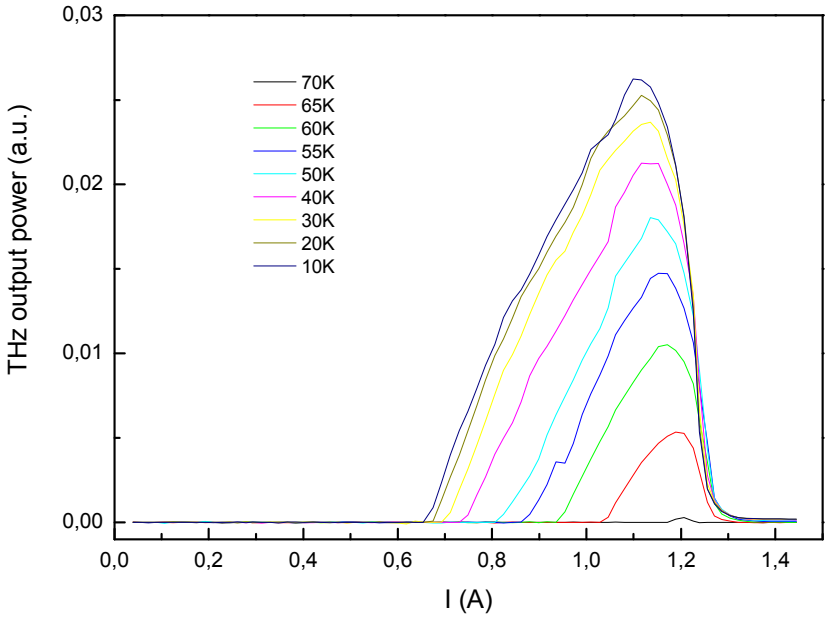

Fig. 3.7 the L-I curve of QCL at different temperature

The threshold current density at 10K is J_{th}=92A/cm^2 (injection current: 650mA) and it increases up to about 160A/cm^2 when the temperature reaches 50K. Raising further the temperature results in a more rapid increase of the threshold current up to 220mA/cm^2 at T=70K. The peak of the THz emission decreases with temperature. From the L-I curve and I-V curve at 10K, the threshold voltage is observed to be 3.6KV/cm. At approximately 3V, the end of resonant injection into the upper state of the laser transition produces a dramatic increase of the differential resistance, which limits the high current and high temperature operation of the QCL. An abrupt decrease of the differential resistance at J_{th} is visible at high temperature. In order to study the temperature dependence of the THz output and injection current, we calibrate the slope efficiency of QCL at different temperature. The slope

efficiency is defined as the derivative of the power to the current density. In our case, the L-I curve slope decreases only by 10% from 10K to 70K. Therefore, the weak temperature dependence of the slope efficiency means good injection efficiency and a small ratio of upper miniband lifetime τ_1 divided by interminiband transition lifetime τ_{21} [144]. In the L-I curve, above 50K, J_{th} increase very rapidly with temperature and lasing stops at 70K. During the lasing behaviour, after the abrupt decrease in differential resistivity ρ_d at threshold (110A/cm2), ρ_d increase steadily. This is not a consequence of a reduction of the injection efficiency. Consistent with the minimum ρ_d observed and the saturation of L-I curve, we conclude that the increase of ρ_d for $J>J_{th}$ reflects an increase of the ratio τ_1/τ_{21}, and believe this is the result of a current-induced heating of the electrons [145].

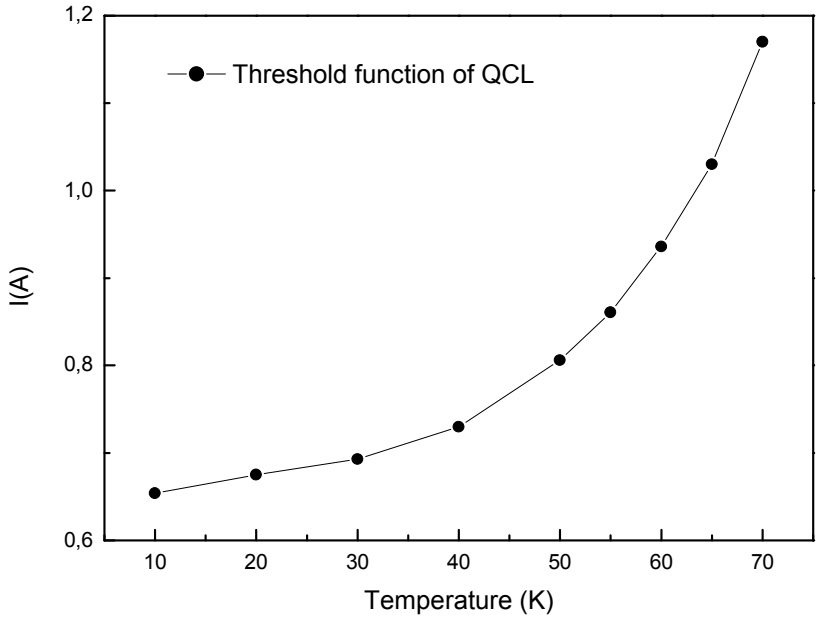

Fig. 3.8 The threshold of 2.9THz QCL at different temperature

At sufficiently low temperatures, scattering relies entirely on elastic processes, or on the emission of acoustic photons. Such mechanisms do not allow for a sufficient energy loss, and thus lead to the formation of a hot electrons gas. In turn, this can trigger activated intersubband LO-phonon emission from high-energy tail of the distribution [145-147]. In the present case, the net effect would be a reduction of τ_{21} rather than τ_1 owing to the smaller activation energy needed. Fast intersubband electron-electron scattering is the main mechanism responsible for the increase of electronic temperature [145,147,148]. This mechanism is more dominant at higher electrons density, yielding smaller τ_{21} at higher current, and

accounts for observed increase of with current density when $J>J_{th}$. However, the L-I curve and I-V curve can not reflect the THz gain of QCL. So, we use THz-TDS system to investigate the THz gain.

3.5 Gain measurement of THz QCL using THz-TDS

3.5.1 Observation of 2.9THz spectral amplification

The THz-TDS system with photoconductive antenna has described in the chapter 3. Here, we first attached the interdigitated antenna and THz-QCL together inside the cryostat with precise alignment in order to obtain a high coupling efficiency. The antenna chip was fixed tightly perpendicular with the waveguide of THz QCL so that the THz pulse divergence could be reduced into the minimum. In order to achieve the coupling, the antenna output surface is coupled with the QCL waveguide entrance with a special designed cold finger. Both devices were driven with different bias source at varied voltages. One of the shortcomings in this first experiment is that both the THz antenna and QCL output performance depends on the heat sink temperature. Therefore, one can only investigate the gain of QCL versus different injection current.

In our measurements, we first aligned the THz antenna signal and switch off the QCL driving source because the GaAs/AlGaAs heterostructure is transparent to the THz radiation. The Agilent signal generator was then set to drive the QCL at 25 KHz. This signal is also used as a reference signal triggering on the Lock-In so that the antenna THz output is not detected. The The corresponding signal is the reference signal are recorded for the gain calculation.

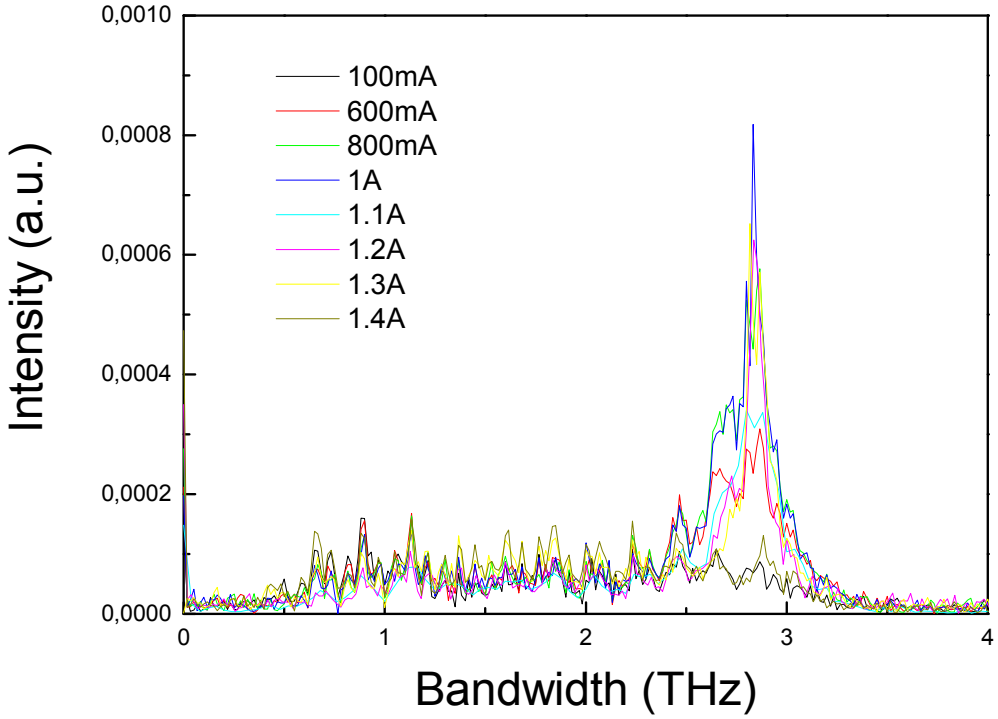

Fig. 3.9 THz amplification at different injection current

In Fig. 3.9, the THz emission spectra of QCL exhibit a narrow bandwidth with the central frequency 2.9THz. Clearly, the THz output intensity depends on the injection current density. Consistently with the L-I curve of the QCL, there is no visible THz transmission peak in spectra when the injection current does not reach the injection current density threshold. When the injection current increases to 110A/cm^2, the THz transmission emerges at the centre of 2.9 THz with a full maximum at half width of 200GHz. When the injection current density was increased to 250mA/cm^2, the THz linewidth became much narrower, about 110GHz. An increase of the injection current inside the QCL results in the dramatic increase of the THz output even though the input THz pulse power is constant. Therefore, the amplification is due to the interminiband transition of the QCL samples.

3.5.2 Gain measurement at different injection current

For the time domain measurements on the THz QCL, the antenna was modulated at 50kHz with a duty cycle of 50%. This signal was used to trigger the QCL, modulated at a frequency of 25kHz and with a 25% duty cycle. The latter was used for the lock-in reference frequency.

This method allowed the detection of the transmitted THz radiation that was modulated only by the QCL and eliminated any unaffected THz radiation bypassing the structure. This detection technique was necessary since the amplification of the input pulse is small at 2.9THz (The narrow bandwidth of the QCL gain overlapped only a small extremity of the antenna's bandwidth (see Fig. 3.10).

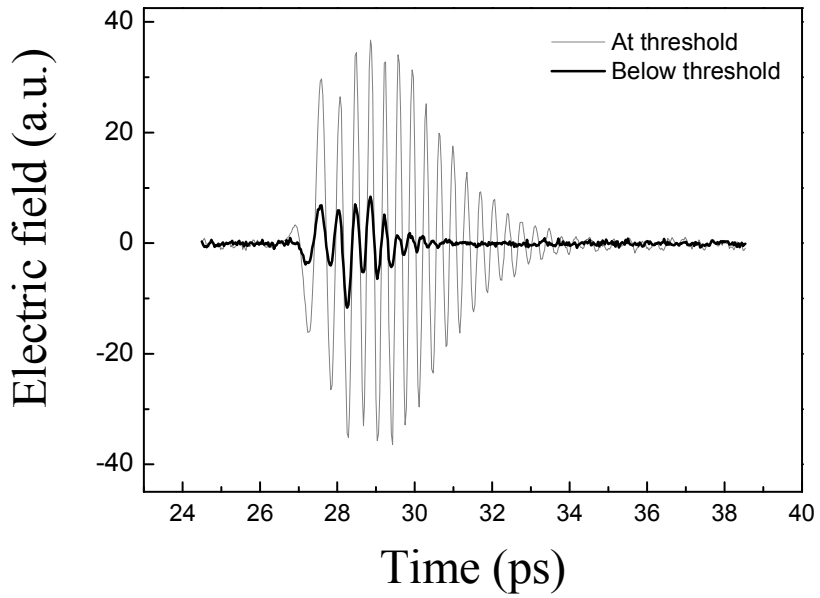

Fig. 3.10 THz waveform of amplificated signal transmitted through the 2.9 THz QCL

Fig. 3.10 shows the transmitted broadband THz pulse in time after it passes through the QCL cavity below and at laser threshold. For the former, a series of oscillations are observed that die out quickly indicating a broad spectral response. At the threshold current the field shows a very different response with oscillations lasting for approximately 7ps, corresponding to an amplification of the broadband pulse at the gain of the QCL. The spectra show a clear peak at 2.86THz i.e. at exactly the emission frequency of the THz QCL. There is also a considerable spectral intensity at lower frequencies due to the spectral response of the antenna which falls rapidly after 1.5THz.

We can write the output field at frequency ω from the QCL with the QCL on (biased) as

$$P_{\mathrm{THz}} = \mathrm{r_{in}}\,\mathrm{r_{out}} \exp\left(-\alpha \mathrm{L}/2 + \mathrm{i}\Delta \mathrm{K}_{\alpha}\mathrm{L}\right)\cdot\left(-\gamma \mathrm{L}/2 + \mathrm{i}\Delta \mathrm{K}_{\gamma}\mathrm{L}\right), \tag{3.3}$$

Here r_{in} , r_{out} are the input and output coupling constants. L is the length of the waveguide. α and ΔkαL are the loss and the loss induced phase of the waveguide (i.e. Drude losses from the doping). γ and ΔkγL are the gain and gain induced phase from the QCL structure. Similarly when the QCL is turned off (not biased) the output field R(ω) can be written as

$$R_{THz} = r_{in} r_{out} \exp\left(-\alpha L/2 + i\Delta K_{\alpha} L\right), \tag{3.4}$$

We wish to divide (3.3) by the phase term to express the gain in terms of R_{THz} and P_{THz}. The most obvious method is to measure the spectra with the QCL on to obtain (3.4) and the QCL off to obtain (3.4). However the frequency of the QCL is far away from the antenna's maximum spectral signal (shown in Fig. 1), and the narrow bandwidth of the QCL gain overlaps a small portion of the antenna's broad bandwidth. The change in signal to due to the QCL will be thus be small, and be on top of a large background signal. (In the time-domain $P_{THz} \sim R_{THz}$)

Instead we measure the difference between equations (3.4) and (3.5). To do this the QCL electrical pulses (which were locked in time and had the same duration as the antenna electrical pulses) were turned off for every other antenna pulse. The lock-in amplifier measured the amplitude (which we denote as S(t)) of the signal at the frequency at which the QCL pulses were turned on and off. (The QCL reference frequency is one half the antenna reference frequencies). At the QCL reference frequency the amplitude is the difference between the signal with the QCL turned on and the signal with the QCL turned off. Thus the measured signal S(t) can be written in the time-domain and frequency domains as

$$S(t) = \pm[R(t) - QCL(t)] \text{ and } S(\omega) = \pm[QCL(\omega) - R(\omega)] \quad , \tag{3.5}$$

We do not know a priori whether the measured amplitude S(t) corresponds to the difference R(t) – QCL(t), or QCL(t) –R(t). In order to resolve this ambiguity we must calculate the gain using both results and discard the results which are found to be unphysical. We can now reconstruct QCL(t) from the signal S(t), and the reference scan with the QCL off (i.e. R(t)). The complex gain can then be written as

$$\exp[-\gamma L/2 + i\Delta k\gamma L] = QCL(\omega)/R(\omega) = [R(\omega) \pm S(\omega)]/[R(\omega)] , \tag{3.6}$$

The real component of the gain γ can be found by taking the magnitude

$$\gamma = \frac{2}{L} \ln\left(\frac{|QCL(\omega)|}{|R(\omega)|}\right) \tag{3.7}$$

The phase change $\Delta k\gamma L$ caused by the gain can similarly be found by finding the phase of (3.8).

$$\Delta\varphi = \Delta k_{\gamma} L = \theta_{S(\omega)} - \theta_{R(\omega)} = \arctan\left(\frac{Im[S(\omega)]Re[R(\omega)]-Re[S(\omega)]Im[R(\omega)]}{Re[S(\omega)]Re[R(\omega)]+Im[S(\omega)]Im[R(\omega)]}\right), \tag{3.8}$$

where $\theta S(\omega)$ and $\theta R(\omega)$ are the phase of $S(\omega)$ and $R(\omega)$.

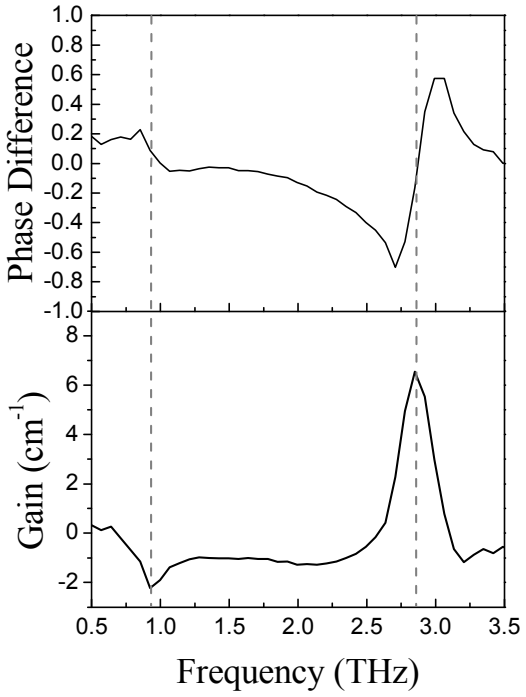

Fig. 3.11 Gain and phase of the 2.9THz QCL

From the transmitted signal, it is possible to determine the gain using a reference scan with the QCL off. We find the curves shown in Fig. 3.11 showing the gain and phase spectra with a QCL current of 954mA. We find a gain of 6.5 cm^{-1} at 2.86THz. The form of the phase, with the phase being negative before the centre frequency of 2.86THz, corresponds to the presence of gain. (An opposite behaviour, with the phase being positive before the centre frequency and negative at higher frequencies, would be expected in the case of absorption). This is a result of the phase being equivalent to the real part of the electric susceptibility, given by $\chi'(\nu) = 2\chi''(\nu)(\nu_0-\nu)/\Delta\nu$ (for a lorentzian resonance) where ν_0 is the centre frequency and $\Delta\nu$ is

the linewidth of the transition. $\chi''(\nu)$ is the imaginary susceptibility (which can be used to define the gain) and is negative for amplification and positive for absorption, resulting in the form observed in Fig. 3.11 [138].

When lasing, the absorption and reflection losses from the waveguide must equal the gain. Assuming a facet reflectivity of 0.37[139] resulting in mirror losses of 3.3cm^{-1} and a calculated free carrier absorption loss of α_g=8cm^{-1}, the gain of the laser is estimated to be 11.3 cm^{-1} which is significantly greater then the measured gain. The reason for this discrepancy could be the result of an underestimate of the scattering time in the Drude model, but is most likely due to the partial coupling of the THz pulses into higher order transverse modes of the sample [140].

Different transverse modes will have different number of nodes between the top metal contact of the laser and the bottom surface of the laser. (In contrast the different longitudinal modes will have a different number of nodes between the sides of the laser facet.) Lasing will only occur for the lowest order transverse mode (the plasmon mode shown in Fig. 3.3) since the spatial overlap of the mode with the active region is greater then any other transverse mode. For the signal scan the QCL is modulated, and the signal scan will only contain the amplification caused by the QCL. However for the reference the QCL is not modulated (it is off), and it will contain contributions from higher order transverse modes. These higher order transverse modes will artificially increase the reference scan. Thus, if the THz input pulse is coupled into the higher order transverse modes (which do not lasing) this will only be seen for the reference scan and not the signal, leading to an underestimation of the gain.

The small dip in Fig. 3.11 at 0.93THz (3.8mV) is possibly to do absorption from levels within the cascade miniband. In the phase spectrum, there appears to be an inversion of the phase at this point compared to the peak at 2.86THz that is consistent with absorption. This illustrates that the THz-TDS technique allows the simultaneous measurement of both the gain/loss and the phase information of a resonance. This is in contrast to other techniques such as FT-IR spectroscopy where only the intensity is recorded. The evolution of the field as a function of the QCL driving current was investigated at 10K.

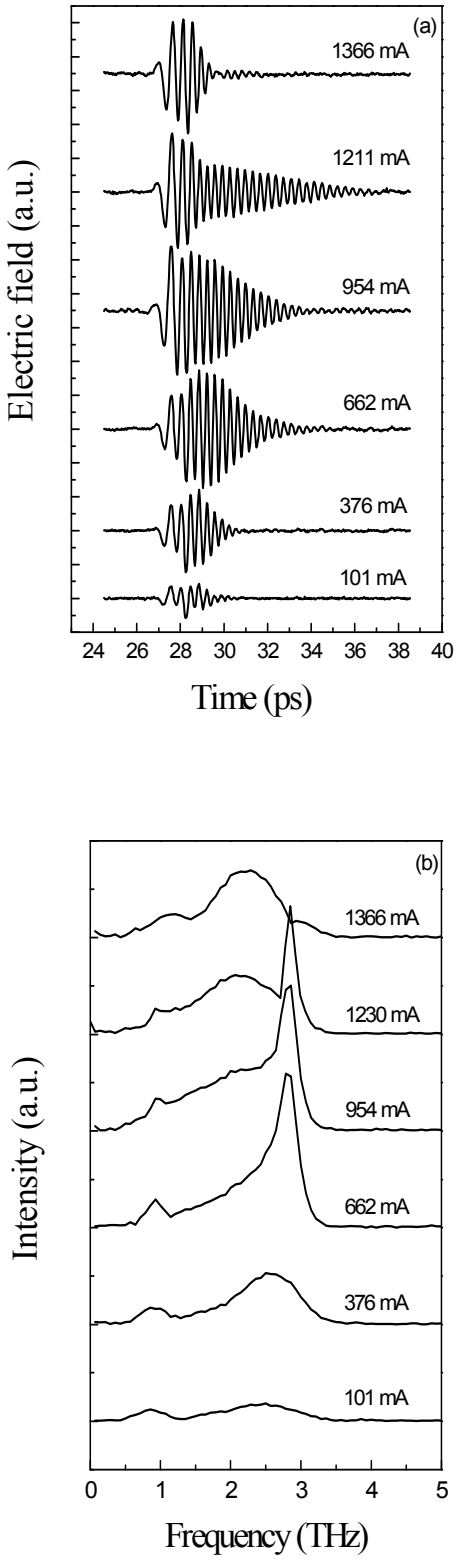

Fig. 3.12 (a) Amplified THz waveform at different injection current; (b) Amplified THz spectra at different injection current

Fig. 3.12(a) shows the fields for currents from 101mA to 1366mA i.e. from well below threshold to beyond the maximum operating current when laser action stops. Oscillations corresponding to emission at 2.86 THz are observed as early as 200mA, considerably below threshold. The oscillations become more intense and persist longer in time as the current is increased. The corresponding spectra are shown in Fig. 3.12b and we clearly observe an increase in emission at the frequency of the QCL and a narrowing of the spectra as threshold is approached due to the alignment of the bandstructure. At 1366mA, the emission at 2.86 THz disappears due to the misalignment of the cascade structure and hence an end to laser action. As mentioned previously, the feature at 0.93THz is possibly due to an absorption resonance within the QCL bandstructure. An interesting point of this THz-TDS technique is that we can examine the gain spectra of the QCL above threshold. Studies of electroluminescence spectra above threshold [149] are problematic as the signal is easily swamped by the laser emission. However, the THz-TDS measurement of the probe pulse does not detect the QCL laser emission. The phase of the QCL laser is not locked in time with the femtosecond laser pulses which measure the THz probe pulses. The femtosecond laser pulse's position in time relative to the QCL laser field will vary randomly time, and the detected signal from the QCL laser field will average to zero.

In Fig. 3.12 the gain is plotted as a function of injected current. Also shown for comparison are the I-V and I-L characteristics at 10K (Fig. 3.12(a)). Firstly the peak gain (Fig. 3.12(b)) increases with increasing current due to the presence of gain even if the losses prevent laser action. The peak gain, however, saturates at 662mA (i.e. just above laser threshold at 623mA), where the gain becomes 'clamped' at the value of the total optical losses. (This is due to the strong negative feedback of the laser intensity on the population inversion that results in gain saturation and stabilizes the carrier density at the threshold value) [138] This behaviour is typical of lasers and semiconductor optical amplifiers (SOA) [150-152] and reported previously for a quantum cascade laser. Furthermore, the gain appears to persist even after the laser action has ceased. At 1.21A, there is no further emission from the QCL. However, the input pulse continues to be amplified and it is only at 1.3A that no further amplification is seen. This is due to the fact that gain is still present although it has become smaller than the total optical losses, inhibiting laser emission.

3.5.3 Temperature Dependence of Gain

The temperature dependence of the transmitted pulse was also investigated. Fig. 3.13(a) shows the evolution of the electric field as a function of temperature, with the QCL biased at a constant voltage of 4.83V. Oscillations corresponding to emission at 2.86THz are observed up to 90K, although the amplitude decreases rapidly after 70K. The first field cycle, corresponding to broad spectral emission, also decreases with increasing temperature. These results are also observed in the spectral domain (Fig. 3.13(b)) where the intensity at 2.86THz decreases at high temperatures a result of gain reduction owing to leakage of the electrons into higher subbands and thermally activated LO phonon emission [24]. An interesting point is that gain is observed at 90K even though the laser action ceases at 70K. This hints that the temperature operation of the QCL can be extended with a reduction in the mirror and/or the waveguide losses.

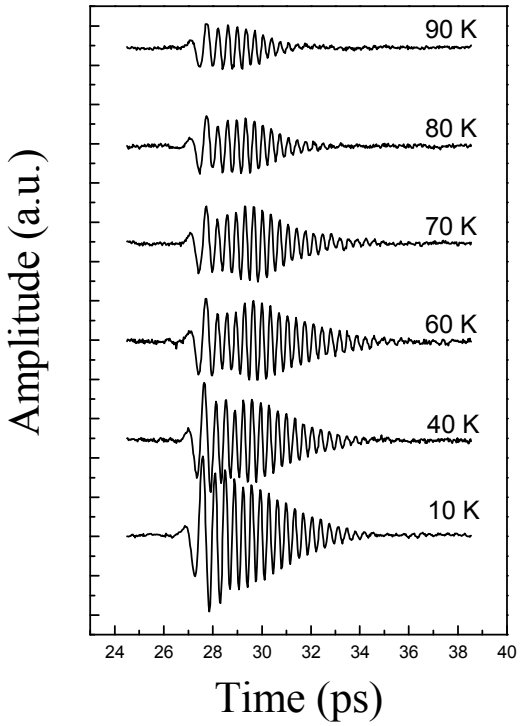

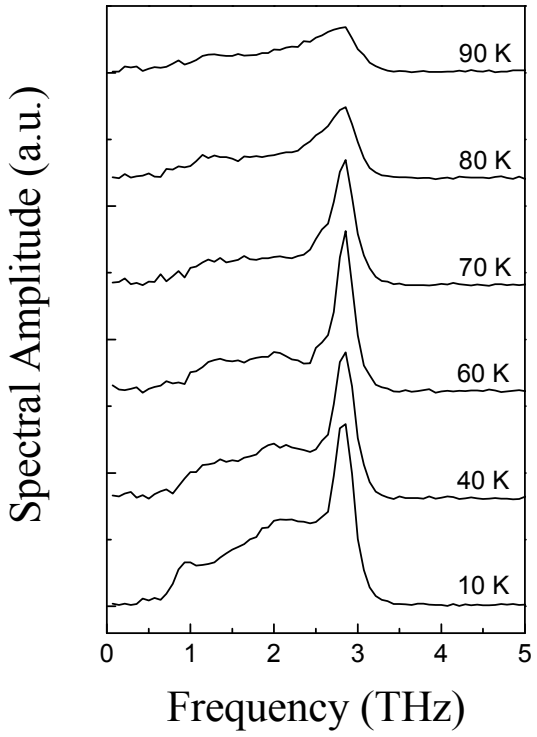

Fig. 3.13 (a) Amplified THz waveform at different temperature (b) Amplified THz spectra at different temperature

The temperature measurements above are summarised in Fig. 3.14 where the gain field is plotted against the driving current for temperatures from 10K to 90K. (The gain field is defined as the ratio of the transmitted electric field with the QCL on to that with the QCL off). As previously shown in Fig. 3.12, we again observe a large increase in gain with increasing current to just below threshold where it is clamped and which slowly drops off before the structure misaligns. As the temperature is increased, the gain rises slower, reaching the clamping point at higher currents. The position of the clamping current is slightly higher than the threshold current. Using this data we can plot the change in current at a fixed gain as a function of temperature. This is shown in the inset Fig. 3.14 for a gain highlighted by the grey dotted line showing a typical exponential rise with a T_0 of 23.9K, similar to that found considering the threshold current (Fig. 3.14).

3.6 Summary

The THz amplification of a 2.9THz QCL was investigated with THz-TDS. The THz gain was measured at different injection current and temperature. The evolution of the gain as a function of current was studied and we demonstrated the effect of gain clamping.

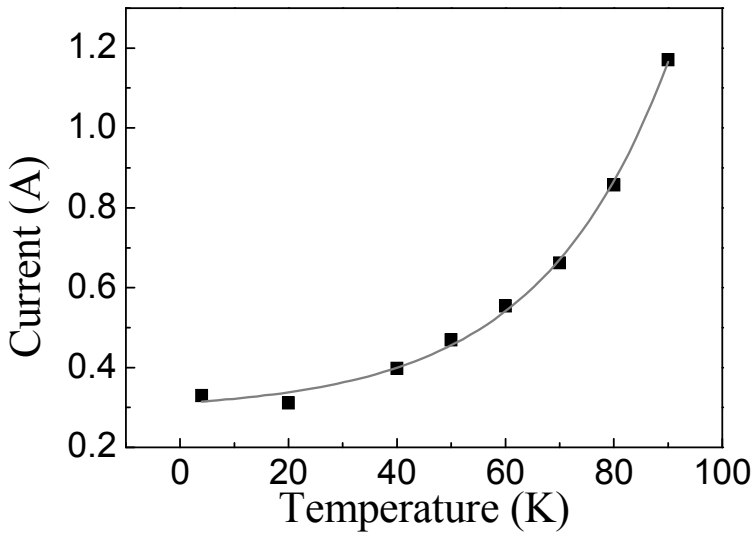

Fig. 3.14 Threshold current of 2.9THz QCL at different temperatuere

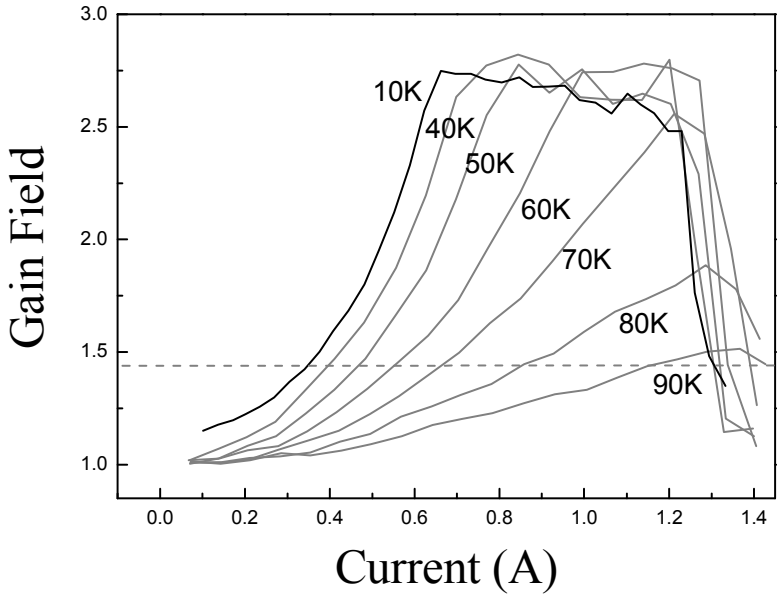

Fig. 3.15 Gain function of 2.9THz QCL at different temperature

Chapter 4

Optical Nonlinearities of AgCl nanocrystals doped niobic tellurite glass

4.1 Conception

4.1.1 3rd Order Optical Nonlinearitires

A currently active area of nonlinear optics is concerned with all-optical devices in which an optical beam is controlled or switched by another optical beam or itself rather than by an electrical control signal. Hence, the development of photonic materials will determine the future progress on photonic switching and information processing. The electric fields associated with intense optical beams are so large that higher-order nonlinear terms in the material polarization become significant. In the case of third-order optical nonlinearities, many different processes, such as third harmonic generation, four-wave mixing process, the optical Kerr effect and/or the intensity-dependent refractive index, are possible. , and which form the basis for the all-optical switching.

In the nonresonant case, the nonresonant optical nonlinearity arises from the distortion of the electron orbits about the nuclei under the influence of high-intensity optical field, which exhibits subpicosecond temporal responses with the minimum heating. In the resonant case, the large resonant nonlinearities are present, but the penalty is higher power dissipation and slower response, which depends on the relaxation time of carriers excited by optical field.

Nonlinear refractive index and two-photon absorption are the major contributions to the 3rd order nonlinear susceptibility. The refractive index described as a function of the electric field,

$$n^2 = \varepsilon = (1 + 4\pi\chi) = 1 + 4\pi(\chi^{(1)} + \chi^{(3)}E^2), \tag{4.1}$$

where the linear refractive index is independent of the electric field. So, the total refractive index can be written as,

$$n = n_0 + n_2 \left\langle E^2 \right\rangle = n_0 + n_2' \left| E^2 \right|, \tag{4.2}$$

Meanwhile, the nonlinear susceptibility follows as,

$$\chi^{(3)} = \mathrm{Re}\,\chi^{(3)} - i\,\mathrm{Im}\,\chi^{(3)}, \tag{4.3}$$

The nonlinear absorption corresponds to the imaginary part of the abovementioned equation, which is generally expressed with β,

$$\beta = (32\pi^2\omega/c^2 n_0^2)\,\mathrm{Im}\,\chi^{(3)}, \tag{4.4}$$

In the femtosecond region, the transient polarization of delocalized electrons is the only root of high order nonlinear susceptibility.

A Fig. of merit is helpful in the competitive materials for all-optical devices, and the Fig. of merit can be expressed as,

$$F \approx \frac{n_2}{\tau \cdot \alpha}, \tag{4.5}$$

where τ is the response time, and α is linear absorption coefficient.

4.1.2 Tellurite Niobic Glass

TeO_2-based glass consists of TeO_{3+1} polyhedra, TeO_4 trigonal bipyramids (tbps) and TeO_3 trigonal pyramids (tps). As shown in Fig.4.1, TeO_4 is trigonal bipyramid (tbp) with two axial and two equatorial oxygen atoms and a lone pair, the TeO_{3+1} asymmetric polyhedron has a short Te–O axial bond and the other long Te–O axial bond, and the the TeO_3 trigonal pyramid (tp) has three short Te–O bond distances .

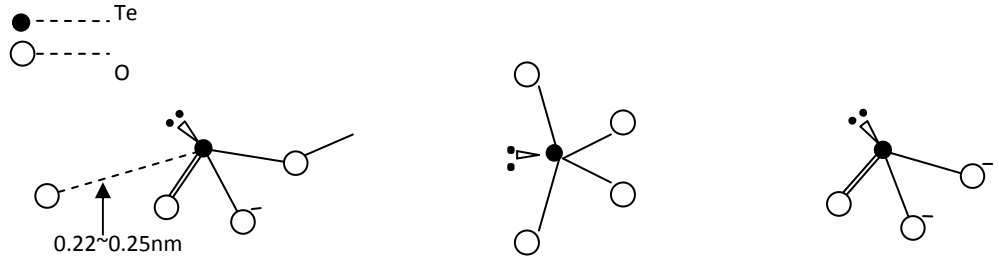

(a) [TeO_{3+1}] type (b) [TeO_4] type (c) [TeO_3] type

Fig. 4.1 Diagram of tellurium oxide entities

In tellurite niobic glass matrix, niobium oxide exists outside the tellurium oxide glass network as a modifier of the glass network structure. Nb^{5+} ions in tellurite glass exists partially in both NbO_6 octahedra (mainly non-bridging oxygen, NBO), and NbO_4 tetrahedra (mainly bridging oxygen, BO). The non-linear optical performance of glass is related to the local atomic structure, particularly, to the energy band gap. According to the Line's bond-orbital theory, the transition metal ions with empty d^0 atomic orbital such as Nb^{5+}, or ions with lone electron pair of Te^{4+}, can give rise to nonlinear optical responses. TeO_4 (tbps) consists of a lone electron pair and two oxygen atoms at the equatorial position and two oxygen atoms at the axial position. A theoretical approach through ab initio calculations led to the hybrid molecular orbital diagrams for the TeO_4 tbp and TeO_3 tp as shown in Fig. 4.2.

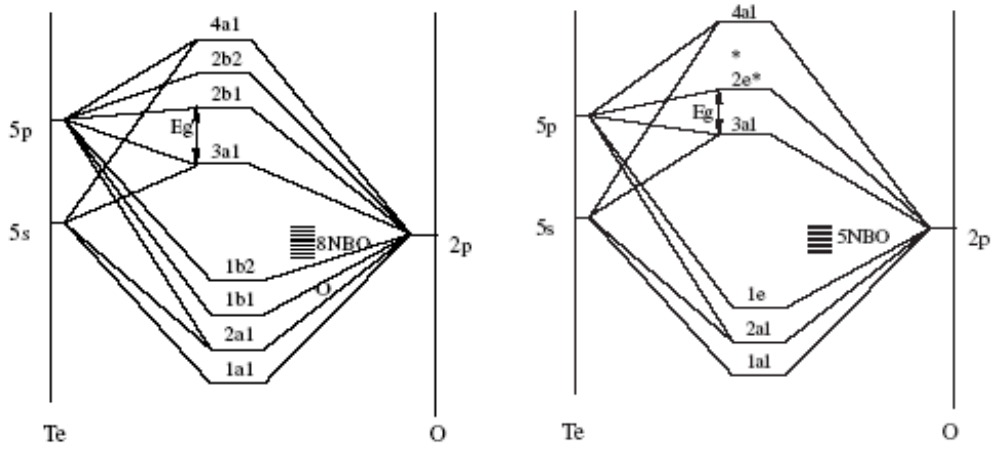

Fig. 4.2 Qualitative molecular orbital diagram of TeO_4 tbp (left) and TeO_3 tp (right), NBO: non-bridge oxygen orbit. E_g: the energy gap between HOMO and LUMO [155].

Theoretical calculations of optical non-linearity for glass indicated that the 3rd order non-linear optical susceptibility $\chi^{(3)}$ is inversely proportional to the mean energy gap E_g (as shown in the following,

$$\chi^{(3)} = \frac{\left(n_0^2+2\right)^2\left(n_0^2-1\right)}{C\pi n_0 N}\left(\frac{E_d}{E_g^2}\right), \tag{4.6}$$

where n_D, E_d, and N refer to the refractive index, the dispersion energy and the cationic bulk concentration of the glass, respectively. C is a constant. The energy gap Eg between HOMO and LUMO in TeO_4 tbp is 10.2eV, and that in TeO_3 tp is 12.1 eV. It suggests that TeO_4 tbp is more polarizable than TeO_3 tp, and the mean polarizability for TeO_4 tbp is about 20% higher than that for the TeO_3 tp.

4.2 Experiments

4.2.1 Fabrication of AgCl nanocrystals doped $80TeO_2$-$20Nb_2O_5$ glass

(a) Melting-Quenching

We use melting-quenching technique to fabricate base glassThe TeO_2 (Aldrich 99.99%) powder and the Nb_2O_5 (Aldrich 99.99%) powder were weighted at the molar ratio of 4:1, and the 1%wt AgCl powder (Aldrich 99.99%) as dopant is stirred homogenously with the TeO_2 (Aldrich 99.99%) and Nb_2O_5 (Aldrich 99.99%) powder in an agate mortar. The batch is dumped into a gold crucible and melted in a box furnace at 800°C for 15minutes, and the temperature fluctuation is less than 1°C during the melting process. The melted glass is poured onto a heat steel plate and coagulated to solid slices rapidly. All the glass samples are annealed at 300°C in a Muffle furnace in order to reduce glassy interior tension.

(b) Diffusion control

Silver chloride nanocrystalss can be grown at relatively low temperature (350°C), and so the doped glass was thermally treated in a Muffle furnace at 360°C for the nucleation and growth of AgCl nanocrystalss. The thermal treatment time varies from 30minuetes to 120minutes in order to control the mean grain-size of nanocrystalss.

Finally, the resultant glass samples are polished by the abrasive paper to optical grade within 2 mm thickness. The AgCl nanocrystals doped glass samples appear light-yellow, which become darker with extending the thermal treatment time.

4.2.2 The grain-size characterization of AgCl nanocrystalss

The morphology and crystallographic structure of a sample at an atomic scale were revealed by High resolution transmission electronic microscopy (HRTEM). We use JEOL-200F TEM to reveal the AgCl nanocrystals geometry and crystalline axis. The accelerate voltage is 200kV, and the resolution is 0.1nm at 20nm scale. The crystalline axis of glass is marked by selected area electron diffraction (SAED), and the sample were milled to small fraction (200nm) so that the electronic beam can penetrate the glass.

The size distribution of AgCl nanocrystalss is recorded by the Hitachi S-4800 FESEM camera with the resolution at 10nm, and the size-distribution is measured with line-crossing method.

4.2.3 Spectral Characterization

(a) Raman spectroscopy

We use Jobin-Yvon T64000 micro-Raman spectrometer to investigate the tellurite niobic glass. The light source is Innova 70C Ar+ continous wave (cw) laser (Coherent. Inc.) with the wavelength of 514.5nm, and the linewidth of <0.5 cm^{-1}. The spectral resolution is about 0.1cm^{-1}.

(b) Absorption Spectroscopy

UV-visible absorption spectra are characterized by UV-2802S (Unica Inc.). The absorption coefficient can be exacted with Beer-Lambert law:

$$A = \lg \frac{I_0}{I} = \lg \frac{100}{T\%} = \lg \frac{1}{T} = \alpha_0 LC \ , \tag{4.8}$$

where A is the absorbance, I_0 be the incident intensity, I be the tranmitted intensity, T be the transmittance, α_0 be the linear absorption coefficient, L be the thickness, and C be the molar concentration.

(c) Photoluminescence

Photoluminescence (PL) is a process in which a substance absorbs photons and then radiates photons back out. It is a powerful tool to investigate the energy level of chemical substance. In our experiment, the fluorescence spectra are achieved by Hitachi F-4500 with the ultraviolet excitation of 3.2eV, and the spectral range is from 400nm to 600nm.

4.2.4 Measurements of nonlinear optical properties

The nonlinear optical experimental setups are based on Spectra-Physics Tsunami/Spitfire femtosecond laser system with the 50 fs pulse duration at 1 KHz repetition rate, and the output energy fluctuation is less than 1%. The optical nonlinear absorption coefficients are measured by Z-scan experiment (appendix F) and the optical limiting is observed by recording both the incident and transmitted pulse energy. Their linear refractive indices are measured by a home-made Brewster-meter. Their $\chi^{(3)}$ are measured by degenerate four wave

mixing (DFWM) (see appendix E), and the signals are detected with a Si photodiode and Lock-in amplifier.

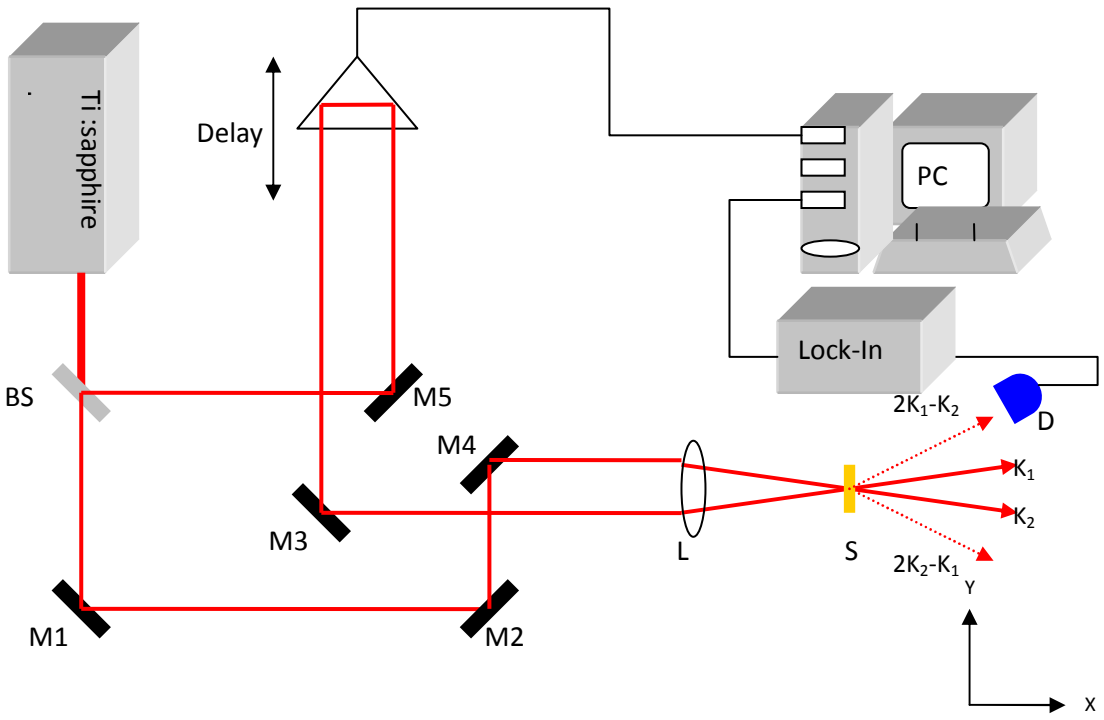

Fig. 4.3 Schematic diagram of DFWM experimental setup; M: reflective mirror, BS: beam-split, D: photodiode, PC: computer, S: sample, L: lens.

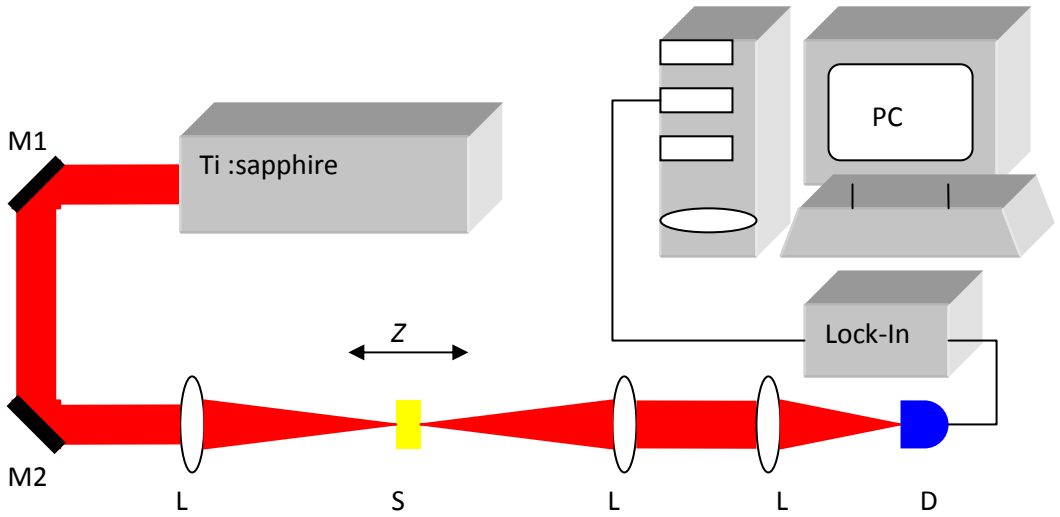

Fig. 4.4 Schematic diagram of Z-Scan experimental setup; M: reflective mirror, BS: beam-split, D: photodiode, PC: computer, S: sample, L: lens.

4.3 Results and Discussion

Niobic tellurite glass is formed by the line and chain linkage of tellurium oxide and niobic oxide with the bridge and non-bridge oxygen bond, and it exhibits excellent accommodation for dopants.

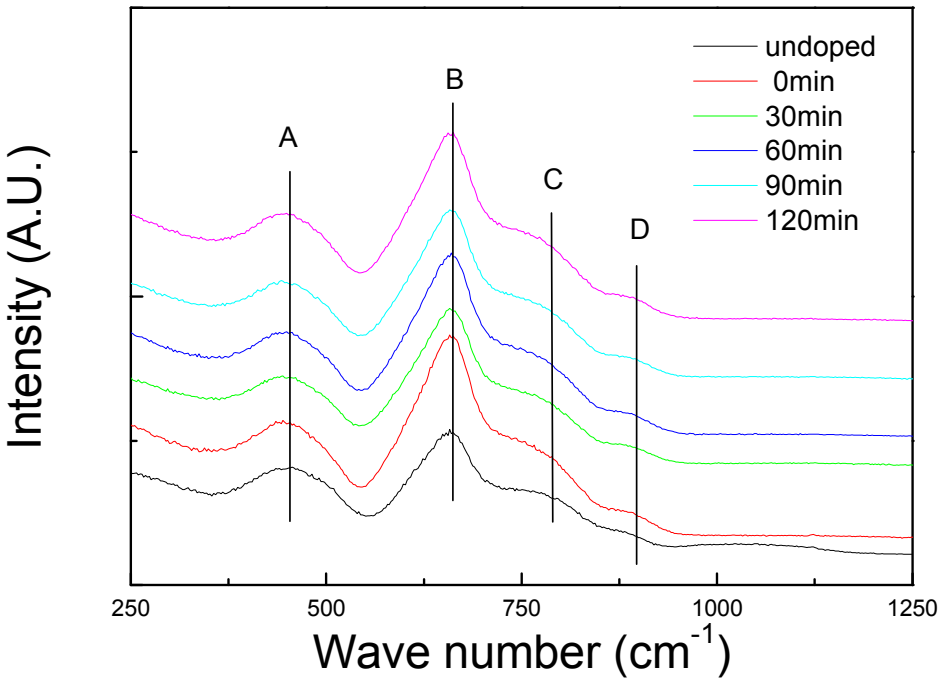

Fig. 4.5 Raman spectra of the undoped and doped glass samples thermally treated for different times

Fig.4.5 shows the Raman spectra of the undoped and doped glass samples thermally treated for different times. The peak A at 445cm-1 corresponds to the symmetric bending vibrational mode of Te-O-Te linkages at the corner-sharing sites. The symmetric stretching vibrational mode of Te-O_{ax} bonds in trigonal bipyramidal TeO_4 units occurs at 660cm^{-1} (peak B). The Te-O symmetric stretching vibrational mode in the structure of unit TeO_{3+1} cause the C peak at 760cm^{-1}. Nb_2O_5 is an intermediate, which results in the transition from TeO_4 to TeO_3 via TeO_{3+1} units and improves the formation of glass structural network.

The Nb^{5+} ion in NbO_4 tetrahedron takes part in as glass network former, f while the Nb^{5+} ion in NbO_6 octahedron occupies the interstitial position as glass network modifiers. The peak D at 890cm^{-1} corresponds to the Nb-O vibrational mode in the NbO_4 unit.

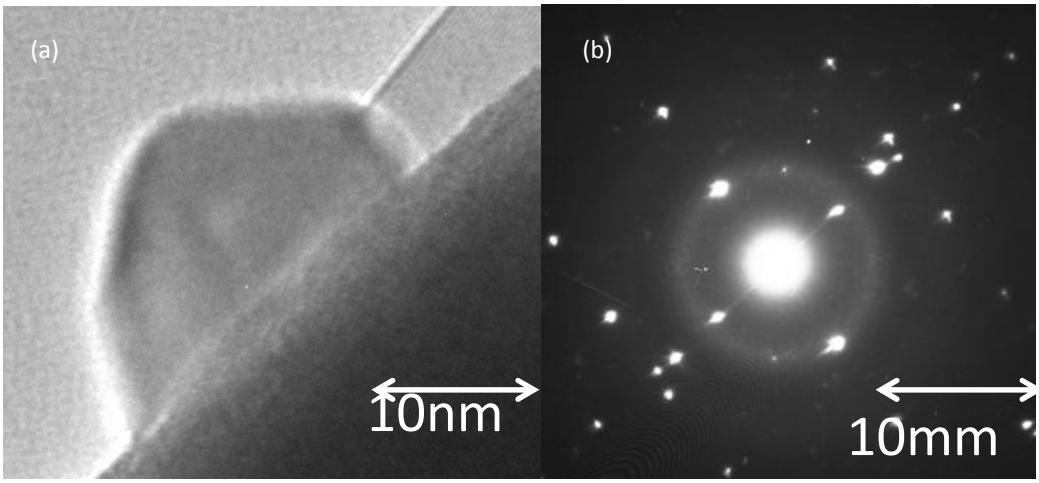

Fig. 4.6 (a) The morphology of AgCl nanocrystals embeded in the glass fraction, (b) the SAED pattern of AgCl nanocrystals,

The HRTEM image reveals the characherics of the nanocrystals dopant. As shown in Fig. 4.6(a), four small AgCl nanocrystalss with the distinct grain boundary are embedded inside the glass. The SAED pattern in Fig. 4.5 (b) shows regular point-array. The AgCl crystal belongs to the cubic family with [220] cubic symmetry, and the *d* value is calculated to be 1.96Å with the electron diffraction equation.

The surface grain density of AgCl nanocrystalss embedded in the tellurite niobic glass matrix. The small speckles in Fig. 4.6 (a) ~ (d) refer to the exposed nanocrystals grain embedded in samples treated for 30minutes, 60minutes, 90minutes and 120minutes. The crack on the glass surface refers to the inhomogeneous etching in HF solvent during the sample preparation

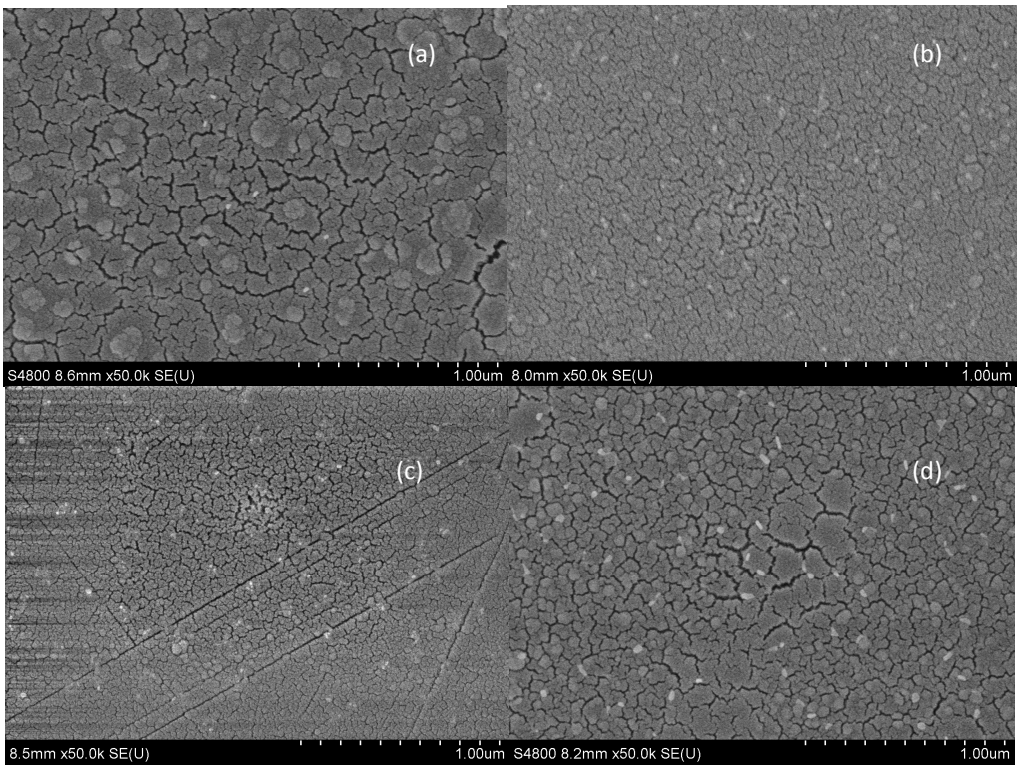

Fig. 4.7 FESEM image of the glass sample thermally treated for (a) 30minuetes, (b) 60minuetes, (c) 90minuetes, and (d) 120minuetes

Table 4.1 Size-distribution of AgCl nanocrystalss in glass matrix.

Thermal treatment time	Mean grain density (/μm^2)	Mean grain size (nm)
30 minutes	5	12
60 minutes	28	17
90 minutes	34	26
120 minutes	38	35

The surface density and size distribution of AgCl nanocrsytals are recorded by FESEM (as shown in Fig. 4.7 (a) ~ (d)), and the mean grain size and mean grain density of AgCl nanocrystalss in glass matrix are shown in Table 4.1. Their nanocrsytal sizes increase from 12 nm to 36 nm with the thermal treatment time increasing from 30 minutes to 120 minutes. These results indicate that the mean grain-size can be controlled by varying the thermal treatment time.

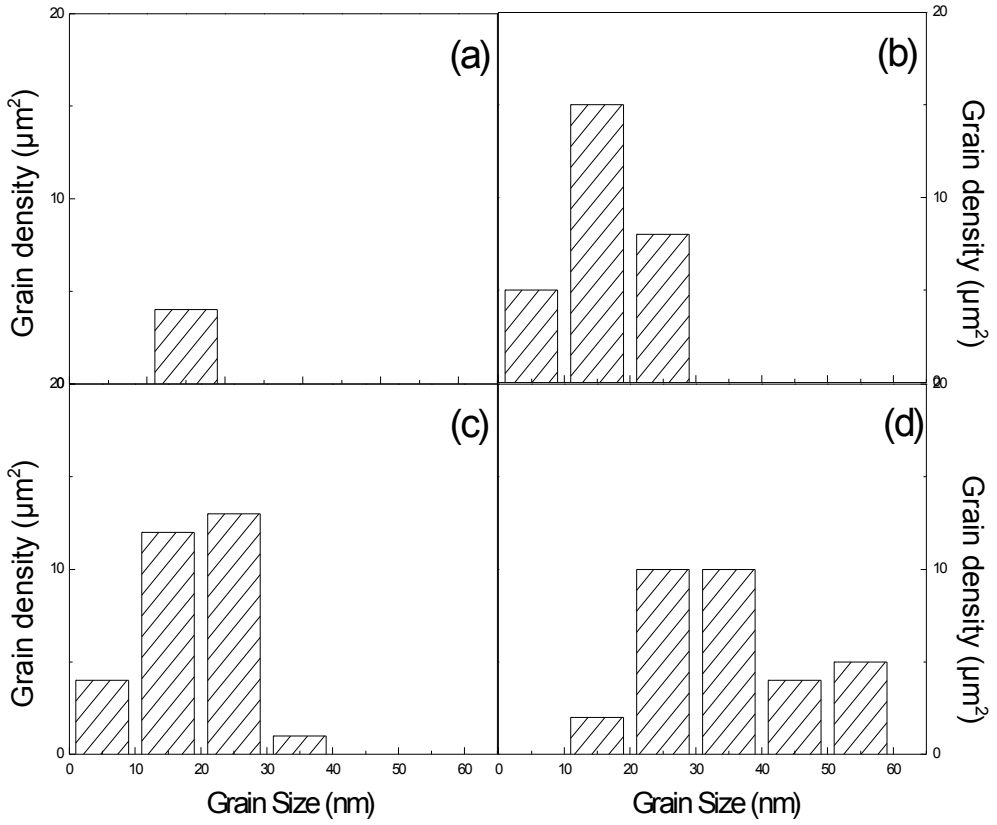

Fig. 4.8 The size distribution of AgCl nanocrystals for the heat treatment of 30 (a), 60 (b), 90 (c) and 120min (d), respectively.

The linear optical properties of the glass samples are investigated by the absorption and fluorescence spectroscopy.

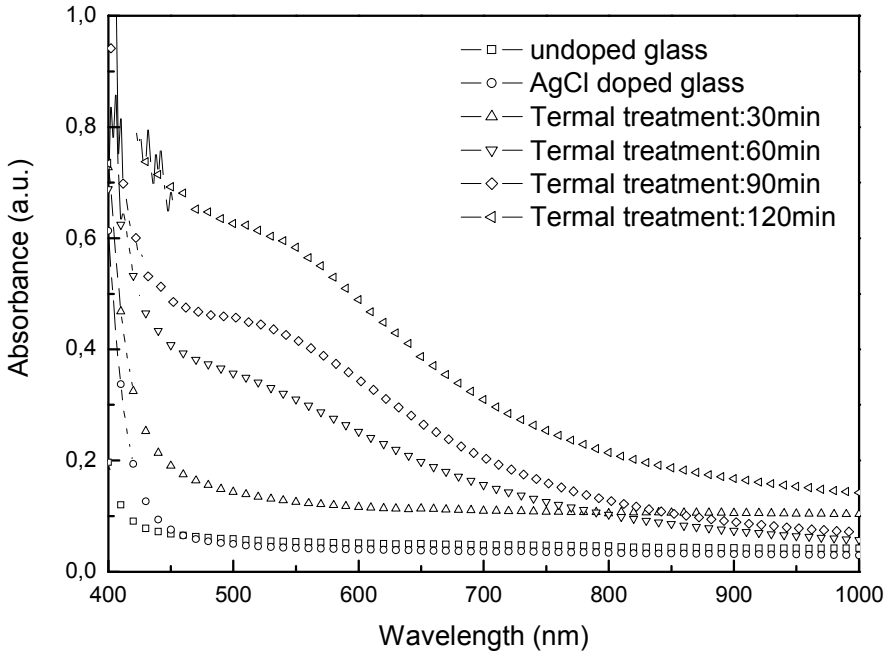

Fig. 4.9 Absorption spectra for the glass samples with different heat treatment time

Fig. 4.9 shows UV-VIS-NIR absorption spectra of the glass samples. It indicates that the undoped and doped glass samples without the thermal treatment exhibit a high transmittance in the visible region, and their absorption tails shift to longer wavelength with prolonging the thermal treatment time. The long absorption tails appear structureless, and can be attributed to the Cl^- colour center in the AgCl nanocrystalss. The AgCl nanocrystalss are thermally unstable, and will decompose at high temperature or under intense UV radiation, that is, the AgCl powders will partly decompose during the melting process via the reduction reaction: $2Cl^- \rightarrow Cl_2 + 2e^-$ and $2Ag^+ + 2e^- \rightarrow 2Ag$. For longer thermal treatment time, the dissociated chloride ions give rise to the amount of the Cl^- defects in the AgCl nanocrystalss, namely, the Cl^- colour centers. According to the Urbach law[159], the intrinsic bandgap of thermally treated glass can be represented as,

$$\alpha(\nu) = \alpha_m \exp\left(\frac{\sigma}{KT}\left(h\nu - E_g\right)\right), \tag{4.14}$$

where α is the absorption coefficient, α_m is the initial absorption value, σ is the constant determined by exciton-photon interaction, hν is the incident photon energy, K is Boltzmann constant, T is temperature, and E_g is the bandgap. As shown in Table 4.2, the simulation indicates that the bandgap becomes much narrower in the samples thermally treated for 30,

60, 90 and 120 minutes, respectively. Therefore, the longer thermal treatment time results in more defects in the AgCl nanocrystalss, and so it will influence their bandgap.

Meanwhile, the defects on the surface of the AgCl nanocrystalss will lead to larger local field on the interface between the glass host matrix and the AgCl nanocrystalss. The decomposed AgCl can lead to the enrichment of Ag^+ in the doped glass so that the glass ligand O^{2-} will distort Ag^+ at the interface. Ag^+ will transfer to the trapped state Ag^{2+} with an oxidation reaction, and so it results in the AgCl lattice deformation. Jahn-Teller effect [157] can form the Ag^+ *4d* admixture at the valence band maximum and cause the trapped hole in a molecular-ion lattice deformation $(AgCl_6)^{4-}$ cluster. Ag^{2+} exists in the deformed cluster, and is bound with a localized electron, and so it results in the self-trapped exciton (STE). The bound-energy of STE is very low so that the hole-electron will be recombined. The previous report [157] shows that the electron-hole recombination via STE gives a green luminescence band at 2.5eV.

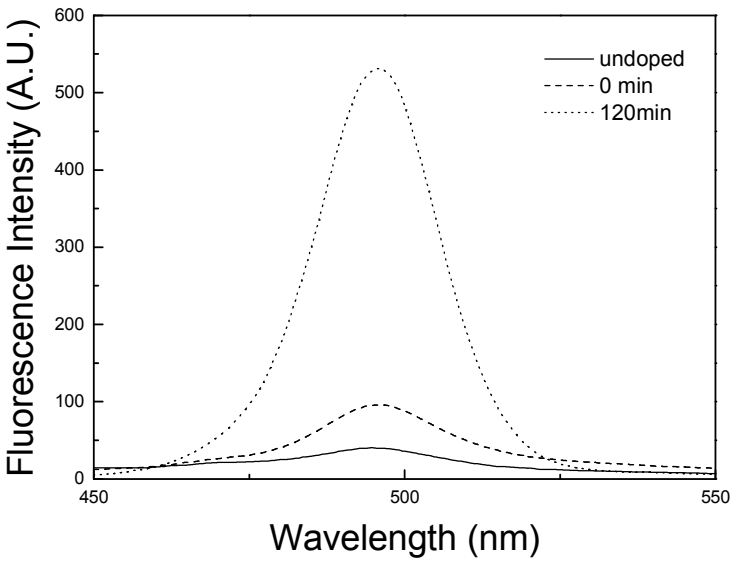

Fig. 4.10 Fluorescence spectra of undoped, untreated and treated glass samples

Fig. 4.10 indicates there is a distinct 496nm photoluminescence peak (2.5eV) with the FWMH of 60meV, and it will be enhanced as the thermal treatment increasing. The experimental results are consistent with the published data [157] and it can be deduced that longer thermal treatment time will cause more trapped states in the AgCl nanocrystals.

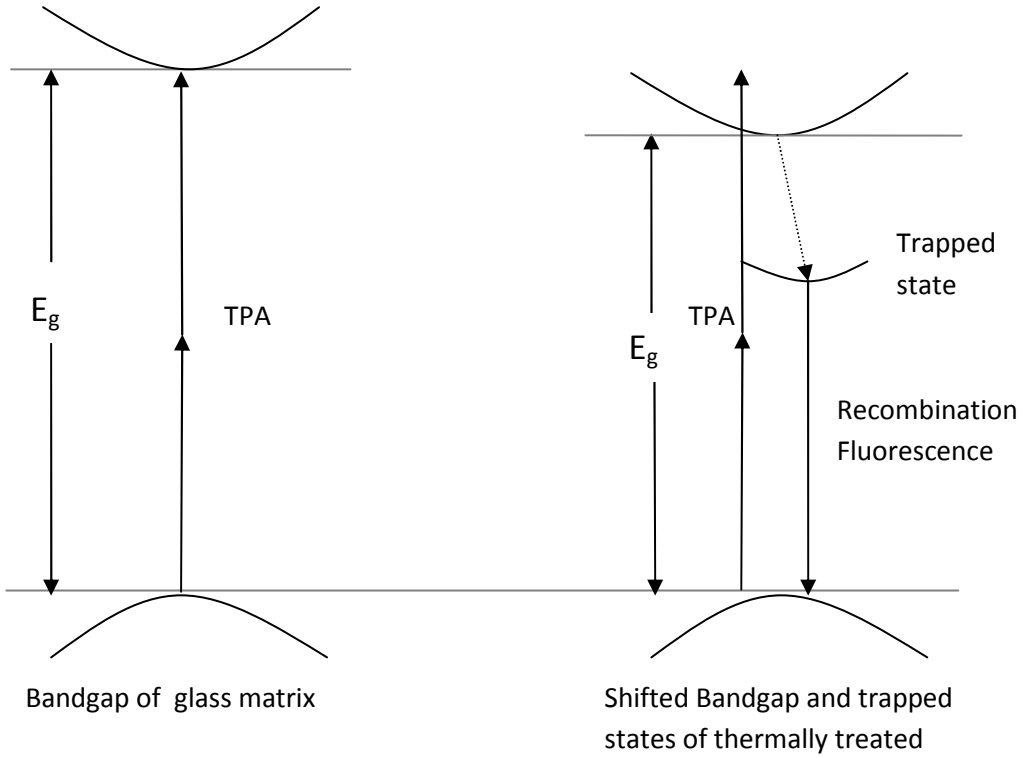

Fig. 4.11 Diagram of electron transition of glass under 800nm femtosecond laser excitation

The trapped state maybe contributes to the nonlinear optical properties of glass. The $\chi^{(3)}$ of our samples were indicated in Fig. 4.11and table 4.2.

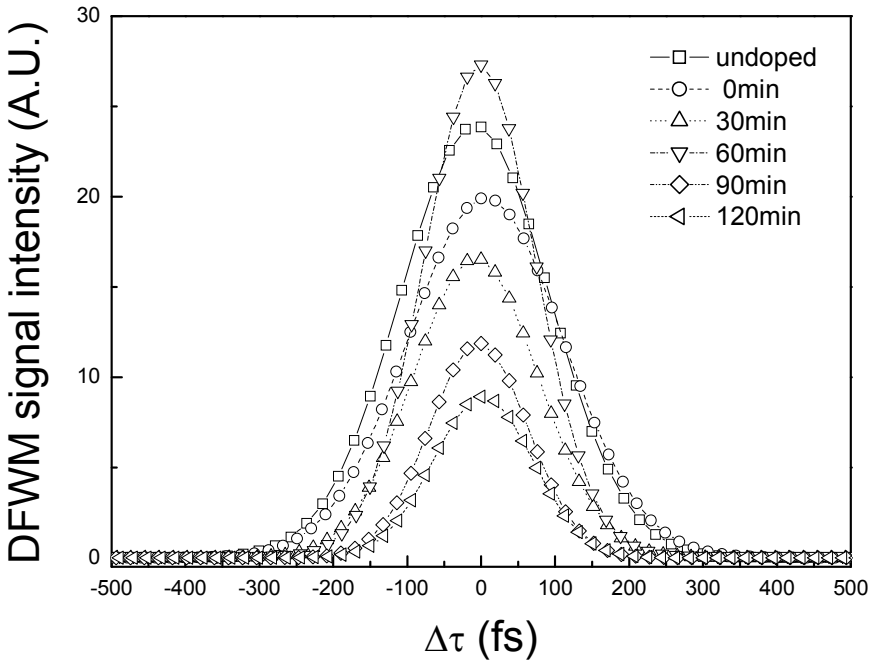

Fig. 4.12 DFWM experimental data and the Gaussian fitting lines

In order to explore third-order optical nonlinearities, their degenerate four wave mixing (DFWM) signals have been measured (as shown in Fig. 4.12). Their third-order nonlinear susceptibilities are calculated by the following equation,

$$\chi^{(3)} = \left(\frac{I}{I_{cs_2}}\right)^{\frac{1}{2}} \frac{L_{cs2}}{L}\left(\frac{n_0}{n_{cs_2}}\right)^2 \left\{\frac{\alpha_0 L \exp\left(\frac{\alpha_0 L}{2}\right)}{1-\exp\left(-\alpha_0 L\right)}\right\} \chi^{(3)}_{Cs_2} \tag{4.15}$$

I is the DFWM signal intensity, L is the sample thickness, α_0 is linear absorption coefficient, and n_0 is the linear refractive index. Here, CS_2 is used as the reference sample, and the nonlinear refractive index can be calculated by,

$$n_2 = \left(\frac{12\pi}{n_0}\right)\chi^{(3)} \tag{4.16}$$

The response time is hundreds of femtosecond, and so the nonlinear refractive index can be attributed to the transient polarized bound electrons. Both the nanocrystals inclusion and the host matrix have contributions to the effective third-order nonlinear susceptibility. As shown in Fig. 4.13 and Table 4.2, the nanocrystals AgCl inclusion can results in the enhancement of third-order optical nonlinearities. The contributions of the host matrix to third-order nonlinear

susceptibility can be assumed to be equal for the different samples. Microscopically, the nanocrystals AgCl inclusion can introduce the defect centers at the crystalline interface, and there is strong Coulomb influence on the oxide anions in the tellurite ligands and results in a large interface polarization in the trapped states. The third-order optical nonlinearities of the trapped state electrons will be enhanced by the local field, and so it gives arise to larger third-order optical nonlinear susceptibility $\chi^{(3)}$. However, Table 4.2 indicates that the nonlinear refractive index decreases as the thermal treatment time is up to more than 60minutes. Mie scattering theory indicated that the laser beam can be scattered by the grain, and the grain-size and density determine the extinction cross-section σ. FESEM images indicate their nanocrsytal sizes increase from 12 nm to 36 nm with the thermal treatment time from 30 minutes to 120 minutes. An increase of the AgCl nanocrystals grain-size will results in more optical scattering, and diminish DFWM signal. Therefore, the measured data is less than the theoretical expectation. It is deduced that the real nonlinear refractive index of the samples thermally treated for 90 and 120 minutes should be much larger than that of the samples thermally treated for 60 minutes.

The optical limiting of the AgCl nanocrystals doped niobic tellurite glass is illustrated in Fig. 4.13. Larger particles have better optical limiting performance and the saturable threshold reduces. The nonlinear absorption coefficient was investigated by open aperture Z-scan. As shown in Fig.4.11, the bandgap E_g of the glass sample is in the range of 1.7ev~3.0eV, and the laser photon energy of 1.55eV satisfies the two-photon absorption (TPA) condition: $E_g < h\nu < 2E_g$. The TPA process is governed by the following relation,

$$\frac{\partial N}{\partial t} = -\frac{\alpha_0 I}{h\nu} - \frac{\beta I^2}{h\nu} \tag{4.17}$$

$$\frac{dI}{dz} = 1 - \frac{\beta I\left(1 - e^{-\alpha_0 L}\right)}{\alpha_0\left(1 + \frac{z^2}{z_0^2}\right)^{\frac{1}{2}}} \tag{4.18}$$

where L is the sample thickness, α_0 represents the linear absorption coefficient, β is the TPA coefficient, I is the incident optical intensity, and $h\nu$ is the incident photon energy. As shown in Fig. 4.15, the z-scan fitting curves and their calculation illustrate that the TPA coefficient β of the untreated samples is about 1GW/cm, which increases to 1.3GW/cm for the glass sample thermally treated for 120 minutes. Absorption spectra show that the sample thermally

treated for 120minutes has larger absorption coefficient than the undoped glass (see the absorption tails in Fig. 4.10), so that more incident laser energy is absorbed by one photon excitation. Consequently, the residual energy contributed to TPA will be diminished. Hence, the corresponding Z-scan valley seems to be less deep than the undoped sample. It was reported that the dependence of the TPA coefficient β on the bandgap E_g is,

$$\beta \propto \frac{1}{E_g^3} \tag{4.19}$$

Therefore, the redshift of the absorption band will increase TPA cross-section and diminish the saturable transmitted optical intensity. Meanwhile, the Urbach tail in the absorption region refers to the local state of the glass sample, so that one photon excitation (1.55eV/800nm) induces local carrier absorption (LCA). In fact, longer thermal treatment time causes more trapped states in the AgCl nanocrystalss, and it will enhance the local carrier state density. Therefore, the local carrier absorption of more AgCl trapped states induces the near-resonant enhancement of nonlinear absorption coefficient and optical limiting performance.

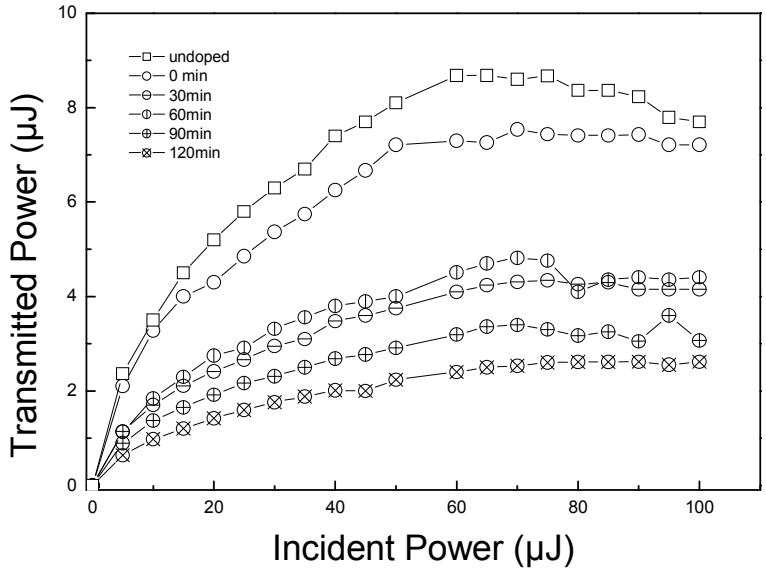

Fig. 4.13 Optical limiting of the AgCl nanocrystals doped glass samples with different thermal treatment time.

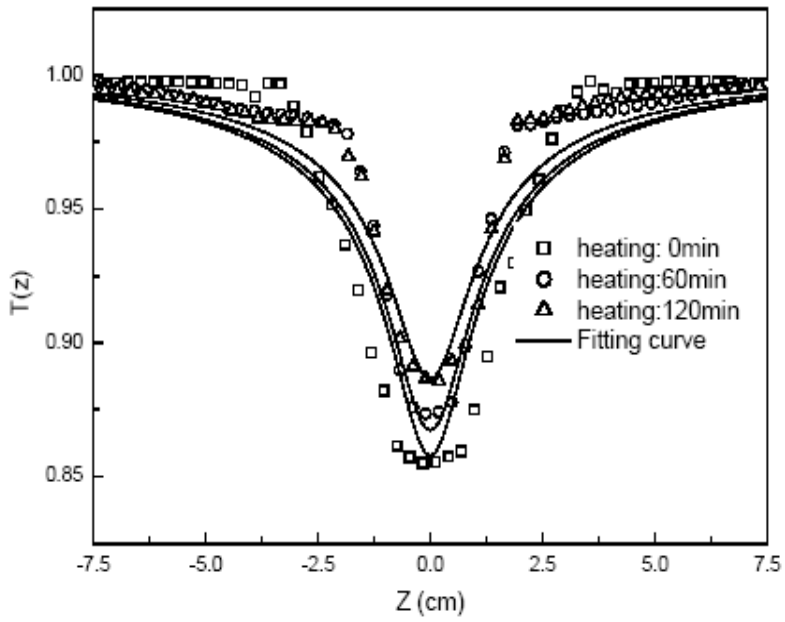

Fig. 4.14 Open-aperture z-scan curves of the AgCl nanocrystals doped glass samples with different thermal treatment time.

Table 4.2 The linear and nonlinear optical parameters: E_g is the bandgap, n_0 is the linear refractive index, $\chi^{(3)}$ is third-order nonlinear susceptibility, n_2 is nonlinear refractive index

Samples	E_g (eV)	n_0	$\chi^{(3)}$ (10^{-13}esu)	n_2 (10^{-11}esu)
undoped	3.1	2.0	7.2	1.2
0 min	2.9	2.1	7.3	1.3
30 min	2.6	2.2	7.8	1.4
60 min	2.3	2.2	14	2.3
90 min	1.9	2.2	11	1.9
120 min	1.7	2.2	9.5	1.6

Meanwhile, the Urbach tails in the absorption region refers to the local state of glass, so that one photon excitation (1.55eV/800nm) induced local carriers absorption (LCA). LCA also contributes to the optical limiting for the thermal treated samples.

Summary:

In summary, non-resonant ultrafast nonlinear optical properties of silver chloride (AgCl) nanocrystals doped niobic tellurite glass ($80TeO_2$-$20Nb_2O_5$) have been investigated by femtosecond DFWM and Z-scan technique. The longer thermal treatment time can increase nanocrystals's grain-size and cause more defect centers and stronger lattice deformation at the interface of the AgCl nanocrystals, and so it gives arise to the formation of self-trapped exciton and the absorption tail redshift. The larger two photon absorption and local state carrier absorption result in a decrease of the optical limiting threshold, and the third order nonresonant nonlinear susceptibility $\chi^{(3)}$ can be enhanced for the transient polarization of trapped state electrons on the surface of the AgCl nanocrystals.

Conclusion

We developed a THz-TDS setup with 2 types of emitters: optical rectification in ZnTe and interdigitated photoconductive antennas. We studied their THz performances. We used this homemade THz-TDS system to investigate the gain of a 2.9THz QCL.

In the case of the ZnTe emitter, the several nonlinear mechanisms diminish the THz emission efficiency. Diffraction effects are essential in the understanding of the THz emission when the pump beam is focused. Taken into account properly the diffraction effect, TPA can be shown to result in the formation of a strong reduction of the THz emission upon focusing, in the form of a "z-hole". Here, we also show that free-carrier absorption cannot be neglected. Nevertheless, free-carrier absorption only tends to scale down the measured THz power and cannot, by itself, explain the formation of a z-hole.

In THz emission from an interdigitated photoconductive antenna was characterized. The neutral impurity scattering dominates the mobility below 70K while the deformation potential scattering dominates the mobility above 70K.

Then, we have used THz-TDS to investigate the gain of a QCL, showing the evolution of the gain as a function of current and demonstrating the effect of gain clamping. Furthermore, we obtain phase information directly from the measurement, without resorting to the Kramers-Kronigs relations. The effect of temperature was also investigated highlighting the reduction in gain at high temperatures where the laser does not operate. Further developments will focus on QCLs operating at lower frequencies where the spectral intensity of the antenna is greater.

Finally, we revealed the fabrication, characterization and nonlinear optical properties of AgCl NCs doped $80TeO_2$-$20Nb_2O_5$ glasses. The lattice defects of AgCl nanocrystals in glass result in self-trapped exciton. Under the near-resonant excitation condition, the self-trapped exciton saturable absorption induces optical limiting. The longer heat treatment time enhances the optical limiting. The ultrafast optical performance below bandgap of AgCl nanocrystalss doped $80TeO_2$-$20Nb_2O_5$ glasses were investigated by experiments. The results indicate that the self-trapped exciton of AgCl nanocrystalss influence the 3^{rd} order optical nonlinearity. The longer thermal treatment time expanse nanocrystals's grain-size caused more defect center and stronger lattice deformation at the interface of AgCl nanocrystals which gives arise to the formation of self-trapped exciton. The ESA between trapped state and glass continuum

band deduces the saturable transmitted optical intensity so that enhance optical limiting. The 3rd order nonlinear susceptibility $\chi^{(3)}$ depends on the competition between transient polarization and scattering process. First, transient polarization of bound electron in self-trapped exciton enhances $\chi^{(3)}$ of nanocrystalss doped glasses while the increase of grain-size and density of nanocrystalss simultaneously enlarge the scattering cross-section which degrade $\chi^{(3)}$. The grain-size of AgCl determined the maximum value of $\chi^{(3)}$ below bandgap in AgCl nanocrystalss doped ionic tellurite glass.

Reference

[1] Jagdeep Shah, *Ultrafast Spectroscopy of Semiconductors and Semiconductor Nanostructures*, Springer-Berlin 2nd edition, 1998

[2] Takeshi Kamiya, *Femtosecond Technology: From Basic Research to Application Prospects*, Springer-Berlin 1st edition, 1999

[3] Kong Thon Tsen, *Ultrafast Dynamical Processes in Semiconductors*, Springer-Berlin 1st edition, 2004

[4] A. G. Davies, E. H. Linfield, and M. B. Johnston, "The development of terahertz sources and their applications", *Phys. Med. Biol.*, **47**: 3679–3689 (2002)

[5] B. Ferguson and X.-C. Zhang, "Materials for terahertz science and technology", *Nature Materials*, **1**: 26-33 (2002)

[6] C. A. Schmuttenmaer, "Exploring Dynamics in the Far-Infrared with Terahertz Spectroscopy", *Chem. Rev.*, **104**: 1759-1779 (2004)

[7] M. van Exter, D. Grischkowsky, "Carrier dynamics of electrons and holes in moderately doped silicon", *Phys. Rev. B*, **41**: 12140 (1990)

[8] M. van Exter, D. Grischkowsky, "Optical and electronic properties of doped silicon from 0.1 to 2 THz", *Appl. Phys. Lett.*, **56**: 1694 (1990)

[9] T.-I. Jeon, D. Grischkowsky, "Nature of Conduction in Doped Silicon", *Phys. Rev. Lett.*, **78**: 1106 (1997)

[10] T.-I. Jeon, D. Grischkowsky, "Characterization of optically dense, doped semiconductors by reflection THz time domain spectroscopy", *Appl. Phys. Lett.*, **72**: 3032 (1998)

[11] Q. Wu, X.-C. Zhang, "Ultrafast electro-optic field sensors", *Appl. Phys. Lett.*, **68**: 1604 (1996)

[12] A. Nahata, A.S. Weiling and T.F. Heintz, "A wideband coherent terahertz spectroscopy system using optical rectification and electro-optic sampling", *Appl. Phys. Lett.*, **69**: 2321 (1996)

[13] D. Mittleman editor, *Sensing with TeraHertz Radiation*, Springer, Berlin (2003).

[14] D.H. Auston, "Cherenkov radiation from femtosecond optical pulses in electro-optic media", *Phys. Rev. Lett.*, **53**: 1555 (1984)

[15] L. Xu, X.-C. Zhang and D.H. Auston, "Terahertz beam generation by femtosecond optical pulses in electro-optic materials", *Appl. Phys. Lett.*, **61**: 1784 (1992)

[16] D. Grischkowsky, in *Frontiers in Nonlinear Optics*, Ed. H. Walther, N. Koroteev, M.O. Scully (Philadelphia, 1993) p. 196.

[17] X.-C. Zhang, B.B. Hu, J.T. Darrow, D.H. Auston, "Generation of femtosecond electromagnetic pulses from semiconductor surfaces", *Appl. Phys. Lett.*, **56**: 1011 (1990)

[18] F.G. Sun, X.-C. Zhang, in *Conference on Lasers and Electro-Optics (CLEO), OSA Technical Digest* (Washington DC 2000) p. 479.

[19] M. Schall and U. Jepsen, "Above-band gap two-photon absorption and its influence on ultrafast carrier dynamics in ZnTe and CdTe", *Appl. Phys. Lett.*, **80**: 4771 (2002)

[20] Faist, Jerome, Federico Capasso, Deborah L. Sivco, Carlo Sirtori, Albert L. Hutchinson, and Alfred Y. Cho, "Quantum Cascade Laser". *Science* **264** (5158): 553-556 (1994)

[21] Carlo Sirtori, P. Kruck, S. Barbierie, P. Collot, J. Nagle, M; Beck, J. Faist, and U. Osterle, "GaAs/AlGaAs quantum cascade laser", *Appl. Phys. Lett.*, **73**: 3468-3488 (1998)

[22] Rüdeger Köhler, Alessandro Tredicucci, Fabio Beltram, Harvey E. Beere, Edmund H. Linfield, Giles A. Davies, and David A. Ritchie, *Advances in Solid State Physics*, Springer Berlin (2003)

[23] J. Faist, L.Aijili, G. Scalari, M. Giovanimi, M. Beck, M. Rochat, H. Beere, A. G. Davis, E. H. Linfield, and D. Ritchie, "Terahertz Quantum Cascade Lasers", *Phil. Trans. R. Soc. Land.*, **362**: 215-231 (2004)

[24] C. Walther, G. Scalari, J. Faist, H. Beere, and D. Ritchie, "Low frequency terahertz quantum cascade laser operating from 1.6 to 1.8 THz", *Appl. Phys. Lett.*, **89**: 231121 (2006).

[25] S. S. Dhillon, J. Alton, S. Barbieri, C. Sirtori, A. de Rossi, M. Calligaro, H. E. Beere, D. A. Ritchie, "Ultra-low threshold current THz quantum cascade lasers based on buried-strip waveguides", *Appl. Phys. Lett.*, **87**: 071107 (2005).

[26] Y. Chassagneux, J. Palomo, R. Colombelli, S. Dhillon, C. Sirtori, H. Beere, J. Alton, D. Ritchie, "THz microcavity lasers with sub-wavelength mode volumes and thresholds in the milli-Ampere range", *Appl. Phys. Lett*., **90**: 091113 (2007).

[27] S. Barbieri, J. Alton, H. Beere, J. Fowler, E. Linfield, and D. A. Ritchie, "2.9 THz quantum cascade lasers operating up to 70 K in continuous wave", *Appl. Phys. Lett.*, **85**: 1674, (2004).

[28] B. S. Williams, S. Kumar, Q. Hu, and J. L. Reno, "Operation of terahertz quantum-cascade lasers at 164 K in pulsed mode and at 117 K in continuous-wave mode", *Opt. Express.*, **13**: 3331 (2005).

[29] G. Dakovski, B. Kubera and J. Shan, "Localized terahertz generation via optical rectification in ZnTe", *J. Opt. Soc. Am. B* **22**:1667 (2005)

[30] V.Y. Gaivoronskii, M.M. Nazarov, D.A. Spapozhnikov, E.V. Shepelyavyi, S.A. Shkel'nyuk, A.P. Shkurinov and A.V. Shuvaev, "Competition between linear and nonlinear processes during generation of pulsed terahertz radiation in a ZnTe crystal", *Quant. Electron.*, **35**: 407 (2005)

[31] J.Z. Xu and X.-C. Zhang, "Optical rectification in an area with a diameter comparable to or smaller than the center wavelength of terahertz radiation", *Opt. Lett.*, **27**: 1067 (2002)

[32] P.Y. Yu and M. Cardona, *Fundamentals of Semiconductors* (Springer-Verlag, Berlin, 1999).

[33] A. Dreyhaupt, S. Winnerl, T. Dekorsy et. al., "High-intensity terahertz radiation from a microstructured large-werea photoconductor", *Appl. Phys. Lett.*, **86**: 121114 (2005)

[34] A. Dreyhaupt, S. Winnerl, T. Dekorsy et. al., ”Optimum excitation conditions for the generation of high-electric-field terahertz radiation from an oscillator-driven photoconductive device”, *Opt. Lett.*, **31**: 1546-1548 (2006)

[35] T. Hattori, K. Egawa, S. Ookuma, et. al., “Intense terahertz pulses from large-aperture antenna with interdigitated electrodes”, *Jpn. J. Appl. Phys.*, **45**: L422-L424 (2006)

[36] A.G. Markelz and E.J. Heilweil, “Temperature-dependent terahertz output from semi-insulating GaAs photoconductive switches”, *Appl. Phys. Lett.*, **72**: 2229 (1998)

[37] G.Rodriguez and A.J.Taylor, “Screening of the bias field in terahertz generation from photoconductors”, *Opt. Lett.*, **21**: 1046 (1996)

[38] B. B. Hu, X.-C. Zhang, D. H. Auston, and P. R. Smith, “Free space radiation from electro-optical crystals”, *Appl. Phys. Lett.*, **56**: 506-508 (1990)

[39] F. Eickenner, R. A. Kaindl, M. Woerner, T. Elsaesser, S. Barberie, P. Krunk, C. Sirtori, and P. Nagle, “Large electrically induced transmission changing in GaAs/AlGaAs quantum cascade structure”, ”, *Appl. Phys. Lett.*, **76**: 3254-3256 (2000)

[40] F. Eickenner, K. Reinmman, M. Woerner, T. Elsaesser, S. Barberie, and C. Sirtori, “Ultrafast electron coherent transport in semiconductor quantum cascade structures”, *Phys. Rev. Lett.*, **89**: 047402-047404 (2002)

[41] J. Kröll, J. Darmo, S. Dhillon, X. Marcadet, M. Caligaro, C. Sirtori, and K. Unterrainner, “Phase resolved measurements on stimulated emission”, *Nature*, **449**: 698-702 (2008)

[42] J. Kröll, J. Darmo, S. Dhillon, X. Marcadet, M. Caligaro, C. Sirtori, and K. Unterrainner, “Longitude spatial hole burning in quantum cascade laser”, *Appl. Phys. Lett.*, to be published

[43] R. El-Mallawany, “Tellurite Glasses: Part 1. Elastic Properties”, *Mater. Chem. Phys.*, **53**: 93-120 (1998)

[44] R. El-Mallawany, “Tellurite Glasses: Part 2. Anelastic, phase separation, Debye temperature and thermal properties”, *Mater. Chem. Phys.*, **60**: 103 (1999)

[45] R. Jose and Y. Ohishi, “Enhanced Raman gain coefficients and bandwidths in P_2O_5 and WO_3 added tellurite glasses for Raman gain media”, *Appl. Phys. Lett.*, **89**: 121122-121124 (2006)

[46] G. Senthil Murugan, T. Suzuki, Y. Ohishi, “Tellurite glasses for ultrabroadband fiber Raman amplifiers”, *Appl. Phys. Lett.*, **86**: 161109-161111 (2005)

[47] G. Senthil Murugan, T. Suzuki, Y. Ohishi, “Phospho-tellurite glasses containing heavy metal oxides for ultrabroad band fiber Raman amplifiers”, *Appl. Phys. Lett.*, **86**: 221109-221111 (2005)

[48] E.Wu, Hao Chen, Zhenrong Sun, Heping Zeng, "Broadband saturable absorber with cobalt-doped tellurite glasses," *Opt. Lett.*, **28**: 1692 (2003)

[49] N. K. Giri, A. K. Singh, S. B. Rai, “Efficient blue upconversion emission in Tm^{3+} via energy transfer from Yb^{3+} doped in lithium modified tellurite glass”, *J. Appl. Phys.*, **101**: 033102-033105 (2007)

[50] L. Huang, A. Jha, S. Shen, X. Liu, “Broadband emission in Er^{3+}-Tm^{3+} codoped tellurite fibre”, *Opt. Express.*, **12**: 2429-2434 (2004)

[51] S. Shen, B. Richards, A. Jha, “Enhancement in pump inversion efficiency at 980 nm in Er^{3+}, Er^{3+}/Eu^{3+} and Er^{3+}/Ce^{3+} doped tellurite glass fibers”, *Opt. Express.*, **14**: 5050-5054 (2006)

[52] R. Souza, M. Alencar, J. M. Hickmann, R. Kobayashi, L. R. P. Kassab, “Femtosecond nonlinear optical properties of tellurite glasses”, *Appl. Phys. Lett.*, **89**: 171917-171919 (2006)

[53] M. Yamane, Y. Asahara, *Glasses for photonics*. (Cambridge Press, 2000)

[54] G. P. Banfi, V. Degiorgio and D. Ricard, “Nonlinear optical properties of semiconductor nanocrystalss,” *Adv. Phys.*, **47**: 447-510 (1998)

[55] E. Hanamura, “Very large optical nonlinearity of semiconductor microcrystallites”, *Phys. Rev. B* **37**: 1273-1279 (1987)

[56] T. Hiroshima, “Nonresonant excitonic optical nonlinearity in semiconductors”, *Phys. Rev. B* **40**: 3862-3866 (1989)

[57] D. Cotter, M.G. Burt, R.J. Manning, "Below-band-gap third-order optical nonlinearity of nanometer-size semiconductor crystallites", *Phys. Rev. Lett.*, **68**: 1200-1203 (1992)

[58] G. P. Banfi, V. Degiorgio, D. Fortusini, H. M. Tan, "Third-order nonlinearity of semiconductor doped glasses at frequencies below band gap", *Appl. Phys. Lett.*, **67**: 13-15 (1995)

[59] L. A. Padilha, A. A. R. Neves, E. Rodriguez, C. L. Cesar, L. C. Barbosa, C. H. Brito Cruz, "Ultrafast optical switching with CdTe nanocrystalss in a glass matrix", *Appl. Phys. Lett.*, **86**: 161111-161113 (2005)

[60] B. L. Yu, C.-S. Zhu, F.-X. Gan, "Nonlinear optical absorption and refraction by CdTe microcrystals doped in glass", *J. Appl. Phys.*, **87**: 1759-1761 (2000)

[61] M. Bass, P. A. Franken, J. F. Ward, and G. Weinreich, "Optical Rectification", *Phys. Rev. Lett.*, **9**(11) : 446-448 (1962)

[62] D. H. Auston, "Picosecond optoelectronic switching and grating in silicon", *Appl. Phys. Lett.*, **26**(3): 101-103 (1975)

[63] T. Yajima and N. Takeuchi, "Far-infrared difference frequency generation by picosecond laser pulse", *Jpn. J. Appl. Phys.*, **9**: 1361-1371 (1970)

[64] J. R. Morris and Y. R. Shen, "Generation of far-infrared radiation by picosecond light pulses in electro-optical materials", *Opt. Commun.*, **3**(2): 81-84 (1971)

[65] K. H. Yang, P. L. Richard, and Y. R. Shen, "Generation of far-infrared radiation by picosecond light pulse in $LiNbO_3$", *Appl. Phys. Lett.*, **19**: 320-322 (1971)

[66] D. H. Auston, A. M. Glass, and P. Lefur, "Tunable far-infrared generation by difference frequency mixing of dye lasers in reduced lithium niobate", *Appl. Phys. Lett.*, **23** (1) : 47-49 (1973)

[67] X.-C. Zhang, Y. Jin, K. Yang, and L. J. Schowalter, "Resonant nonlinear susceptibility near the GaAs bandgap", *Phys. Rev. Lett.*, **69**: 2303-2306 (1992)

[68] A. Rice, Y. Jin, X.-F. Ma, X.-C. Zhang, D. Bliss, J. Larkin, and M. Alexander, "Terahertz optical rectification from [110] zincblende crystals", *Appl. Phys. Lett.*, **64**(11) : 1324-1326 (1994)

[69] X.-C. Zhang, X.-F. Ma, Y. Jin, T. M. Lu, E. P. Boden, P. D. Phelps, K. R. Stewart, and C. P. Yakymyshyn, "Terahertz optical rectification from an organic crystal", *Appl. Phys. Lett.*, **61**: 3080-3082 (2003)

[70] A. Schneider, I. Biaggio, and P. Cunter, "Optimized generation of THz pulses via optical rectification in the organic salt DAST", *Opt. Commun.*, **224**(1-6): 337-341 (2003)

[71] A. Nahata, D. H. Auston, C. J. Wu, and J. T. Yardley, "Generation of terahertz radiation from a poled polymer", *Appl. Phys. Lett.*, **67**(10): 1358-1360 (1995)

[72] A. Bouvalet, M. Joffre, J. L. Martin, and A. Migus, "Generation of ultrabroadband femtosecond pulses in the midi-infrared by optical rectification of 15fs light-pulse at 100MHz repetition rate", *Appl. Phys. Lett.*, **67**(20): 2907-2909 (1995)

[73] D. H. Auston, K. P. Cheng, and P. R. Smith, "Picosecond photoconducting hertzian dipoles", *Appl. Phys. Lett.*, **45**: 284-286 (1984)

[74] D. H. Auston, and M. C. Nuss, "Electro-optic generation and detection of femtosecond electrical transients", *IEEE J. Quan. Elec.*, **24**: 184-197 (1988)

[75] D. R. Grischkowsky, "Nonlinear generation of sub-psec pulses of THz electromagnetic radiation by optoelectronics – Application to time-domain spectroscopy", *Frontiers in Nonlinear Optics*, IOP Philadelphia (1993)

[76] W.M.Robertson, *Optoelectronic Techniques for Microwave and Millimeter Engineering*, Artech House Boston (1995)

[77] G. Mourou, C. V. Stancampiano, A. Antonetti, "Picosecond microwave pulses generated with a subpicosecond laser-driven semiconductor switch", *Appl. Phys. Lett.*, **39**: 295-297 (1981)

[78] G. Mourou, C. V. Stancampiano, D. Blumenthal, "Picosecond microwave pulse generation", *Appl. Phys. Lett.*, **38**: 470-472 (1981)

[79] J. T. Darrow, B. B. Hu, X.-C. Zhang, D. H. Auston, "Subpicosecond electromagnetic pulses from large-aperture photoconducting antennas", *Opt. Lett.*, **15**: 323 (1990)

[80] L. Xu, X.-C. Zhang, D. H. Auston, B. Jalali, "Terahertz radiation from large-aperture Si p-i-n diodes", *Appl. Phys. Lett.*, **59**: 3357 (1991)

[81] D. You, R. R. Jones, P. H. Bucksbaum, D. R. Dykaar: "Generation of high-power sub-single-cycle 500-fs electromagnetic pulses", *Opt. Lett.*, **18**: 290 (1993)

[82] B. B. Hu, J. T. Darrow, X.-C. Zhang, D. H. Auston, P. R. Smith, "Optically steerable photoconducting antennas", *Appl. Phys. Lett.*, **56**: 886 (1990)

[83] B. I. Greene, P. N. Saeta, D. R. Dykaar, S. Schmittrink, S. L. Chuang, "Far-infrared light generation at semiconductor surfaces and its spectroscopic application", *IEEE J. Quantum Electron.* **28**: 2302 (1992)

[84] A. J. Taylor, P. K. Benicewicz, S. M. Young, "Modeling of femtosecond electromagnetic pulses from large-aperture photoconductors", *Opt. Lett.*, **18**: 1340 (1993)

[85] H. Roskos, M. C. Nuss, K. W. Gossen, D. W. Kisker, A. E. White, K. T. Short, D. C. Jacobson, J. M. Poate, "Propagation of picosecond electrical pulses on a slilicon-based microstrip line with buried cobalt silicide ground plane", *Appl. Phys. Lett.*, **58**: 2604 (1996)

[86] P. Uhd Jepsen, R. H. Jacobsen, S. R. Keiding, "Generation and detection of terahertz pulses from biased semiconductor antennas", *J. Opt. Soc. Am. B*, **13**: 2424 (1996)

[87] N. Fröberg, M. Mack, B. B. Hu, X.-C. Zhang, D. H. Auston, "500GHz electrically steerable photoconducting antenna-array", *Appl. Phys. Lett.*, **58**: 446 (1991)

[88] P. K. Benicewicz, A. J. Taylor, "Scaling of terahertz radiation from large-aperture biased InP photoconductors", *Opt. Lett.*, **18**: 1332 (1993)

[89] J. T. Darrow, X.-C. Zhang, J. D. Morse, "Saturation properties of large-aperture biased InP photoconductors", *IEEE J. Quantum Electron.*, **28**: 1607 (1992)

[90] J. T. Darrow, X.-C. Zhang, D. H. Auston, "Power scaling of large aperture photoconducting antennas", *Appl. Phys. Lett.*, **58**: 25 (1991)

[91] P. K. Benicewicz, J. P. Roberts, A. J. Taylor, "Scaling of terahertz radiation from large-aperture biased photoconductors", *J. Opt. Soc. Am. B*, **11**: 2533 (1994)

[92] A. V. Kuznetsov, C. J. Standon, "Ultrafast optical generation of carriers in a dc electric-field : Transient localization and photocurrent", *Phys. Rev. B*, **48**: 10828 (1993)

[93] C. W. Siders, J. L. W. Siders, A. J. Taylor, S. G. Park, M. R. Melloch, A. M. Weiner, "Generation and characterization of terahertz pulse trains from biased, large-aperture photoconductors", *Opt. Lett.*, **24**: 241 (1999)

[94] S. B. Lang, "Pyroelectricity: from ancient curiosity to modern imaging tool", *Phys. Today*, **58**: 31-36 (2005)

[95] T. L. Hwang S. E. Schwarz, and D. R. Rutledge, "Microbolometers for infrared detection", *Appl. Phys. Lett.*, **34**: 11 (1979)

[96] M. J. Griffin and W. S. Holland, "The influence of background poqer on the performance of an ideal bolometer", *Int. J. Infra. Milli. Wave.* **9**(10): 861-875 (1988)

[97] P. L. Richards, "Bolometers for infrared and millimeter waves", *J. Appl. Phys.*, **76**(1): 1-24 (1994)

[98] H. Kraus, "Superconductive bolometers and calorimeters", *Supercond. Sci. Technol.*, **9** : 827-842 (1996)

[99] Q. Wu and X.-C. Zhang, "Ultrafast electro-optic field sensors", *Appl. Phys. Lett.*, **68** (12): 1604 (1996)

[100] Q. Wu and X.-C. Zhang, "Free-space electro-optic sampling of terahertz beams", *Appl. Phys. Lett.*, **67**: 3525 (1995)

[101] Z. G. Lu, P. Campbell, and X.-C. Zhang, "Free-space electro-optic sampling with a high-repetition-rate regenerative amplified laser", *Appl. Phys. Lett.*, **71**: 593 (1997)

[102] Sang-Gyu Park, M. R. Melloch, and A. M. Weiner, "Comparison of terahertz waveforms measured by electro-optic and photoconductive sampling", *Appl. Phys. Lett.*, **73**(22): 3184-3186 (1998)

[103] Zhiping Jiang, F. G. Sun, and Q. Chen, and X.-C. Zhang, "Electro-optic sampling near zero optical transmission point", *Appl. Phys. Lett.*, **74**(9): 1141-1143 (1999)

[104] Q. Wu, M. Litz, and X.-C. Zhang, "Broadband detection capability of ZnTe electro-optic field detectors", *Appl. Phys. Lett.*, **68** (21): 2924-2926 (1996)

[105] J. F. Holzman, F. E. Vermeulen, S. E. Irvine, and A. Y. Elezzabi, "Free-space detection of terahertz radiation using crystalline and polycrystalline ZnSe electro-optic sensors", *Appl. Phys. Lett.*, **81**(20): 2294-2296 (2002)

[106] D. Grischkowsky, S. Keiding, M. van Exter, C. Fattinger, "Far-infrared time-domain spectroscopy with terahertz beams of dielectrics and semiconductors", *J. Opt. Soc. Am. B*, **7**: 2006 (1990)

[107] W. M. Robertson, G. Arjavalingam, S. L. Shinde, "Microwave dielectric measurements of zirconia-alumina ceramic composites – A test of the Clausius-Mossiti mixture equations", *J. Appl. Phys.*, **70**: 7648 (1991)

[108] K. Katzenellenbogen, D. Grischkowsky, "Electrical characterization to 4 THz of N- and P-type GaAs using THz time-domain spectroscopy", *Appl. Phys. Lett.*, **61**: 840 (1992)

[109] M. Schall, H. Helm, S. R. Keiding, "Far infrared properties of electro-optic crystals measured by THz-TDS", *Int. J. Infrared Millimeter Wave*, **20**: 595 (1999)

[110] Minwoo Yi, Kang Hee Lee, Inhee Maeng, Joo-Hiuk Son, R. D. Averitt, and Jaewook Ahn, "Tailoring the Spectra of Terahertz Emission from CdTe and ZnTe Electro-Optic Crystals", *Jpn. J. Appl. Phys.* **47**: 202-204 (2008)

[111] D. Mittleman editor, *Sensing with TeraHertz Radiation*, Springer, Berlin (2003).

[112] G. Hernandez, *Fabry-Perot Interferometers*, Cambridge University Press (1986)

[113] http://spec.jpl.nasa.gov/ftp/pub/catalog/c018005.cat.

[114] R. A.Akhmedzhanov, A. I.Korytin, A. G. Litvak,nA. M. Sergeev, and E.V. Suvorov, "Generation and detection of untrashort pulse of electromagnetic field in the THz range and their application for spectroscopy", *Radiophysics and Quantum Electronics*, **48**: 837-843 (2005)

[115] G. Gallot, J. Zhang, R. W. McGowan, T.-I. Jeon, and D. Grischkowsky, "Measurements of the THz absorption and dispersion of ZnTe and their relevance to the electro-optic detection of THz radiation", *Appl. Phys. Lett.*, **74**: 3450-3452 (1999)

[116] Q. Chen, M. Tani, Z.-P. Jang and X.-C. Zhang, "Electro-optic transceivers for terahertz-wave applications", *J. Opt. Soc. Am. B*, **18**: 823 (2001)

[117] P.Y. Yu and M. Cardona, *Fundamentals of Semiconductors* Springer-Verlag, Berlin, (1999).

[118] J.Z. Xu and X.-C. Zhang, "Optical rectification in an area with a diameter comparable to or smaller than the center wavelength of terahertz radiation", *Opt. Lett.* **27**: 1067 (2002)

[119] D.C. Hutchings and B.S. Wherrett, "Azimuthal dependence of two photon absorption coefficient in an isotropic crystal", *J. Opt. Mod.* **41**: 1141 (1994)

[120] A.A. Said, M. Sheik-Bahae, D.J. Hagan, T.H. Wei, J. Wang, J. Young and E.W. Van Stryland, "Determination of bound-electronic and free-carrier nonlinearities in ZnSe, GaAs, CdTe, and ZnTe", *J. Opt. Soc. Am. B* **9**: 405 (1992)

[121] W.-Q. He, C.-M. Gu and W.-Z. Shen, "Direct evidence of Kerr-like nonlinearity by femtosecond Z-scan technique", *Opt. Express.* **14**: 5476 (2006)

[122] G. Dakovski, B. Kubera and J. Shan, "Localized terahertz generation via optical rectification in ZnTe", *J. Opt. Soc. Am. B* **22:** 1667 (2005)

[123] V.Y. Gaivoronskii, M.M. Nazarov, D.A. Spapozhnikov, E.V. Shepelyavyi, S.A. Shkel'nyuk, A.P. Shkurinov and A.V. Shuvaev, "Competition between linear and nonlinear processes during generation of pulsed terahertz radiation in a ZnTe crystal", *Quant. Electron.*, **35**: 407 (2005)

[124] F.G. Sun, X.-C. Zhang, in *Conference on Lasers and Electro-Optics (CLEO)*, OSA Technical Digest (Washington DC 2000) p. 479.

[125] Tze-An Liu, M. Tani and C.-L. Pan, "THz radiation emission properties of multienergy arsenic-ion-implanted GaAs and semi-insulating GaAs based photoconductive antennas", *J. Appl. Phys.*, **93**: 2996 (2003)

[126] P. Uhd Jepsen, R. H. Jacobsen, and S. R. Keiding, "Generation and detection of terahertz pulses from biased semiconductor antennas", *J. Opt. Soc. Am. B*, **13**: 2424 (1996)

[127] G.Rodriguez and A.J.Taylor, “Screening of the bias field in terahertz generation from photoconductors”, *Opt. Lett.*, **21**: 1046 (1996)

[128] C. W. Siders, J. L. W. Siders, A. J. Taylor, S.-G. Park, M. R. Melloch, and A. M. Weiner, “Screening of the bias field in terahertz generation from photoconductors”, *Opt. Lett.*, **24**: 241 (1998)

[129] T. Dekoysky, T. Pferfier, W. Kutt, H. Kurz, “Subpicosecond carrier transport in GaAs surface-space-charge fields”, *Phys. Rev. B*, **58**: 4553 (1998)

[130] G. E. Stillman, C. M. Waife, and J. O. Dimmock, “Hall coefficient factor for. mode scattering in n-type GaAs” *J. Phys. Chem. Solids*, **31**: 1199-1204 (1970)

[131] J. Sjakste, V. Tyuterev, and N, Vast, “Intervalley scattering in GaAs: ab initio calculation of the effective parameters for Monte Carlo simulations” *Appl. Phys. A* **86**: 301–307 (2007)

[132] J. S.Blakemore, “Semiconducting and other major properties of gallium arsenide”, *J. Appl. Phys.* **53**: R123-R181 (1982)

[133] J. Faist, M. Beck, T. Allen, M. Rochat, and S. Blaser, “”, *IEEE J. Quant. Electron.*, **38**: 533 (2001)

[134] G. Scalari, L. Ajili, J. Faist, H. Beere, E. Linfield, D. Ritchie, and A. G. Davis, “”, *Appl. Phys. Lett.*, **82**: 3165 (2003).

[135] M. Woerner, K. Reimann, and T. Elsaesser, “Coherent charge transport in semiconductor quantufm cascade structure”, *J. Phys.: Condens. Matter.*, **16**: R25-R48 (2004)

[136] C Gmachl, F Capasso, D L Sivco, A. Y. Cho, “Recent progress in quantum cascade lasers and application”, *Rep. Prog. Phys.*, **64**: 1533-1601 (2001)

[137] G. Zhao, R. N. Schouten, N. van der Valk, W. Th. Wenckebach and P. C. M. Planken, “Design and performance of a THz emission and detection setup based on a semi-insulating GaAs emitter”, *Rev. Sci. Instrum*. **73**: 1715 (2002).

[138] J. Alton, S. S. Dhillon, A. de Rossi, M. Calligaro, H. E. Beere, S. Barbieri, E. H. Linfield, D. A. Ritchie and C. Sirtori, “Buried waveguides in THz quantum cascade

lasers based on two-dimensional surface plasmon modes", *Appl. Phys. Lett*. **86**: 071109 (2005).

[139] C. Worrall, J. Alton, M. Houghton, S. Barbieri, H. E. Beere, D. Ritchie and C. Sirtori, "Continuous wave operation of a superlattice quantum cascade laser at 2THz", *Opt. Express*. **14**: 171 (2006).

[140] R. Colombelli, F. Capasso, C. Gmachl, A. Tredicucci, A.M. Sergent, A.L. Hutchinson, D.L. Sivco, and A.Y. Cho "Intersubband electroluminescence from long-sided-cleaved quantum-cascade lasers above threshold: Investigation of phonon bottleneck effects" *Appl. Phys. Lett*. **77**: 3893 (2000).

[141] A. J. Bennett, R. D. Clayton, and J. M. Xu, "Above-threshold longitudinal profiling of carrier nonpinning and spatial modulation in asymmetric cavity lasers", *J. Appl. Phys.* **83**: 3784 (1998).

[142] R. Köhler, A. Tredicucci, F. Beltram, H. E. Beere, E. H. Linfield, A. G. Davies, D. A. Ritchie, R. Iotti, and F. Rossi, "Terahertz semiconductor-heterostructure laser", *Nature* **417**: 156 (2002)

[143] J. Alton, S. Barberie, H. E. Beere, J. Fowler, E. H. Linfield, D. A. Ritchie, "Low-threshold superlattice quantum cascade laser emitting at $\lambda = 103$ μm and operating up to 70 K in continuous wave", *Proc. SPIE.* **5354**: 129 (2004)

[144] C. Sirtori, F. Capasso, J. Faist, A. L. Hutchinson, D. L. Sivco, and A. Y. Cho, "Resonant tunneling in quantum cascade lasers", *IEEE J. Quantum Electron.* **34**: 1722 (1998)

[145] D. Indjin, P. Harrison, R. W. Kelsall, and Z. Ikonic, "Mechanisms of temperature performance degradation in terahertz quantum-cascade lasers", *Appl. Phys. Lett.*, **82**: 1347 (2003)

[146] K. Hirakawa, M. Grayson, D. C. Tsui, and C. Kurdak, "Blackbody radiation from hot two-dimensional electrons in AlxGa1-xAs/GaAs heterojunctions", *Phys. Rev. B*, **47**: 16651(R) (1993)

[147] M. Dür, S. Goodnick, and P. Lugli, "Monte Carlo simulation of intersubband relaxation in wide, uniformly doped GaAs/AlxGa1-xAs quantum wells", *Phys. Rev. B*, **54**: 17794 (1996)

[148] P. Harrison, D. Indjin, and R. W. Kelsall, "Electron temperature and mechanisms of hot carrier generation in quantum cascade lasers", *J. Appl. Phys.*, **92**: 6921 (2001)

[149] A. J. Bennett, R. D. Clayton, and J. M. Xu, "Above-threshold longitudinal profiling of carrier nonpinning and spatial modulation in asymmetric cavity lasers", *J. Appl. Phys.*, **83**: 3784 (1998).

[150] F. Rinner, J. Rogg, P. Friedmann, M. Mikulla, G. Weimann, and R. Poprawe, "Longitudinal carrier density measurement of high power broad area laser diodes" *Appl. Phys. Lett*. **80**: 19 (2002).

[151] M. -S. Nomura, F. Salleras, M. A. Dupertuis, L. Kappei, D. Marti, B. Deveaud, J.-Y. Emery, A. Crottini, B. Dagens, T. Shimura and K. Kuroda, "Density clamping and longitudinal spatial hole burning in a gain-clamped semiconductor optical amplifier", *Appl. Phys. Lett.* **81**, 2692 (2002).

[152] M. Rochat, J. Faist, M. Beck and U. Oesterle, "Electrically pumped Terahertz quantum well sources", *Physica E* **7**: 44 (2000).

[153] J. Kröll, J. Darmo, K. Unterrainer, S. S. Dhillon, C. Sirtori, X. Marcadet, and M. Calligaro, "Longitudinal spatial hole burning in terahertz quantum cascade lasers", *Appl. Phys. Lett.* Accepted for publication.

[155] J. Lin, W. Huang, Z. Sun, C. S. Ray, D. E. Day, "Structure and nonlinear optical performance of TeO_2-Nb_2O_5-ZnO glasses", *J. Non-Cryst. Sol.* **336**: 193-197 (2004)

[156] M. Sheik-Bahae, A. A. Said, and E. W. Van Stryland, "High-sensitivity, single-beam n_2 measurements," *Opt. Lett.*, **14**: 955-957 (1989)

[157] H. Vogelsang, O. Husberg, U. Köhler, W. von der Osten, "Exciton self-trapping in AgCl nanocrystalss", *Phys. Rev. B* **61**: 1847-1852 (2000)

[158] S. Lettieri, P. Maddalena, "Nonresonant Kerr effect in microporous silicon: Nonbulk dispersive behavior of below band gap $\chi^{(3)}$", *J. Appl. Phys.* **91**: 5564-5570 (2002)

[159] F. Urbach, “The long-wavelength edge of photographic sensitivity and of electronic absorption of solids”, *Phys. Rev.* **92**: 1324 (1953)

Appendix A

Generally, the nonlinear polarizability can be expressed with susceptibility and Taylor series term of planar electromagnetic field E (t)

$$P = \varepsilon_0 \chi^{(1)} E(t) + \varepsilon_0 \chi^{(2)} E(t)^2 + \varepsilon_0 \chi^{(3)} E(t)^3 + \cdots\cdots = P_L + P_{NL}, \qquad (A.1)$$

where ε_0 is the vacuum permittivity, χ is the dielectric tensor. The first term corresponds to the linear polarizability and the other terms correspond to the nonlinear polarizability. The order of χ represents the order of the nonlinear effect. In order to separate different nonlinear optical effect, the temporal variable t of above equation has to be replaced by frequency variable ω with Fourier transformation

$$E(z,t) = \int_{-\infty}^{+\infty} E(z,t) \cdot e^{i\omega t} d\omega = \int_{-\infty}^{+\infty} E_0 e^{-(\omega-\omega_0)^2 \tau_p^2} \cdot e^{i(\omega t - k(\omega) z)} d\omega, \qquad (A.2)$$

where the ω_0 is its central frequency and τ_p is the pulse duration. Thus, Gaussian beam pulse configuration can be expressed in a time dependent function as follows:

$$E(z,t) = A(z,t) \cdot e^{i(\omega_0 t - k\omega_0 z)}, \qquad (A.3)$$

with

$$A(z,t) = A_0 \cdot e^{-\frac{\left(t - \frac{z}{v_g}\right)^2}{4\tau_p^2}}, \qquad (A.4)$$

where $A(z,t)$ is the Gaussian enveloppe of ultrashort pulse duration. In order to reveal the electromagnetic emission induced by the optical rectification, Maxwell equations can helps us understand the interaction between ultrashort pulse and nonlinear crystals which generate THz radiation. Taking into account the 3 dimension spatial reference $r = \sqrt{x^2 + y^2 + z^2}$, the Maxwell equations are as follows:

$$\nabla \times E(r,t) + \mu_0 \frac{\partial H(r,t)}{\partial t} = 0, \qquad (A.5)$$

$$\nabla \times H(r,t) = j(r,t) + \frac{\partial D(r,t)}{\partial t}, \qquad (A.6)$$

$$\nabla P = 0, \qquad (A.7)$$

$$\nabla D = \rho = 0\,, \tag{A.8}$$

We suppose that the free charge ρ is zero so that the electric field and displacement vector can be written in:

$$\left[\nabla\times\left(\nabla\times E\right)+\frac{1}{c^2}\frac{\partial^2}{\partial t^2}\varepsilon\cdot E\right]=-\frac{4\pi}{c^2}\frac{\partial^2}{\partial t^2}P^{(2)}\left(r,t\right), \tag{A.9}$$

Taking into account $D=\varepsilon_0 E+P$, it can be simplified to

$$\Delta E\left(r,t\right)=\mu_0\frac{\partial^2 D\left(r,t\right)}{\partial t^2}, \tag{A.10}$$

Here, we transfer the spatial variable to the frequency space by Fourier transformation and get

$$\Delta\int_{-\infty}^{+\infty}E\left(r,\omega\right)\cdot e^{i\omega t}d\omega=\mu_0\frac{\partial^2}{\partial t^2}\int_{-\infty}^{+\infty}D\left(r,\omega\right)\cdot e^{i\omega t}d\omega\,, \tag{A.11}$$

The integral operator counteract the deviate operator and it can be express as

$$\Delta E\left(r,\omega\right)=-\omega^2\mu_0 D\left(r,\omega\right), \tag{A.12}$$

then taking account into the nonlinear polarizability $P=P_L+P_{NL}$ we have

$$D\left(r,\omega\right)=\varepsilon_0 E\left(r,\omega\right)+\varepsilon_0\chi^{(1)}E\left(r,\omega\right)+P_{NL}=\varepsilon_0\left(1+\chi^{(1)}\left(\omega\right)\right)E\left(r,\omega\right)+P_{NL}\left(r,\omega\right), \tag{A.13}$$

Therefore, the equation can be written with linear and nonlinear polarizability

$$\Delta E\left(r,\omega\right)+\frac{\varepsilon\left(\omega\right)\omega^2}{c^2}E\left(r,\omega\right)=-\mu_0\omega^2 P_{NL}\left(r,\omega\right), \tag{A.14}$$

The electromagnetic radiation has been represented with nonlinear polarization. From above equation, one can understand the process that Gaussian beam pulse generates electromagnetic radiation. Consider the equation1.1, the second order nonlinear polarization dominate the P_{NL} in an anti-centrosymmetric crystals due to the $\chi^{(2)}$ is not zero. However, the second order nonlinear polarization give arise to a frequency-sum and frequency-difference effect which is expressed as

$$P^{(2)}\left(z,t\right)=\varepsilon_0\frac{\chi^{(2)}\left(0;\omega,-\omega\right)A\left(z,t\right)^2}{2}+\varepsilon_0\frac{\chi^{(2)}\left(2\omega;\omega,-\omega\right)A\left(z,t\right)^2}{2}e^{(2i\omega_0 t)}, \tag{A.15}$$

In equation1.15 the first term represent the optical rectification (OR) and the second term represent the second harmonic generation (SHG). Now, one can consider the a Gaussian pulse propagate in z direction and its OR polarization can be given as

$$P_{OR}^{(2)}(z,t)=\frac{1}{2}\varepsilon_0\chi^{(2)}(0;\omega,-\omega)A_0^2\cdot e^{-\frac{\left(t-\frac{z}{v_g}\right)^2}{2\tau_p^2}}=P_0\cdot e^{-\frac{\left(t-\frac{z}{v_g}\right)^2}{2\tau_p^2}}, \tag{A.16}$$

Then the different spectral components of ultrashort pulse has to be expressed and this equation can be written in

$$P_{OR}^{(2)}(z,\omega)=\frac{P_0\tau_p}{\sqrt{2\pi}}\cdot e^{-\frac{\omega^2\tau_p^2}{2}}e^{-i\omega\frac{z}{v_g}}, \tag{A.17}$$

Thus the right term of equation1.15 can be deduced into

$$-\mu_0\omega^2P_{NL}(z,\omega)=-\mu_0\omega^2\frac{P_0\tau_p}{\sqrt{2\pi}}\cdot e^{-\frac{\omega^2\tau_p^2}{2}}e^{-i\omega\frac{z}{v_g}}=a_0\omega^2\tau_p\cdot e^{-\frac{\omega^2\tau_p^2}{2}}e^{-i\omega\frac{z}{v_g}}, \tag{A.18}$$

This is the simplified expression of THz radiation and its amplitude can be exacted

$$a(\omega)=a_0\omega^2\tau_p e^{-\frac{\omega^2\tau_p^2}{2}}, \tag{A.19}$$

From above two equations, one can find some important properties of THz radiation by optical rectification:

The output THz radiation is proportional to the incident beam mean power. A ultrashort pulse duration corresponds to a broadband frequency component, which can broad the THz bandwidth. THz amplitude is proportional to the laser frequency. In fact, there is another important point take impact on the propagation of THz beam that is the THz propagation velocity in z direction is equal to the pump laser beam, which is called phase matching condition. It can be deduced by equation 1.15 at one dimension z:

$$\Delta E(z,\omega)+\frac{\varepsilon(\omega)\omega^2}{c^2}E(z,\omega)=a(\omega)e^{-i\omega\frac{z}{v_g}}, \tag{A.20}$$

The electric field E(z,ω) propagates by the z axis can be written as

$$E(z,\omega) = E_{THz}(z,\omega)e^{-i\omega\frac{z\cdot n(\omega)}{c}}, \tag{A.21}$$

Taking into account of the slow variable approximation $\left(\frac{d^2E_{THz}}{dz^2} \langle\langle k(\omega)\frac{dE_{THz}}{dz}\right)$, one can get

$$-2ik(\omega)\frac{\partial E_{THz}(z,\omega)}{\partial z} = a(\omega)e^{i\omega z\left(\frac{n(\omega)}{c}-\frac{1}{v_g}\right)}, \tag{A.22}$$

Thus, suppose that the pump beam energy dispersion in the nonlinear crystal approaching to zero, one can integrate the above equation and deduce the output THz amplitude:

$$E_{THz}(L,\omega) = \frac{ia(\omega)}{2k}L.\sin c\left(\frac{\omega}{2c}\left[n(\omega)-n_g\right]L\right), \tag{A.23}$$

where the L is the thickness of crystal. Only in the condition $n(\omega) = n_g$ that the THz pulse phase velocity is the same as pump beam group velocity, THz field reaches maximum.

Appendix B

According to the Maxwell's equations, the material response is a function of conductivity tensor. For a material with a linear response to the driving electric field and time-invariant properties, this relation is particularly simple in the frequency domain where the Fourier transforms of he current density j(ω) and the driving electric field $E_b(\omega)$ are related by the conductivity tensor σ(ω) as

$$\vec{j}(\omega) = \vec{\sigma}(\omega)\vec{E}_b(\omega), \tag{B.1}$$

In the time domain, the equivalent expression is

$$\vec{j}(\omega) = \int \vec{\sigma}(t-t')\vec{E}_b(t')dt', \tag{B.2}$$

where the time-domain response,

$$\vec{\sigma}(t) = \frac{1}{2\pi}\int_{-\infty}^{\infty} \vec{\sigma}(\omega)e^{-i\omega t}d\omega, \tag{B.3}$$

σ(t) is the inverse Fourier transform of the frequency-domain conductivity σ(ω).

This formulation of the material response in terms of a conductivity tensor has the advantage of permitting one to incorporate the finite carrier response time that is clearly relevant for the subpicosecond transient currents involved in the production of THz radiation. However, theabove description is still incomplete. It must be modified to account for the critical time-dependent change in the material properties induced by the pump excitation. Therefore, the expression of conductivity can be changed from frequency variation to time term by

$$\vec{\sigma}(t) = \vec{\sigma}_{dc}\delta(t), \tag{B.4}$$

where, $\sigma_{dc}=\sigma(\omega=0)$ is the usual dc conductivity of material. If the response is dominated by the motion of electrons of charge e, the dc conductivity can be written as

$$\vec{\sigma}_{dc} = e\vec{\mu}_{dc}N(t), \tag{B.5}$$

where μ_{dc} is the dc mobility of electrons and N(t) is the time-varying carrier density. This relation could be modified to incorporate a parametric time dependence for the mobility itself and it is also a description of density-dependent changes in the carrier-scattering rate. The

expression could also be modified to include a contribution from hole transport. The electron contribution generally is considerably larger than that of the holes because of the much higher electron mobility. Thus, the hole contribution to transient current is out of explicity in this chapter. Corresponding to the instantaneous response of carriers, the time dependence of current density can then be expressed as

$$j(t) = e\tilde{\mu}_{dc} N(t) E_b(t), \tag{B.6}$$

It can be modeled that the photocurrent density at time t resulting from carrier injection at time t_0 as the product of carrier density still persisting at the later time t multiplied by the drift velocity of carriers at that time. Thus, contribution to current desnsity at time t from carriers generated in a unit time interval at time t_0 can be written as:

$$j(t, t_0) = eN(t, t_0) v_{t_0}(t), \tag{B.7}$$

Here the carrier density at time t from generation at time t_0, denoted by $N(t,t_0)$, is given by the initial contribution multiplied by a function $R_c(t-t_0)$, describing the decay of the number of photo-generated carriers with time. Introducing a factor A to account for the conversion from incident laser intensity to the rate of electron-hole pair generation in the photoconductor, we can express the carrier density as

$$N(t, t_0) = AR_c(t - t_0) I_0, \tag{B.8}$$

where I_0 is the laser irradiance.

The carrier drift velocity (in the linear-response regime) can be described by a frequency-domain mobility as $\nu(\omega)=\bar{U}(\omega)E_b(\omega)$. The corresponding expression in the time domain can be stated in terms of the time-domain mobility response function as

$$v_{t_0}(t) = \int_{t_0}^{t} \mu(t - t') E_b(t') dt', \tag{B.9}$$

with the initial condition given at time t0 of $\nu(t=t_0)=0$. Thus, the photocurrent density resulting from instantaneous injection of carriers at time t_0 becomes

$$j(t, t_0) = eN(t, t_0) \int_{t_0}^{t} \mu(t - t') E_b(t') dt', \tag{B.10}$$

Appendix C

The electric displacement vector of ZnTe crystal is $\vec{D} = \varepsilon_0 \varepsilon_r \vec{E}$. Due to the crystallographic symmetry, the relative permittivity tensor is diagonal

$$\varepsilon_r = \begin{bmatrix} n_x^2 & 0 & 0 \\ 0 & n_y^2 & 0 \\ 0 & 0 & n_z^2 \end{bmatrix}, \tag{C.1}$$

Therefore, we deduced that the composant of tensor alone the xyz axis is $D_i = \varepsilon_0 n_i^2 E_i$. For the non-diagonal elements, the tensor is $[\varepsilon_r]_{ij} = [\varepsilon_r]_{ji}$ so that $D_i = \varepsilon_0 \sum_j n_{ij}^2 E_i$ From Maxwell equations:

$$\vec{\nabla} \times \vec{H} = \frac{\partial \vec{D}}{\partial t} \Leftrightarrow \vec{k} \times \frac{\vec{B}}{\mu_0} = -\omega \vec{D}, \tag{C.2}$$

$$\vec{\nabla} \times \vec{E} = \frac{\partial \vec{B}}{\partial t} \Leftrightarrow \vec{k} \times \vec{E} = \omega \vec{B}, \tag{C.3}$$

$$\vec{\nabla} \cdot \vec{B} = 0 \Leftrightarrow \vec{k} \cdot \vec{B} = 0, \tag{C.4}$$

$$\vec{\nabla} \cdot \vec{D} = 0 \Leftrightarrow \vec{k} \cdot \vec{D} = 0 \tag{C.5}$$

One cam deduced that $\vec{D}: D_i = \varepsilon_0 n^2 \left(E_i - \left(\vec{\mu} \cdot \vec{E} \right) \mu_i \right)$. The electric field component can be written in $E_i = \frac{1}{\varepsilon_0} \sum_j \left(\frac{1}{n^2} \right)_{ij} D_j$ According to the gradient of electric vector equation, there is the relation:

$$\frac{x^2}{n_x^2} + \frac{y^2}{n_y^2} + \frac{z^2}{n_z^2} + \frac{2xy}{n_{xy}^2} + \frac{2yz}{n_{yz}^2} + \frac{2zx}{n_{zx}^2} = 1, \tag{C.6}$$

This is called refractive index ellipsoid.

In the case of [110] ZnTe crystal, when an arbitary bias electric fields $E = E\left(E_x, E_y, E_z\right)$ is applied to the crystal, the equation of the crystal refractive index ellipsoid induced by the electric field can be written as

$$\frac{x^2+y^2+z^2}{n_0^2}+2r_{41}E_x yz+2r_{41}E_y zx+2r_{41}E_z xy=1, \tag{C.7}$$

In the FSEOS of THz beam, the bias field comes from the transient THz pulse radiation. When a THz beam is normally incident upon a [110] ZnTe, in the crystallographic axes, its E field can be written as

$$E_{THz}=E_{THz}\left(\frac{\sin\phi}{\sqrt{2}},-\frac{\sin\phi}{\sqrt{2}},\cos\phi\right), \tag{C.8}$$

The equation of the index ellipsoid becomes

$$\frac{x^2+y^2+z^2}{n_0^2}+\frac{2r_{41}E_{THz}\sin\phi}{\sqrt{2}}yz-\frac{2r_{41}E_{THz}\sin\phi}{\sqrt{2}}zx+2r_{41}E_{THz}\cos\phi xy=1, \tag{C.9}$$

By the use of equation 1.42 the above equation is expressed in the lab coordinate system x'y'z' as

$$\frac{x'^2+y'^2+z'^2}{n_0^2}+2r_{41}E_{THz}\sin\phi y'z'+r_{41}E_{THz}\cos\phi\left(x'^2-y'^2\right)=1, \tag{C.10}$$

The equation of the index ellipse on the [110] plane (y'z'plane) is obtained by setting x'=0:

$$\left(\frac{1}{n_0^2}-r_{41}E_{THz}\cos\phi\right)y'^2+\frac{z'^2}{n_0^2}+2r_{41}E_{THz}\sin\phi y'z'=1, \tag{C.11}$$

From the above equation one can derive the difference of the two principal refractive indexes of the ellipse and the orientation of the principal axes. We first find the eigenvalues by solving the following equation:

$$\det\begin{vmatrix}\frac{1}{n_0^2}-r_{41}E_{THz}\cos\phi-s & r_{41}E_{THz}\sin\phi\\ r_{41}E_{THz}\sin\phi & \frac{1}{n_0^2}-s\end{vmatrix}=0, \tag{C.12}$$

The roots of the above equation are

$$s_{1,2}=\frac{1}{n_0^2}+\frac{1}{2}r_{41}E_{THz}\left(\pm\sqrt{1+3\sin^2\phi}-\cos\phi\right), \tag{C.13}$$

$$\Delta n \equiv \left(n_{z''} - n_{y''}\right) = \frac{n_0^3 r_{41} E_{THz} \sqrt{1+3\sin^2\phi}}{2} \ , \tag{C.14}$$

At the outcome of ZnTe, Pockel's effect results in the the phase retardation $\Gamma = (2\pi d/\lambda)\Delta n$, so the optimum signal can be realized at the largest phase retardation with Φ=90°, in which the THz E field is parallel to the y" axis, the $[\pm 1, \mp 1, 1]$ direction of the crystal. When the phase retardation is largest withΦ=90°, the angle φ is equal to 45°, which means that one should set the polarization of the probe beam to be parallel to either y'$[\pm 1, \mp 1, 1]$ or z'$[\pm 1, \mp 1, 1]$ for optimized electro-optical sampling geometry. The phase retard

$$\Gamma = \frac{2\pi d}{\lambda} n_0^3 r_{14} E_{THz} \, , \tag{C.15}$$

Imagine the probe beam is linear polarized in xy-plane and it is normal incident on the ZnTe (z-direction) so that the above refractive ellipsoid is as follows:

$$\frac{E_x^2}{\frac{E_0^2}{2}(1+\cos\Gamma)} + \frac{E_y^2}{\frac{E_0^2}{2}(1-\cos\Gamma)} = 1 , \tag{C.16}$$

Therefore, one can deduce the probe beam pass through the ZnTe crystal without THz radiation, its s-polarization or p-polarization still the same because the phase retardation is 0.

Thus, let's pay attention to the polarization variation of transmitted probe beam pass through the λ/4 waveplate. Without THz radiation, the ZnTe crystal is isotropic. An arbitrary linear polarized transmitted probe beam E_0, its polarization component angle to x-axis is γ. So its Jone's matrix is

$$\vec{E}_0 = \begin{pmatrix} E_0 \cos\gamma \cos\omega t \\ -E_0 \sin\gamma \cos\omega t \end{pmatrix}, \tag{C.17}$$

Due to the subtle difference of ordinary and extraordinary optical axis (n_o=1.5442, n_e=1.5533), the dephasing ratio is π/2. The outcome beam is with the polarization:

$$\vec{E}_1 = \begin{pmatrix} E_0 \cos\gamma \cos\left(\omega t + \frac{\pi}{2}\right) \\ -E_0 \sin\gamma \cos\omega t \end{pmatrix} = \begin{pmatrix} -E_0 \cos\gamma \sin\omega t \\ -E_0 \cos\gamma \cos\omega t \end{pmatrix}, \tag{C.18}$$

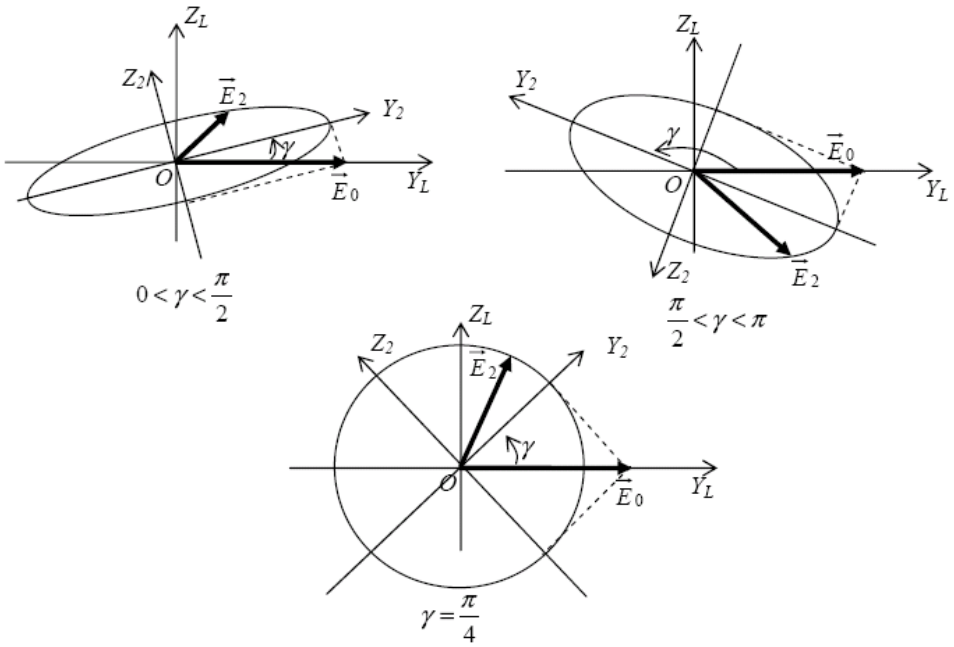

Fig. C.1 Diagram of THz beam pass through the λ/4 waveplate

We suppose the polarized transmitted beam is λ/4 to the x-axis and y-axis. So it is

$$\vec{E}_2 = \begin{pmatrix} \frac{\sqrt{2}}{2} E_0 \cos(\omega t + \delta) \\ \frac{\sqrt{2}}{2} E_0 \cos \omega t \end{pmatrix}, \tag{C.19}$$

The total phase retardation is $\delta=\Phi+\Gamma=\frac{2\pi d}{\lambda} n_0^3 r_{14} E_{THz}+\pi/2$. Thus the total refractive index ellipse equation can be written in

$$\frac{E_{2x}^2}{\frac{E_0^2}{2}(1+\cos\delta)} + \frac{E_{2y}^2}{\frac{E_0^2}{2}(1-\cos\delta)} = 1 \Leftrightarrow \frac{E_{2x}^2}{\frac{E_0^2}{2}(1-\sin\Gamma)} + \frac{E_{2y}^2}{\frac{E_0^2}{2}(1+\sin\Gamma)} = 1, \tag{C.20}$$

$$I_x = \left\langle E_{2x}^2 \right\rangle = \frac{E_0^2}{8}(1-2\sin\Gamma), \tag{C.21}$$

$$I_y = \left\langle E_{2y}^2 \right\rangle = \frac{E_0^2}{8}(1+2\sin\Gamma), \tag{C.22}$$

$$\Delta I = I_0 \sin\Gamma \approx I_0 \Gamma = \frac{2\pi d}{\lambda} n_0^3 r_{14} E_{THz} I_0, \tag{C.23}$$

Now, one can deduce the polarization equation of THz modulated probe beam passing through the Wollaston prism. Wollaston prism compose of 2 calcite triangle with perpendicular ordinary and extraordinary optical axis (n_o=1.6584, n_e=1.4864) its principal is showed in Fig. C.1.

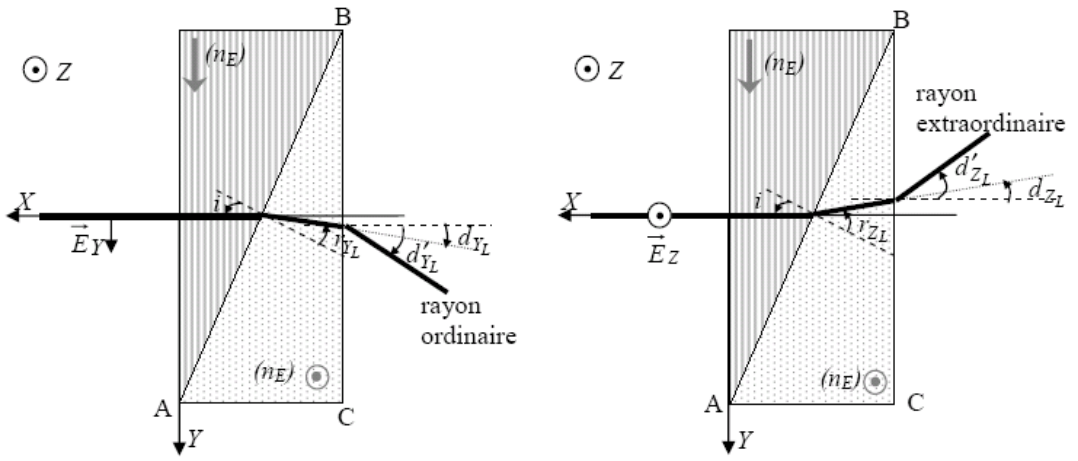

Fig. C.2 Diagram of Wollaston prism

The perpendicular polarized beam is separated by the different refractive index at the interface of two sub-prism. The angle of prism is θ0, the s-polarization component of beam is refracted by θ_1, $\theta_1 < \theta_0$ and $n_E \sin\theta_0 = n_O \sin\theta_1$, $\Delta\theta_x = \theta_1 - \theta_0$ the same as the p-polarization component $\theta_2 > \theta_0$ and $n_E \sin\theta_2 = n_O \sin\theta_0$, $\Delta\theta_y = \theta_2 - \theta_0$. So we have

$$\sin\Delta\theta_x = \sin\theta_0 \left(\frac{n_E}{n_O}\cos\theta_0 - \sqrt{1-\left(\frac{n_E}{n_O}\sin\theta_0\right)^2} \right) < 0, \tag{C.24}$$

$$\sin\Delta\theta_y = \sin\theta_0 \left(\frac{n_O}{n_E}\cos\theta_0 - \sqrt{1-\left(\frac{n_O}{n_E}\sin\theta_0\right)^2} \right) > 0, \tag{C.25}$$

Therefore, the separated angle of 2 perpendiculars polarized beam component:

$$\sin\theta'_x = n_O \sin\Delta\theta_x = \sin\Delta\theta_0 \left(n_E \cos\Delta\theta_0 - \sqrt{n_O^2 - n_E^2 \sin^2\Delta\theta_0} \right), \tag{C.26}$$

$$\sin\theta'_y = n_E \sin\Delta\theta_x = \sin\Delta\theta_0 \left(n_O \cos\Delta\theta_0 - \sqrt{n_E^2 - n_O^2 \sin^2\Delta\theta_0} \right), \tag{C.27}$$

Finally, the angle divergence is $D = \theta'_x - \theta'_y$

Appendix D

THz beam is a Gaussian beam, and it can be focused to a diffraction-limited spot size. It indicates that normal Gaussian beam formalism in optical system can be used to model the propagation of THz beams. Therefore, the method for measuring laser waist is still available for determining the THz focal diameter measurements. Knife-edge method is matured technique by which we can determine the waist of Gaussian beam easily.

The cross-sectional spatial profile of a Gaussian laser beam propagating in the z direction is given by the function

$$G_0 = E_0 \exp\left(-\frac{x^2+y^2}{\omega(z)^2}\right), \tag{D.1}$$

E_0 is the center electric amplitude of Gaussian beam, $\omega(z)$ is the radius at which G_0 fall to $\frac{1}{e}$ times (37%) its center amplitude. We suppose linear 1 dimension translation of knife-edge. If the x axis is chosen as a translation axis, the response of transmission energy is given by

$$T\left(x_b\right) = \int_{-\infty}^{+\infty} dy \int_{-\infty}^{x_0} dx G_0\left(x,y\right), \tag{D.2}$$

where x_0 is the x coordinate of the knife-edge when the measurement is made. Evaluation of Eq. yields

$$T\left(x_b\right) = E_0\omega(z)\pi^{-\frac{1}{2}} \int_{-\infty}^{x_0} dx \exp\left(-\frac{x^2}{\omega(z)^2}\right), \tag{D.3}$$

$$T\left(x_b\right) = E_0\omega(z)\pi^{-\frac{1}{2}} \left[\int_{-\infty}^{+\infty} dx \exp\left(-\frac{x^2}{\omega(z)^2}\right) + \int_{0}^{x_0} dx \exp\left(-\frac{x^2}{\omega(z)^2}\right)\right], \tag{D.4}$$

By the same evaluation we go further

$$T\left(x_b\right) = E_0\omega(z)\pi^{-\frac{1}{2}} \left[\frac{\omega\sqrt{\pi}}{2} + \int_{0}^{x_0} dx \exp\left(-\frac{x^2}{\omega(z)^2}\right)\right], \tag{D.5}$$

Here, we use the parameter transformation to make $t = \frac{x}{w}$

Then we get $dt = \frac{dx}{w}$ and $wdt = dx$

Next we use error function

$$erf\left(x\right) = \frac{2}{\sqrt{\pi}} \int_{0}^{x} dt \exp\left(-t^2\right), \tag{D.6}$$

So, the latter term of Eq. can be transformed into error function type

$$\int_0^{x_0} dx \exp\left(-\frac{x^2}{\omega(z)^2}\right) = \int_0^{\frac{x_0}{w}} w dt \exp\left(-t^2\right) = \frac{\omega\sqrt{\pi}}{2} erf\left(\frac{x_0}{w}\right), \tag{D.7}$$

Obviously, the transmission of Gaussian beam can be written as

$$T = \frac{E\omega^2\pi}{2}\left[1 + erf\left(\frac{x_0}{\omega}\right)\right], \tag{D.8}$$

Therefore, we can get the waist of Gaussian beam with deviate the transmission function.

Appendix E

Theory of DFWM

The diffraction of light from such a grating is closely related to the classical scattering of light from random fluctuations. The formation of transient gratings is the basis of real-time holography, phase conjugation and four wave mixing. In order to create a grating, two beams are arranged to interfere. Interference produces a spatially periodic light intensity and polarization distribution which changes the optical properties of a material placed into the interference region. The spatial modulation of the optical material constants acts as a diffraction grating. Light from a more-or-less powerful pump laser is split into two-beams A and B with wave vectors k_A and k_B, electric field amplitude A_A,A_B and intensity I_A,I_B. The two beams intersect at an angle θ at the sample and create an interference pattern, the grating vector *q* of which is

$$q = \pm(k_A - k_B), \tag{E.1}$$

The spatial period Λ is

$$\Lambda = 2\pi/q, \tag{E.2}$$

Where q=|q|. Λ can be expressed in terms of the pump wavelength λ_p and the angle θ

$$\Lambda = \lambda_p / 2\sin(\theta/2), \tag{E.3}$$

For small angles θ, the grating period is approximately

$$\Lambda \approx \lambda_{0p}/\theta_0 \text{ for } \theta_0 << 1, \tag{E.4}$$

By varying the intersection angle θ_0 the grating period Λ can be changed. The maximum value of Λ is limited by the diameter of the laser beam inducing the grating. Experimentally, values up to approsximately 100μm have been used. The smallest grating-period values are achieved when the two excitation beams are antiparallel with θ=180° giving a minimum value of $\Lambda=\lambda_p/2=\lambda_{0p}/2n$. Using a visible laser and highly refractive material, the grating period may be as small as 100nm.

Cartesian coordinates will be chosen throughout this volume such that the x- and z-axes are in the plane defined by k_A and k_B. For symmetry reasons, these vectors point into the directions of the two bisectrix between the pump beams as indicated in Fig.2.2b. The y-direction points upwards so as to produce a right-handed system. Thus the x-axis is parallel to q while the z-axis, for small θ_p, almost coincide with k_A and k_B, the propagation directions of pump beams. The cross-section of the interference pattern is confined to the *xy* plane being perpendicular to (k_A, k_B) and containing *q*.

k_A and k_B, and q can be expressed as

$$K_{A,B} = z_0 k_z \pm x_0 k_x , \tag{E.5}$$

$$q = \pm x_0 q = \pm x_0 2k_x , \tag{E.6}$$

Where x_0, z_0 (and y_0) denote the respective unit vectors.

The electric-field amplitude distribution inside the interference region is

$$A = A_A e^{ik_x x} + A_B e^{-ik_x x} , \tag{E.7}$$

and the total time-dependent field E(r,t) is given by

$$E(r,t) = \frac{A}{2} e^{i(k_z z - \omega_p t)} + c.c.. , \tag{E.8}$$

The intensity distribution is

$$I = \frac{n}{2}\varepsilon_0 cA \cdot A^* = \frac{n}{2}\varepsilon_0 c\left(|A_A|^2 + 2A_A A_B^* \cos 2k_x x + |A_B|^2\right) = I_A + 2\Delta I \cos 2k_x x + I_B , \tag{E.9}$$

Where $\Delta I = \frac{n}{2}\varepsilon_0 cA_A \cdot A_B^*$ is the intensity modulation amplitude and the asterisk denotes the complex conjugate (c.c.).

Appendix F

Under the assumption that the sample is 'thin' the optical field behind the sample can be calculated. We assume a Gaussian TEM_{00} beam. The electric field in front of the sample is then given by

$$E(z,r,t) = E_0(t)\frac{\omega_0}{\omega(z)}\exp\left\{-\frac{r^2}{\omega^2(z)} - \frac{ikr^2}{2R(z)}\right\}\exp(-i\phi(z,t)), \tag{F.1}$$

where $r^2 = x^2 + y^2$, z_0 the Rayleigh range $z_0^2 = \frac{\pi\omega_0^2}{\lambda}$, ω the beam radius,

$$\omega^2(z) = \omega_0^2\left(1 + \frac{z_0^2}{z^2}\right), \tag{F.2}$$

The assumption that the plate is thin means that the beam profile remains unchanged along the sample thickness L, which is equivalent to the condition $L<z_0$. The differential equations for the intensity and phase change are then given by

$$\frac{dI}{dz'} = -(\alpha + \beta I)I\,, \tag{F.3}$$

Solving these equations leads to the following field behind the sample:

$$E_e(z,r,t) = E(z,r,t)\frac{e^{-\alpha L/2}}{(1+q)^{1/2}}\exp\left\{i\frac{kn_2}{\beta}\ln(1+q)\right\} = E(z,r,t)e^{-\alpha l/2}(1+q)^{ikn_2/\beta - \frac{1}{2}}, \tag{F.4}$$

$$q(z,r,t) = I(z,r,t)\beta\frac{1-e^{-\alpha L}}{\alpha}, \tag{F.5}$$

Where α is the linear absorption coefficient, β is the two-photon absorption coefficient, n_2 is the nonlinear refractive index and $k = 2\pi/\lambda$. In practice, short pulses are needed to achieve the high intensities required to measure the nonlinearities.

Publication List

Journals:

1. Zhenyu Zhao, Sophie Hameau, and Jérôme Tignon, "THz Generation by Optical Rectification and Competition with Other Nonlinear Processes", *Chin. Phys. Lett.*, **25**:1868 (2008)
2. Nathan Jukam, Sukhdeep Dhillon, Zhenyu Zhao, Geog Duerr, Julien Armijo, Nathalian Sirmons, Sophie Hameau, Stephani Barbieri, Pascal Filloux, Carlo Sirtori, Xavier Marcadet and Jérôme Tignon, "Gain Measurements of THz Quantum Cascade Lasers using THz Time-Domain Spectroscopy", *IEEE Selected Topics J. of Quant. Electro.* **14**(2): 436-442 (2008)

Submitted:

3. N. Jukam, S. S. Dhillon, D. Oustinov, Z.-Y. Zhao, S. Hameau, J. Tignon, S. Barbieri, A.Vasanelli, P. Filloux, C. Sirtori, and X. Marcadet, "Investigation of spectral gain narrowing in quantum cascade lasers using terahertz time domain spectroscopy", *Applied Physics Letters* (Submitted)
4. Zhenyu Zhao, Sophie Hameau, and Jérôme Tignon, "Azimuthal dependence and competition between THz radiation induced by optical rectification and other nonlinear processes", *Physica B* (Submitted)
5. Zhenyu Zhao, Nathan Jukam, Sukhdeep Dhillon, Sophie Hameau, and Jérôme Tignon, "THz emission performance of SI-GaAs interdigitated photoconductive antenna", *Chin. Phys. Lett.*, (Submitted)
6. Zhenyu Zhao, Tianqing Jia, Jian Lin, Zhenrong Sun, and Zugeng Wang, "Femtosecond non-resonant optical nonlinearity of silver chloride nanocrystals doped niobic tellurite glass", *Physica. B* (Submitted)
7. Zhenyu Zhao, Tianqing Jia, Jian Lin, Zhenrong Sun, and Zugeng Wang, "Optical limiting induced by trapped state exciton of silver chloride nanocrystals doped niobic tellurite glass", *Chin. Sci. Bull.* (Submitted)

Conference Proceedings

1. Z.-Y. Zhao, S. Hameau, M. Voos, and J. Tignon, "THz generation by optical rectification and competition with other nonlinear processes", *17th International Symposium on Space Terahertz Technology (ISSTT)*, *Conference proceeding*, P2-14
2. Z.-Y. Zhao, S. Hameau, and J. Tignon, "THz generation by optical rectification and competition with other nonlinear processes", *28th International conference on Physics of Semiconductors (ICPS)*, *AIP Conference Proceeding*, **896**: 503-504 (2007)
3. N. Jukam, S. Dhillon, D. Oustinov, Z. Y. Zhao, S. Hameau, S. Barbieri, P. Filloux, X. Marcadet, C. Sirtori, and J. Tignon, "Spectral gain narrowing in THz Quantum Cascade Lasers above laser threshold using THz-time domain spectroscopy", Technical Digest, *CLEO/QELS 2008, Conf. on Lasers and Electro-Optics (2008).*

International Conferences

[Oral] N. Jukam, S. Dhillon, D. Oustinov, Z. Y. Zhao, S. Hameau, S. Barbieri, P. Filloux, X. Marcadet, C. Sirtori, J. Tignon, « Spectral gain narrowing in THz Quantum Cascade Lasers above laser threshold using THz-time domain spectroscopy », **CLEO/QELS' 08, Conf. on Lasers and Electro-Optics**, San Jose, 04/05-09/05 2008.

[poster] Z.Y. Zhao, S. Hameau, J. Tignon, «THz generation by optical rectification and competition with other nonlinear processes», **ICPS 2006, 28th International Conference on the Physics of Semiconductors**, Vienna, 24/07-28/07 2006.

[poster] Z.Y. Zhao, S. Hameau, M. Voos, J.Tignon, « THz generation by optical rectification and competition with other nonlinear processes », **ISSTT 2006, International Symposium on Space-Terahertz Technology**, Paris, 10/05-12/05 2006.

[Oral] S. Dhillon, N. Jukam, D. Oustinov, Z. Y. Zhao, S. Hameau, S. Barbieri, P. Filloux, X. Marcadet, C. Sirtori, J. Tignon, "Spectral gain Narrowing in THz quantum cascade lasers", **33rd International Conference on Infrared, Millimeter, and Terahertz Waves, Pasadena**, 15/09-19/09 2008.

National Conferences

[Oral] N. Jukam, S. Dhillon, Z.Y. Zhao, J. Armijo, G. Duerr, M. Voos, S. Hameau, J. Tignon, «THz generation using interdigitated emitters. Application to the study of QCLs », **4ème Journées THz**, Bombannes, 29/05 - 31/05 2007, exposé invité (J. Tignon).

[Oral] N. Jukam, S. Dhillon, Z.Y. Zhao, J. Armijo, G. Duerr, M. Voos, S. Hameau, J. Tignon, « Spectroscopie téra-Hertz ultra-rapide », **Première Rencontre Nationale des Jeunes Chercheurs ANR**, Orléans, 11/04 - 12/04 2007.

[poster] Z.Y. Zhao, S. Hameau, J.Tignon, « Génération d'impulsions THz par rectification optique et compétition avec d'autres mécanismes non-linéaires», **JMC10, Journées de la Matière Condensée**, Toulouse, 28/8 - 1/9 2006.

[poster] D. Oustinov, N. Jukam, S. Dhillon, Z-.Y. Zhao, S. Hameau, S. Barbieri, P. Filloux, C. Sirtori, X. Marcadet, J. Tignon « Etude du gain dans les lasers à cascade quantique THz par spectroscopie THz dans le domaine temporel », **JMC11, Journées de la Matière Condensée**, Strasbourg, 25/08 – 29/08 2008.

[oral] N. Jukam, S. Dhillon, D. Oustinov, J . Madéo, S. Hameau, S. Barbieri, P. Filloux, X. Marcadet, C. Sirtori, and J. Tignon « Application de la Spectroscopie THz dans le Domaine Temporel aux Lasers à Cascade Quantique THz », **JMC11, Journées de la Matière Condensée**, Strasbourg, 25/08 – 29/08 2008.

[poster] D. Oustinov, N. Jukam, Z-.Y. Zhao, S. Hameau, S. Dhillon, W. Maineult, P. Gellie, S. Barbieri, C. Sirtori and J. Tignon « Lasers à cascade quantique THz : hautes performances et dynamique inter-soubande », **Rencontre DGA Recherche et Innovation Scientifique**, Paris, 20/03 2008.

[oral] Z. Y. Zhao, T.Q. Jia, J. Lin, Z.-R. Sun, and Z.G.Wang « Femtosecond non-resonant optical nonlinearity of silver chloride nanocrystals doped niobic tellurite glass», **Annals of Shanghai Physics Society**, Shanghai 06/12 2007

[oral] Z. Y. Zhao, T.Q. Jia, J. Lin, Z.-R. Sun, and Z.G.Wang « Optical limiting induced by trapped state exciton of silver chloride nanocrystals doped niobic tellurite glass », **Annals of Shanghai Optics Society**, Shanghai 15/11 2007